Universität Greifswald

Institut für Geographie und Geologie

Late Quaternary paleoenvironmental records from a glacially and permafrost affected island in the Canadian Arctic

(Herschel Island, Yukon Coastal Plain)

Diplomarbeit

zur Erlangung des akademischen Grades

Diplom-Geograph

vorgelegt von

Michael Fritz

Greifswald, 29. Februar 2008

„Es ist nichts, was den geschulten Verstand
mehr kultiviert und bildet, als Geographie."

– Immanuel Kant –

TABLE OF CONTENTS

LIST OF FIGURES

LIST OF TABLES

ABSTRACT

Herschel Island − about 70 km east of the Yukon-Alaska border − occurs as the only major elevation on the Yukon Coastal Plain facing the Southern Beaufort Sea and represents the likely westernmost edge of Wisconsin Glaciation in northwestern Canada. Being accumulated as a terminal moraine during the Early to Middle Wisconsin the island has been intensively affected by periglacial processes for a period of time that probably dates back to 50 ka BP but is still of great uncertainty.

Multi-proxy analyses on sediments and stable isotope determinations (δD, $\delta^{18}O$) on ground ice samples have been performed to reconstruct the island's paleoenvironmental evolution and paleoclimatic variations through time. Distinct stages in landscape succession are addressed with regard to permafrost/ground ice aggradation and its degradation through time as well as to link these processes to distinct periods of climate change.

Sediments generally consist of clayey diamicton and silty loams with a quite uniform origin as near-shore marine beds that have been glacially redeposited and set as a terminal moraine that makes up the body of the modern island. Stratigraphic appraisals are difficult due to the deformed nature of Herschel Island sediments by glacial ice thrust. However, even these deformations give evidence that deeper strata remained unaffected by post-glacial thaw and reworking, thus representing original Pleistocene deposits. Climate amelioration during the early Holocene Thermal Maximum (HTM) between 11 and 8 ka BP led to increased thermokarst processes and an enhanced accumulation of peat. Extensive active layer thickening is recorded by a widespread thaw unconformity along the Yukon coast at depths between 1.5 to 2.5 m below surface. Increased bioproductivity, Holocene cryoturbation and recent mass wasting have produced an upper diamicton with deviant cryostructures and significantly more organics than below the discontinuity.

Different types of ground ice have been recovered that range widely regarding their isotopic composition, thus reflecting different types of water and strongly variable climatic conditions during their genesis. Holocene ice wedges vary in $\delta^{18}O$ between −24 and −20 ‰ (VSMOW). A fossil wedge truncated at 1.5 m below surface, revealed low $\delta^{18}O$ values between −30 and −27 ‰ and is therefore supposed to have formed during an ice-free period of more severe climatic conditions prior to HTM. Texture ice within sediment sequences might be an applicable tool for paleoclimate reconstructions as isotope values show clear dependency with depth and enable the recognition of afore-identified boundaries in paleoenvironmental development like the prominent thaw unconformity. Buried glacier ice and ice of unknown origin with low isotope values (< −30 ‰) seem to contribute to ground ice spectrum on Herschel Island, too.

Up to the present day, the study area is affected by extensive coastal erosion and ongoing melt of ground ice, that both leads to a strong geomorphological alteration of the landscape.

KURZFASSUNG

Herschel Island − etwa 70 km östlich der Grenze zwischen Alaska und Kanada − tritt als einzige wesentliche Erhebung auf der Yukon Coastal Plain an der südlichen Beaufortsee in Erscheinung und befindet sich am westlichen Rand der maximalen Wisconsin-Vereisung im Nordwesten Kanadas. Die Insel wurde während des Früh- bis Mittel-Wisconsin als Endmoräne geschüttet und über einen langen Zeitraum von periglazialen Prozessen stark beeinflusst, der möglicherweise bis 50 ka BP zurückreicht aber noch immer mit großer Unsicherheit behaftet ist.

Multidisziplinäre Analysen an Sedimenten und die Bestimmung stabiler Isotope (δD, δ^{18}O) am Grundeis wurden vor dem Hintergrund durchgeführt, die Paläoumweltentwick-lung der Insel und Paläoklima-Variationen entlang der Yukon Coastal Plain über die Zeit zu rekonstruieren. Unterschiedliche Stadien der Landschaftsentwicklung werden mit Blick auf Bildungs- und Degradationsprozesse von Permafrost und Grundeis untersucht und wie diese Prozesse mit bestimmten Klimaveränderungen in Verbindung stehen.

Die untersuchten Sedimente bestehen im allgemeinen aus tonigen Diamikten und siltigen Lehmen mit relativ einheitlichem Ursprung als küstennahe Flachmeerablagerungen, die glazial umgelagert wurden und als Stauchendmoräne den Korpus der Insel bilden. Aufgrund der deformierten Struktur vorliegender Sedimente infolge des Eisschubs ist eine stratigraphische Einordnung schwierig. Jedoch zeugen eben diese Deformationen davon, dass tiefere Schichten von postglazialen Tau- und Umlagerungsprozessen unbeeinflusst blieben und somit die ursprünglichen pleistozänen Ablagerungen repräsentieren. Die Klimaerwärmung während des (früh)holozänen Klimaoptimums zwischen 11 und 8 ka BP führte zu verstärkten Thermokarstprozessen und einer gesteigerten Torfakkumulation.

Eine flächendeckende Mächtigkeitszunahme der Auftauzone bis auf 1,5-2,5 m unter Flur ist durch eine weitverbreitete Auftaudiskordanz entlang der Yukon Coastal Plain doku-mentiert. Erhöhte Bioproduktivität, holozäne sowie rezente Kryoturbationsprozesse und Massenverlagerungen haben eine oberen Diamikt geschaffen, der sich durch signifikant höhere Organikgehalte und verschiedenartige Kryostrukturen auszeichnet als sie unterhalb der Diskordanz auftreten.

Verschiedene Typen Grundeis wurden vorgefunden, die in ihrer isotopischen Zusammensetzung stark variieren und somit unterschiedliche Wassertypen und stark schwankende Klimabedingungen während der Eisgenese widerspiegeln. Holozäne Eiskeile schwanken im δ^{18}O-Wert zwischen −20 und −24 ‰ (VSMOW). Ein fossiler Eiskeil, der bei 1,5 m unter Flur gekappt wurde, weist δ^{18}O-Werte von −30 bis −27 ‰ auf und scheint daher während einer eisfreien Periode strengerer Klimabedingungen vor dem holozänen Klimaoptimum gebildet worden zu sein. Das Textureis in Sedimentsequenzen stellt möglicherweise ein geeignetes Instrument in der Paläoklimarekonstruktion dar. Denn zum einen zeigen die Isotopenwerte eine klaren Zusammenhang mit der Tiefe an und zum anderen lassen sich die zuvor identifizierten Grenzen in der Paläoumweltentwicklung, wie

jene markante Auftau-diskordanz, nachvollziehen. Begrabenes Gletschereis und Grundeis unbekannter Herkunft mit niedrigen Isotopenwerten (< −30 ‰) scheinen ebenfalls zum Grundeisspektrum von Herschel Island beizutragen, was noch bis vor wenigen Jahren als umstritten galt.

Bis in die Gegenwart hinein wurde das Untersuchungsgebiet durch umfassende Küsten-erosionsprozesse und anhaltendes Schmelzen von Grundeis beeinflusst. Beide Prozesse haben zu starken geomorphologischen Veränderungen der Landschaft geführt.

1 INTRODUCTION

1.1 Scientific rationale

The high latitudes of the northern hemisphere are highly vulnerable to climatic change (ACIA, 2004) with a modern warming trend that is projected to exceed the global mean warming by roughly a factor of two (IPCC, 2007). Widespread increases in thaw depth along arctic coasts are projected to be associated with an extensive release in terrigenous carbon as additional greenhouse gas (OECHEL et al., 1993) and enhanced coastal erosion rates − a risk for industry, community planners and aboriginal peoples (RACHOLD et al., 2004; LANTUIT, 2005).

As there have been significant climatic and hence environmental changes in the Late Quaternary, this study focuses on terrestrial archives in permafrost sequences that provide worthwhile information for reconstructing paleoenvironmental conditions and variations (e.g. MACKAY, 1974; BURN et al., 1986; VAIKMAE, 1989; VASIL'CHUK & VASIL'CHUK, 1997; MEYER et al., 2002a,b; SCHIRRMEISTER et al., 2003) deduced from presently observable processes and thus hopefully enable to predict future developments.

Herschel Island on the Yukon Coastal Plain in the western Canadian Arctic possesses an archive to study strong environmental gradients as it was glaciated during pre-late Wisconsin times but apparently remained ice-free during the Last Glacial Maximum (LGM) although in direct vicinity to the Laurentide Ice Sheet (LIS) to the east. Therefore, the study area lies immediately on the interface of the formerly glaciated area to the east and the easternmost margin of the unglaciated land mass Beringia to the west. Beringia extended continuously between the Taymyr Peninsula in the Russian East to the Mackenzie River in the Northwest Territories of Canada in consequence of a globally lowered sea level by about 120 m (PELTIER, 2002). Despite its apparently outstanding position for the understanding of the regional landscape development, the island's Quaternary history is largely unknown and relies on a master thesis published by Bouchard in 1974 and a report treating the Yukon Coastal Plain that dates back to 1982 (Rampton, 1982) and that is largely inspired by reports written in former years.

Additionally, further knowledge about the island's environmental history is of special public interest since Herschel Island Territorial Park, together with two other National

Parks on the Yukon mainland is designated to become Canada's next UNESCO World Heritage Site.

Since about fifteen years the Alfred-Wegener-Institute for Polar and Marine Research (Research Unit Potsdam) applies multi-proxy approaches comprising various disciplines (e.g. sedimentology, geomorphology, geocryology, hydrochemistry, isotope geochemistry, paleoecology) in order to get an encompassing view about the framework of processes in paleoenvironmental as well as in paleo-landscape development. Following an adapted approach, this thesis grew on the basis of a joint Canadian-German field campaign on Herschel Island and the mainland of the Yukon Coastal Plain in July 2006 bringing together the expertise of German and Canadian scientists to solve existing scientific issues in this remote region.

1.2 Aims & objectives

In the context of the afore-mentioned research activities, this present work shall generally contribute to a better understanding of the formation of the island and the landscape-shaping processes in both, the glacial and periglacial scope of environmental history. Therefore, detailed paleoclimatic and paleoenvironmental information within an age-controlled context are needed to reconstruct Herschel Island landscape succession since deglaciation.

A joint approach using sedimentary and stable isotope records will provide insights into postglacial permafrost history. Permafrost sequences taken from coastal outcrops consist of both, sediments and ground ice that will be employed as source material for a multi-disciplinary scientific approach comprising sedimentological, cryostratigraphic, geochronological and biogeochemical analyses as well as stable isotope determination with the following objectives:

- to describe permafrost inventory and the sedimentary as well as cryostratigraphic conditions

- to identify facies changes within permafrost deposits and to refine the stratigraphic position and order of Herschel Island sediment beds;

- to precise the age of deposition and the processes responsible for the formation of Herschel Island

- to assert the genetic processes associated with massive ground ice on Herschel Island;

- to distinguish different periods of ground ice formation;

- to track different stages in landscape development since deglaciation;

- to compare paleoenvironmental proxy data from both sides of the Late Pleistocene glacial margin in order to distinguish and evaluate periglacial and thus landscape-shaping processes of both realms.

The plethora of analyses and the difficulty to produce comparability and summarising classification of highly diverse strata on Herschel Island and beyond the glacial limit are not least responsible for the extent of this thesis.

2 STUDY AREA

2.1 Geographical setting & geological situation

Physiography

Herschel Island, also known as *Qikiqtaruk* − an Inuvialuit idiom for "it is island" −, is located in the northern part of the Yukon Territory, Canada. The island is situated approximately 70 km to the east of the Yukon-Alaska border, about 200 km west of Inuvik as the closest bigger settlement and lies 3 km off the Yukon continental coast in the southern Beaufort Sea at 69°36'N and 139°04'W (Fig. 2.1). It covers an area of about 108 km² with a maximum spatial extent of 8 by 15 km and has an apex elevation of 185 m above sea level (LANTUIT, 2005).
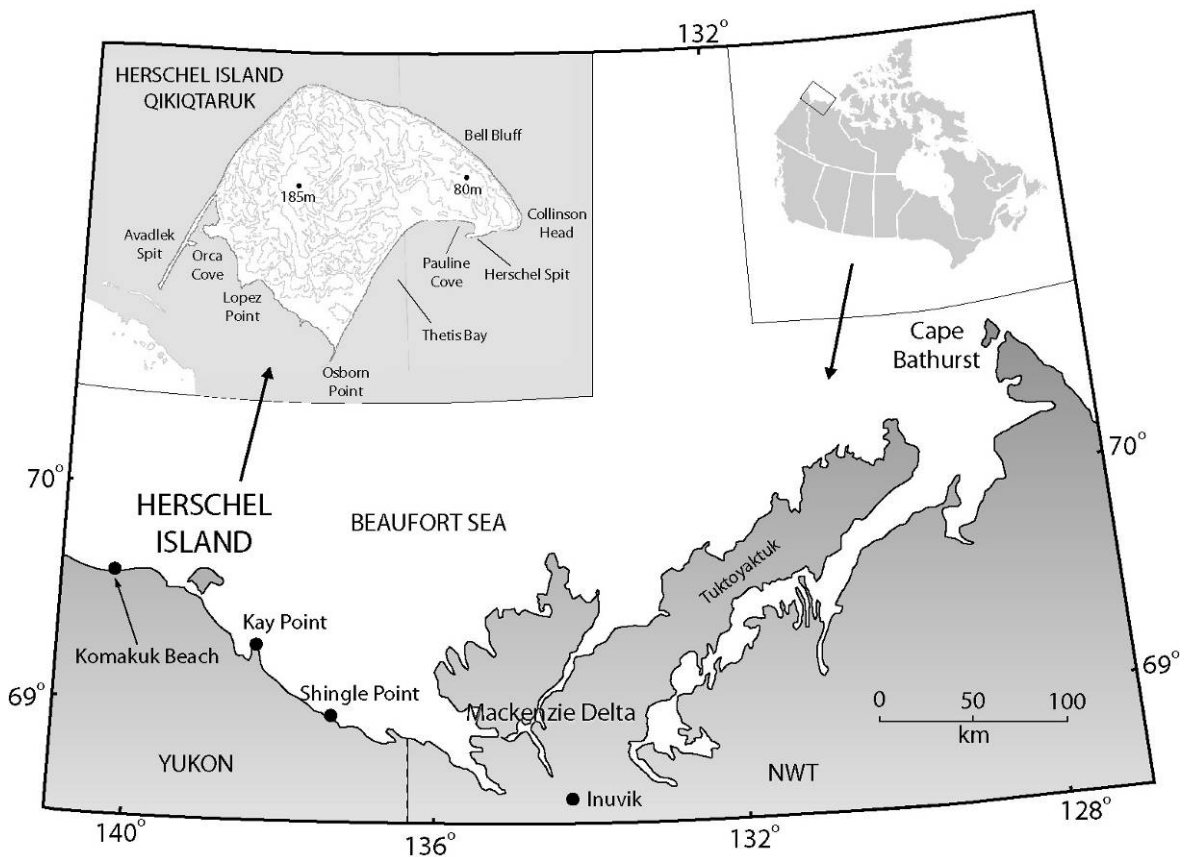
Fig. 2.1: Map of the study area showing the regional topography as well as the sample areas Komakuk Beach and Herschel Island (after LANTUIT, 2005).

Herschel Island is part of the Yukon Coastal Plain physiographic region (RAMPTON, 1982) − a landward extension of the Beaufort Sea Shelf − that is structurally due to a gently sloping late to middle Tertiary erosional surface (pediment), covered with Pleistocene and

Holocene unconsolidated deposits (RAMPTON, 1982). The plain extents about 200 km from southeast to northwest beyond the Yukon-Alaska border where it gives way to the Alaska North Slope. The plain is bounded to the east by the Mackenzie Delta. The Richardson Mountains, the Barn and British Mountains (including the Buckland Hills), as foothills of the Alaskan Brooks Range, act as a mountainous fringe to the west and south of the plain. About 10 to 30 km in width on the mainland, the plain rises in altitude slightly from west to east (BOUCHARD, 1974). Offshore, it spreads as the continental shelf where it slopes gently to the north until the shelf abruptly steepens into the Mackenzie Trough at about 80 m water depth (HILL et al., 1991). The shelf is relatively narrow, ranging from 40 km wide in the western area to over 150 km wide at the Mackenzie Delta (COUTURE, 2006, unpublished).

The topography of Herschel Island is generally divided into two major parts. The north and north-eastern area is characterised by the higher elevations and steeper relief features (DE KROM, 1990), whereas the southern and south-western part exhibit lower elevations and a slightly more gently-sloping terrain. The areas of higher relief show a hummocky to rolling morphology marked by a series of morainic ridges alternating with parallel, asymmetrical narrow valleys. Deep gullies dissect the ridges forming steep valleys with depths up to 45 m (DE KROM, 1990), which form a roughly radial drainage pattern from the highest central part of the island towards the coast.

The north to north-eastern coastline is dominated by steep cliffs/bluffs up to an elevation of 50 m fronted by very narrow to non-existent beaches (LANTUIT, 2005). Where the coast is directly exposed to the Beaufort Sea, wave action and ice scour lead to intense coastal retreat since undercutting of cliffs causes large block failures of frozen sediments. The coastal morphology along the lower side of the island is more complex comprising coastal bluffs of comparable lower elevation, spits, gravel and sand beaches as well as alluvial fans. Large aggrading spits on the mainland-facing side of the island (Avadlek Spit, Herschel Spit, Osborn Point) as well as beaches along the southwest side consist of gravel, coarse sand and locally contain boulders (BOUCHARD, 1974; DE KROM, 1990). Coastal slopes are subject to intense thermokarst activity including numerous large retrogressive thaw slumps and active layer detachments slides (LANTUIT, 2005). Active and relic stabilised retrogressive thaw slumps may extend up to 500 m inland and reach a lateral extent of 1 km. On the south-east side, the shoreline is mantled by a thick accumulation of

supersaturated clay, clayey silt and organic matter, which represent residues of thermokarst activity and mass wasting. The island's interior is subjected to other forms of permafrost processes and therefore landscape-shaping processes, including permafrost heave and subsidence, melt out of ice wedges, formation of thermokarst lakes and polygon formation.

Mackenzie Delta

The estuarine Mackenzie Delta, extending north-south for approximately 210 km and about 65 km in width, is of postglacial age. The Late Pleistocene (Wisconsin) Laurentide Ice Sheet covered the Mackenzie region and changed the landscape dramatically with the consequence of forcing the river to its present-day course. Since deglaciation, the Mackenzie River delivers the sediments for progradation of the delta into the southern Beaufort Sea, while it drains approximately 1.8 million km² including large parts of the Canadian Shield and the Western Cordillera (HILL et al., 1991). With an estimated annual solid discharge of 1.25×10^8 tonnes a^{-1} (LEWIS, 1988), the Mackenzie River is clearly the major sediment source, contributing to 95 % of the total sediment supplied to the shelf (HILL et al., 1991). The average thickness of Holocene accumulation is approximately 80 m.

Thick accumulations of 20-30 m fine-grained to very fine-grained sediments are present in the Mackenzie Trough, directly seaward of the delta, to water depths of 100 m. East of Mackenzie Trough, the thickness of Holocene mud is generally less than 20 m and decreases eastward (HILL et al., 1991). As the thickness of Holocene deposits decreases to the east, the grain size does as well.

On the seaward part of the Yukon Coastal Plain, sediments are not primarily deposited by deltaic outpour of the Mackenzie Delta system although this drainage system is still the major contributor for sediment supply on the plain. Here, secondary deposition takes place when material proximate to the delta is resuspended during strong wave and wind action (see Fig. 2.2). Resuspended material is then transported by longshore currents and wind-driven currents to distal areas throughout the shelf.
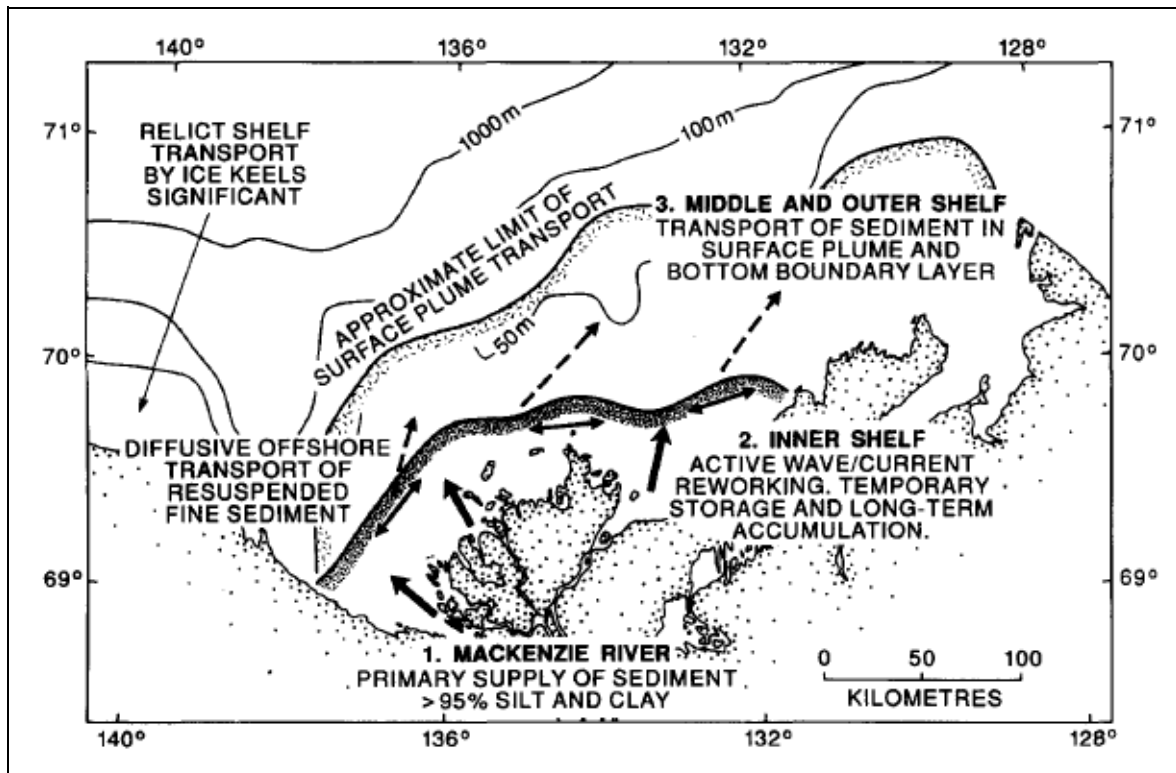
Fig. 2.2: Sediment transport on the Canadian Beaufort Shelf originating from the Mackenzie River. Note that the study area lies westward beyond the limit of surface plume transport (HILL et al. 1991; p. 839).

Yukon Coastal Plain

The whole Yukon Coastal Plain as well as its submarine extension on the upper shelf is underlain by the bedrock surface of a Tertiary pediment that slopes gently from the southern mountains towards the coast and beyond. A thick cover of pre-Quaternary and Quaternary deposits, ranging from a few metres close to the mountain fringe to more than 60 m on the shelf and the coastal strip, including Herschel Island (RAMPTON, 1982).

According to Rampton (1982), the Yukon Coastal Plain can be divided into two major parts: (1) The coastal fringe, directly adjoining the Beaufort Sea, has no significant slope as a whole but is of undulating morphology on specific sites where glacial ice-thrust features are supposed. (2) In southern direction, a gently coastward sloping area fringes the mountains to the south and belongs to the upper part of the Tertiary erosional surface extending northward into the Beaufort Sea.

In general, sediments reworked by periglacial processes cover the entire plain and often hold an organic cover of variable thickness (MACKAY, 1959; BOUCHARD, 1974).

West of Firth River (i.e. to the west of Herschel Island), the area is almost flat consisting of fluvial deltas and alluvial fans since several creeks and streams (e.g. Firth River, Malcolm River, Fish Creek), incising the British Mountains, flow downslope into the Beaufort Sea.

The geological map of Herschel Island and Demarcation Point (GEOLOGICAL SURVEY OF CANADA, 1981) shows that fluvial deposits as silt, sand and gravel form deltas and alluvial fans, which are neighboured by marine and estuarine silt and sand where fluvial forms are missing.

Between Firth River and Shingle Point, close to westernmost Mackenzie Delta extensions, a rolling to hummocky terrain with numerous ponds and lakes covers the plain. Absolute elevations rarely exceed 60 m and a local relief of at most 30 m is present (RAMPTON, 1982) with exception of Herschel Island (max. 185 m) and a coast-parallel ridge connecting Kay Point and King Point (max. 80 m). Mackay (1959) first suggested an ice-thrusted origin due to the observation of strongly tilted, folded and contorted sediments between Herschel Island and King Point.

During the Pleistocene, glaciers advanced at least twice towards the coastal plain (MACKAY, 1972a; DUK-RODKIN et al., 2004), while only the oldest advance is supposed to have extended in the study area and little west of Herschel Island bordering the southern Firth River erosional channel.
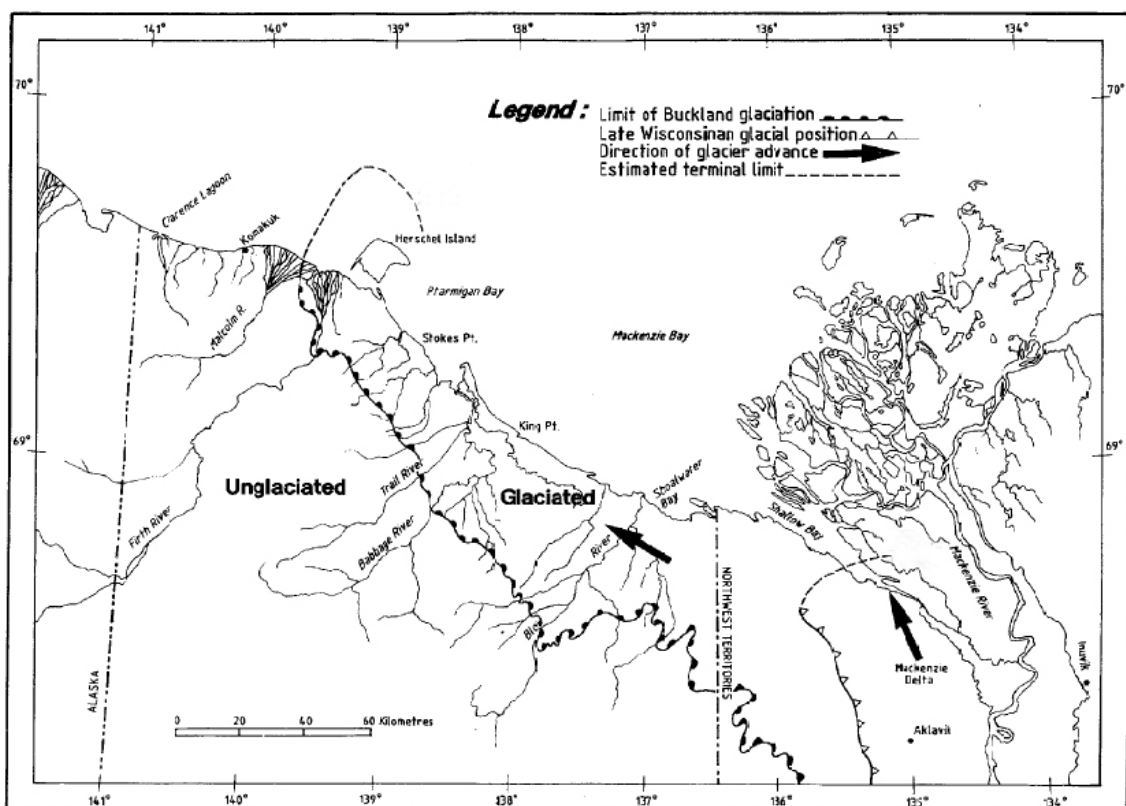
Fig. 2.3: Glacial limits along the Yukon Coast. Buckland Glaciation was most extensive but is still unclear in age. Late Wisconsin glacial position was within the Mackenzie Delta region (SMITH et al., 1989 p. 6; adapted from Rampton, 1982 and Dyke & Prest, 1987).

Thus, the study site at Komakuk Beach presumably lies well beyond the Wisconsin glacial limit (Fig. 2.3). Age determinations for the responsible ice advance vary significantly although many scientists agree with Rampton (1982), dating the glaciation well beyond the Last Glacial Maximum (LGM: ~ 24 ka BP) towards being of Early to Middle Wisconsin (POLLARD & DALLIMORE, 1988; POLLARD, 1990, WOLFE et al., 2001) or pre-Late Wisconsin age (HARRY et al., 1988; KOKELJ et al., 2002, DUK-RODKIN et al., 2004). However, Moorman et al. (1996) dated CO_2 directly from massive ice recovered from Herschel Island, with a maximum age of about 17.5 ka BP. Based on the fact that massive ice must have formed after deglaciation they suggest a more extensive Late Wisconsin glaciation than previously assumed. This leads to great uncertainties regarding the geological point of time and the time period of the maximum glacial extent in the study area, respectively (Fig. 2.4).
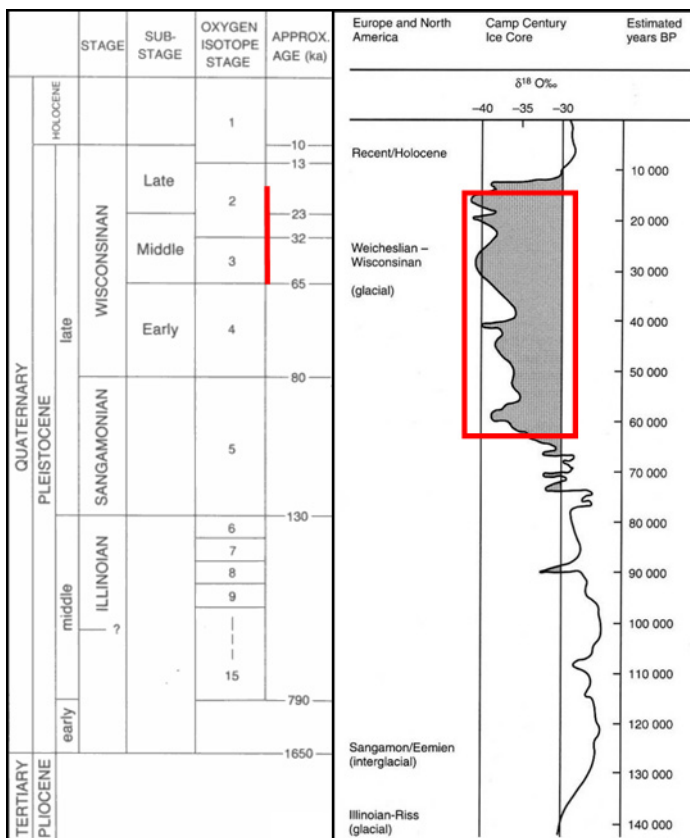
Fig. 2.4: The chronology of the Quaternary showing the alternation between glacial and interglacial times with regard to oxygen isotope stages (left hand side; after FULTON, 1989). More detailed isotopic resolution for the last glacial-interglacial period is shown on the right hand side from Camp Century oxygen isotopic data (Greenland, 77°10'N, 61°08'W) (after FRENCH, 1996). Red line and rectangle indicate the period of Buckland Glaciation, according to Rampton (1982), with high uncertainty.

Herschel Island

Herschel Island was shaped by glacial activity during the Late Pleistocene by the north-westward movement of a lobe of the Laurentide Ice Sheet (Fig. 2.5). Rampton (1982) postulated that the glacier advance took place during an early stage of the Wisconsin

glacial period, termed Buckland Glaciation, although there exists no universally accepted age for this glacial advance, ranging widely from about 65 ka BP until 17.5 ka BP (see Fig. 2.4).
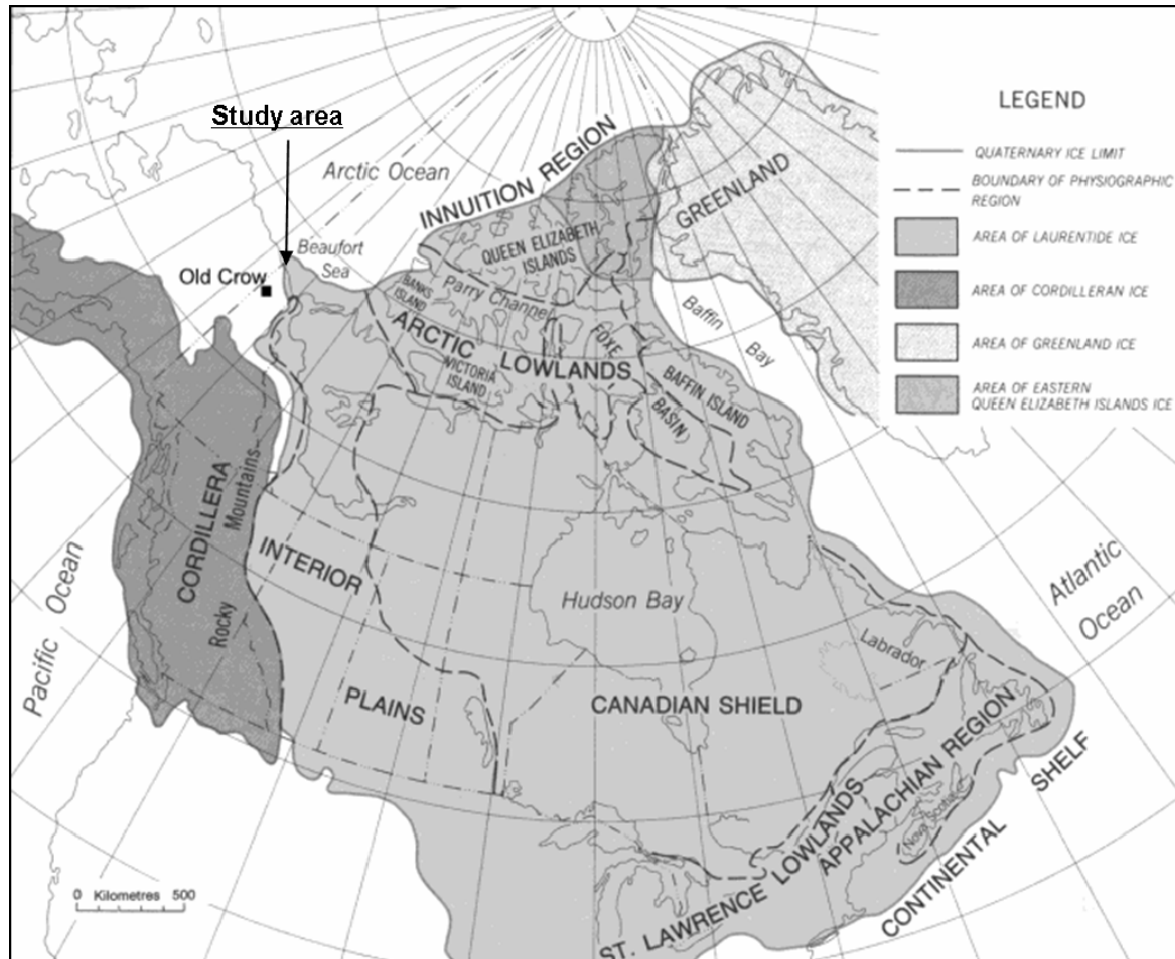
Fig. 2.5: Limits of ice cover in North America during the Quaternary (after FULTON, 1989).

As Mackay (1959) suggested, the island was formed by glacial plough and push up of frozen sediments to form an ice-thrusted terminal moraine, representing the present-day main body of the island. This theory is supported by the existence of the Herschel Basin within the sea floor (Ptarmigan Bay) southeast of Herschel Island, having approximately the same volume as the island (BOUCHARD, 1974; SMITH et al., 1989).

Intense stratigraphic and morphological investigations have been performed by Mackay (1959) and Bouchard (1974), being compiled by Rampton (1982) to distinguish strata with different genetic origin and different age. Drilling accompanied by seismic studies suggest that bedrock is absent from the island until at least 35 m below surface (b.s.). Drilled and exposed sediments throughout the island are classified as pre-glacial, glacial and

postglacial deposits (BOUCHARD, 1974).

(1) Relatively young postglacial deposits are usually related to the accumulation of organic matter, littoral and alluvial processes as well as mass movement.

(2) Glacial deposits include erratic boulders and pebbles scattered throughout the surface up to the highest points of the island with a lithology that was identified originating from a distant source region, namely deriving from the Mackenzie Mountains south of the Mackenzie Delta (BOUCHARD, 1974).

(3) According to Bouchard (1974), preglacial deposits include all other sediment types associated with or without ice-thrust features, which are the most common and most complicated stratigraphic units forming the island. Although, sediments affected by glacial ice-thrust, represent glacial deposits in their sense of genesis, they are attributed as preglacial in order to their primary deposition predating glaciation. They are categorised in terms of the environment they formed in as marine, non-marine and mixed sediments (BOUCHARD, 1974).

2.2 Climate & vegetation

Climate

The Yukon Coastal Plain owns a polar tundra climate with an average temperature of the warmest month above 0°C but below 10°C. The study area is characterised by a harsh, cold, arctic climate dominated by continental arctic air in winter and maritime arctic air in summer (RAMPTON, 1982). The temperature distribution is more continental in nature than maritime as a result of ice cover most of the year in the Southern Beaufort region (SMITH et al., 1989).

Temperature and precipitation surveys were carried out by the *Meteorological Service of Canada* for the reference period 1971-2000 at Komakuk Beach, an immediate study site 50 km west of Herschel Island, at Shingle Point at the south-eastern edge of the Yukon Coastal Plain and at Inuvik (North West Territories) being located slightly more inland. Mean annual temperatures range from −11°C at Komakuk Beach (Fig. 2.6) to −9.9°C at Shingle Point and −8.8°C in Inuvik pointing to a south-easterly trending temperature gradient. July mean daily temperatures vary from 7.8°C at Komakuk Beach to 11.2°C at Shingle Point and 14.2°C at Inuvik. January mean temperatures range from −24°C at

Komakuk to −23.7°C at Shingle Point and −27.6°C at Inuvik.

Komakuk Beach (7.3 m)

69°34.8' N   -11°C
140°10.8' W   161.3 mm
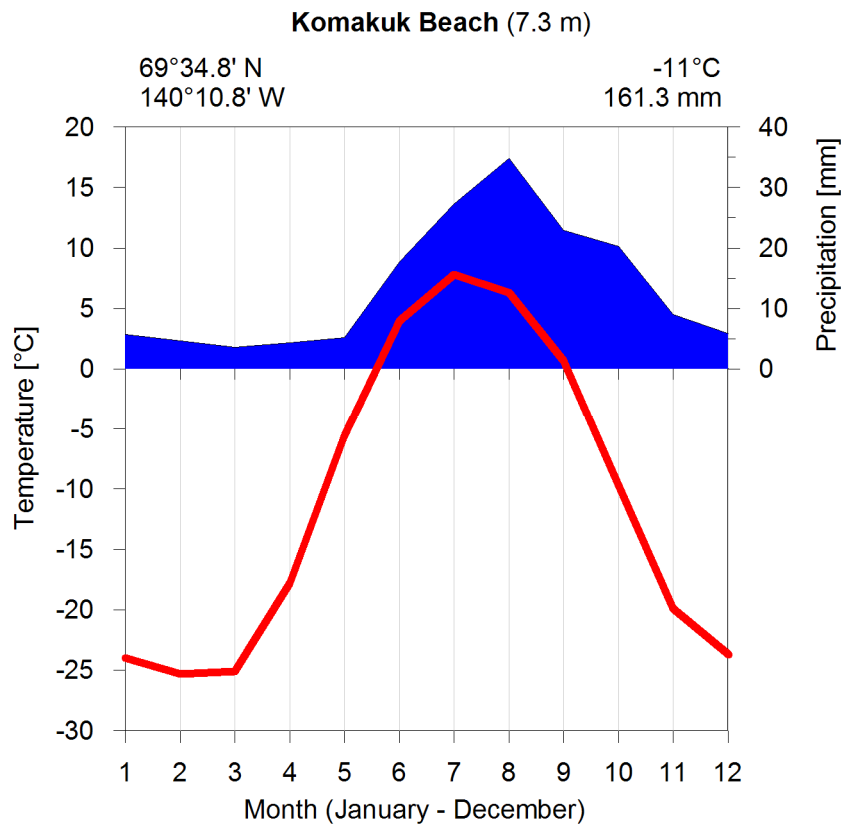
Fig. 2.6: Climate chart of Komakuk Beach. Temperature distribution shows a continental low-arctic climate with low precipitation values. (data source: METEOROLOGICAL SERVICE OF CANADA, 2006).

Precipitation averages around 154 mm at Komakuk Beach, rising to 253 mm at Shingle Point and almost 250 mm at Inuvik, which falls mainly in form of rain or drizzle during the short summer when the Beaufort Sea is free of ice. Maximum snow cover averages 50 cm on the plain although depths are variable due to drifting (RAMPTON, 1982). Snow melts during late May to early June, whereas meltwater is retained until river breakup in early June releasing most of the annual water supply in a short burst (REIMNITZ & WOLF, 1998). Floods at breakup are the major annual sedimentation events so that most of the annual suspended sediment load is delivered to the sea during a 2-week period after ice breakup (REIMNITZ & WOLF, 1998).

Wind – a major climate element in coastal areas regarding sediment transport and coastal erosion – blows from to main directions:

(1) North-westerly winds are prevailing for most of the year causing a net easterly drift of surface water over almost the entire shelf (HILL, 1990).

(2) However, from May to August winds prevail from eastern directions (BOUCHARD, 1974) leading to reverse current and thus sedimentation directions (HILL et al.,

1991).

Sea ice is present for most of the year with exception of 3-4 months each summer, thus limiting open-water conditions and most notably limiting the fetch. During the period of open water, fog and cloud cover are maximum.

Vegetation

The study area lies more than 100 km to the north of the modern tree line. Its vegetation is a direct result of the harsh climate, the proximity to the Arctic Ocean, landscape evolution and the occurrence of permafrost near surface. Smith et al. (1989) summarised the soil and vegetation properties of Herschel Island within the scope of a survey performed by the Land Resource Research Centre, Canada. As a result, 194 plant species in 28 families were catalogued, grouped into 11 vegetation types and 8 ecological map units, respectively.

Herschel Island and Komakuk Beach are mainly covered by arctic and alpine tundra species that differ in composition and coverage due to hydrological conditions, soil properties, morphological features and their state of succession.

Arctic willow, dryas and vetch (*Salix arctica, Dryas integrifolia, Astragalus umbellatus / alpinus*) are the dominating species on extensive, smooth uplands with gentle slopes, where fine-textured and moderately well- to imperfectly-drained soils, namely Orthic Turbic Cryosols (AGRICULTURE CANADA EXPERT COMMITTEE ON SOIL SURVEY, 1987), predominate. The upland plateau on the central portion of the island is covered by cotton grass / tussock tundra (*Eriophorum vaginatum & Bryophytes*). This kind of vegetation cover represents the typical vegetation type for the whole region on level to gently-sloping terrain with depressional polygonal ground, standing water and small thermokarst ponds.

2.3 The periglacial environment

The term "periglacial" was first introduced by Lozinski (1909) describing climatic and geomorphologic conditions of areas peripheral to ice sheets. More recently, the term refers to a broad range of processes in cold, non-glaciated regions regardless of their proximity to glaciers, either in time or space (WASHBURN, 1979; FRENCH, 1996). For the purpose of this thesis, two diagnostic criteria are worthwhile to describe periglacial environments. (1) The presence of perennially frozen ground and (2) processes that are related to frost-action in association with water, especially the occurrence of freeze-thaw cycles leading to

mechanical weathering, frost heave and subsidence, frost cracking and ice wedge-growth as well as material sorting.

Approximately 25 % of the earth's land surface (about 50 % of Canada and 80 % of Alaska) are currently underlain by perennially frozen ground, also known as permafrost (Fig. 2.7) (FRENCH, 1996). This term describes ground, regardless whether it consist of rock, unconsolidated deposits or organics, that remains at or below 0°C for at least two consecutive years (VAN EVERDINGEN, 1998).
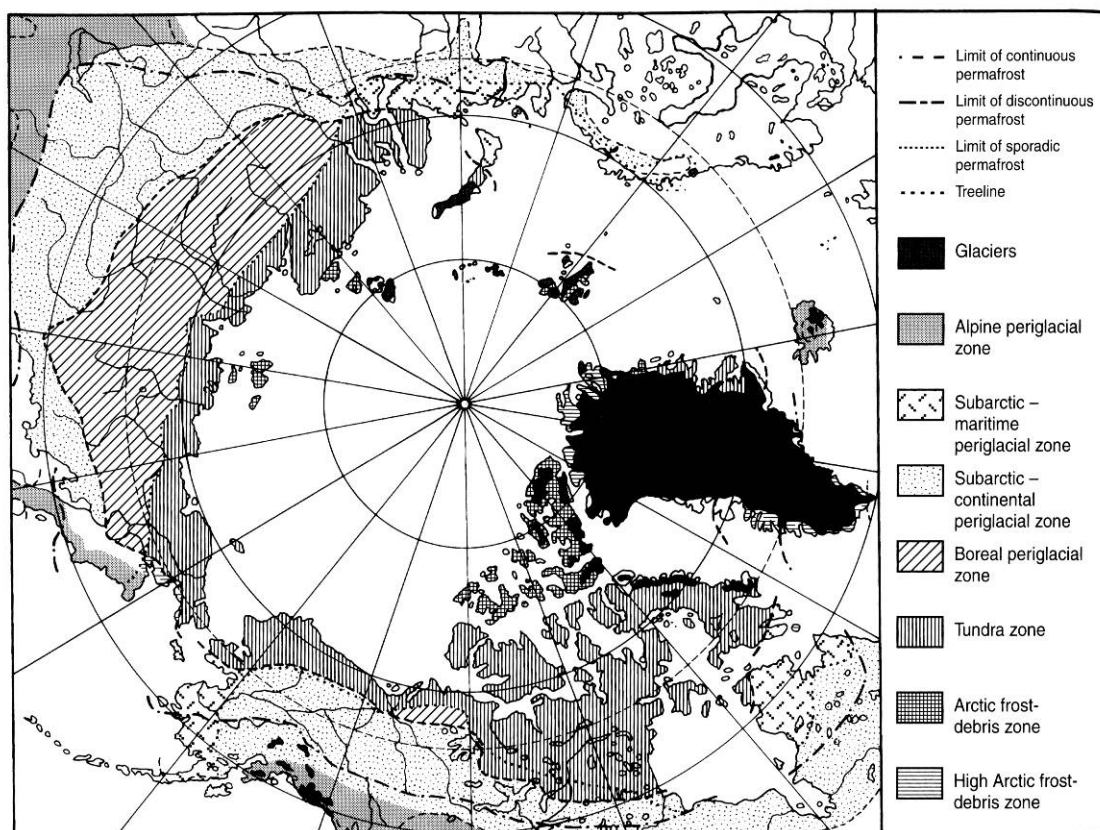
Fig. 2.7: Extent of periglacial zones and permafrost distribution in the northern hemisphere (FRENCH, 1996 p. 4; according to KARTE, 1979).

The most important environmental factors controlling permafrost conditions are indeed the prevailing regional climate, topographic features and the subsurface material as well as its moisture content (WASHBURN, 1979). The growth of permafrost reflects a negative thermodynamic balance between ground and surface temperature, which is controlled by air temperature and the geothermal gradient (POLLARD, 1998). Regarding this precondition, three major zones of permafrost distribution can be differentiated:

(1) *Continuous* permafrost occurs within a zone of very low mean annual temperatures (≤−8°C) and thin snow cover, which inhibits isolation effects, so that permafrost

can actively aggrade or is in freeze-thaw equilibrium;

(2) *Discontinuous* permafrost towards lower latitudes, separated by areas of unfrozen ground, is often relic and/or subject to degradation;

(3) S*poradic* and *isolated* frozen ground is predominantly surrounded by unfrozen ground and represents an advanced stage in degradation (WEISE, 1983).

Permafrost experiences cycles of freeze and thaw associated with periodic (decadal, seasonal or daily) climate and weather cycles. It is overlain by a surficial ground layer, termed "active layer", which lies above the permafrost table and is subjected to those cycles. Active layer depths vary significantly, also from year to year, depending on interactions of factors such as air temperature, radiation, vegetation, snow cover, soil/rock type, drainage, slope orientation and water content (FRENCH, 1996).

The study area lies within the zone of continuous permafrost ashore and a narrow fringe of sub-sea permafrost underlying the shallow offshore part of Yukon Coastal Plain. Permafrost thickness reaches more than 600 m along the Arctic Coastal Plain near Barrow (Alaska) and decreases southward (BROWN, 1970). Previously unglaciated periglacial terrain with little annual snow cover owns greatest permafrost depths since it has not been subject to insulation phenomena or glacial pressure melt since Wisconsin times.

Herschel Island as well as Komakuk Beach exhibit excellent examples of periglacial features although both areas contain a permafrost setup of different temporal maturity since Komakuk has supposedly never been glaciated at least during Wisconsin Glaciation in contrast to Herschel Island. The most abundant surficial characteristics are polygonal nets, earth hummocks, non-sorted patterned ground and thermokarst lakes or depressions on level to gently sloping terrain, whereas gelifluction lobes, thermoerosional valleys and retrogressive thaw slumps are typical periglacial features for areas with higher relief energy.

Ground ice

All of these landscape shaping elements (see above) have their origin in the aggradation or degradation of ground ice, which is a major component of permafrost and is supposed to make up to 50 % of the volume of near-surface permafrost on Herschel Island (MACKAY, 1971). Ground ice, in general, refers to all types of ice formed in freezing and frozen ground, respectively (HARRIS et al. 1988). Mackay (1972b) established a classification

based upon the origin of water prior to freezing and the principle process of water movement towards the freezing plane yielding ten types of ground ice (Fig. 2.8), however, this classification excludes all ice types of buried origin (i.e. glacier ice, snow bank ice, sea ice, river and lake ice) that likely contribute to the ground ice inventory on Herschel Island (FRENCH & HARRY, 1990). Consequently, in 1989, Mackay added a classification of massive ground ice (Fig. 2.9), which is defined as a large mass of ground ice with a gravimetric water content exceeding 250 % (HARRIS et al., 1988), including the former mentioned ice types due to their significance in North American permafrost sequences.
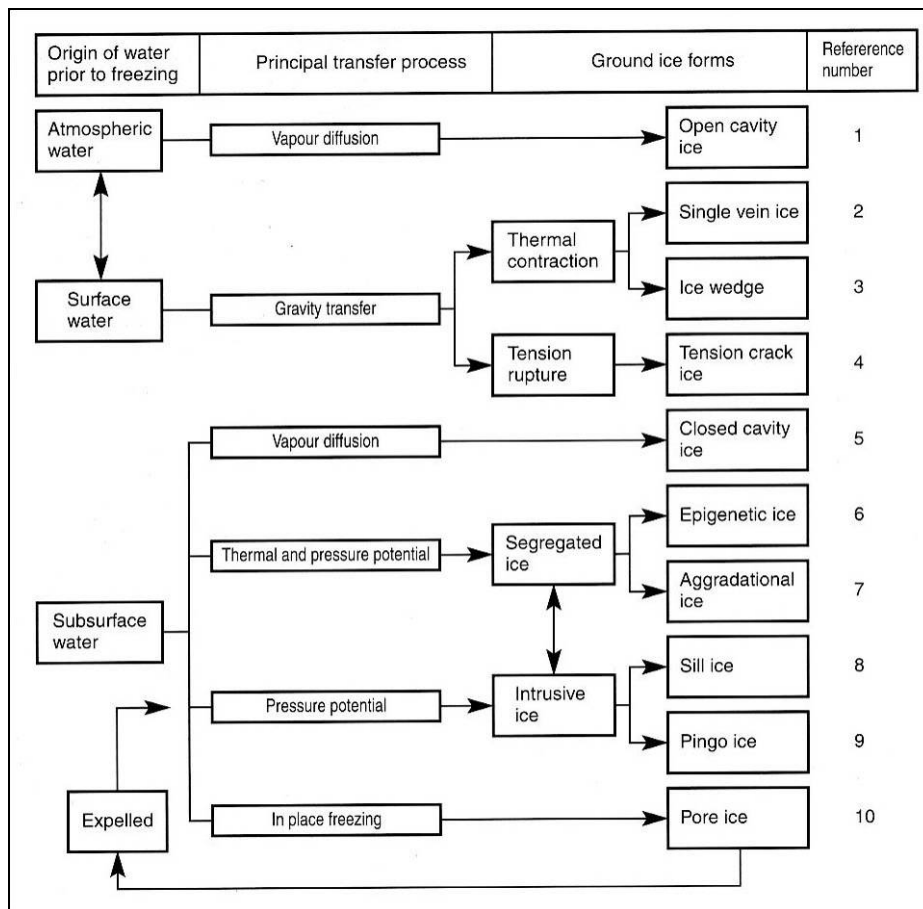
Fig. 2.8: A genetic classification of ground ice (according to MACKAY, 1972a in: FRENCH, 1996 p. 88).
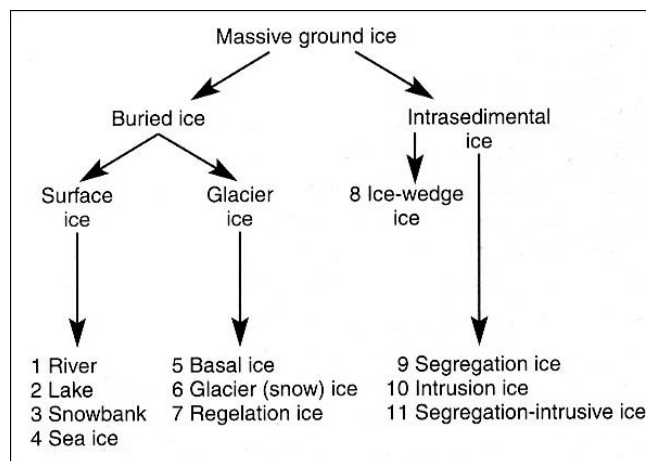
Fig. 2.9: A classification of massive ground ice proposed by Mackay at a GSC workshop in 1989 (FRENCH, 1996 p. 100).

In arctic dry winters, rapid cooling of frozen soil leads to the initiation of vertical fractures (thermal contraction cracks). This process only takes place where the snow cover is usually thin, so that the surface is directly exposed to very low temperatures and not insulated by a thick snow cover (MACKAY, 1979). In the following spring, the frost fissure is filled with melt water, which immediately refreezes due to negative temperatures in the permafrost-affected ground. This leads to the formation of a single ice vein, which prevents the closure of the frost crack. During following winters, the ice-filled crack reopens due to anew thermal contraction as the initial ice vein is assumed to be a zone of weakness (LACHENBRUCH, 1962). Spring meltwater then adds another ice vein. Over several hundreds or thousands of years, repeated cracking and infill with meltwater leads to the formation of a vertically foliated ice wedge (Fig. 2.10 C, D). Depending on whether there occurs accumulation of material or the surface remains stable, ice wedges tend to grow syngenetically or epigenetically. Epigenetic ice wedges grow in already existing permafrost deposits with negligible accumulation or erosion, are usually younger than the host material (MACKAY, 1990) and only grow in width (MACKAY, 1974). In contrast, syngenetic ice wedges grow as the permafrost surface rises due to material supply allowing both horizontal as well as vertical growth (MACKAY, 1990) (Fig. 2.11).

Interconnected ice wedges form polygonal nets as superficial expression, which are characteristic for Arctic Tundra regions and thus reflect ground ice conditions. These polygons occur either as low-centred or high-centred polygons depending on local drainage conditions (FRENCH, 1996).
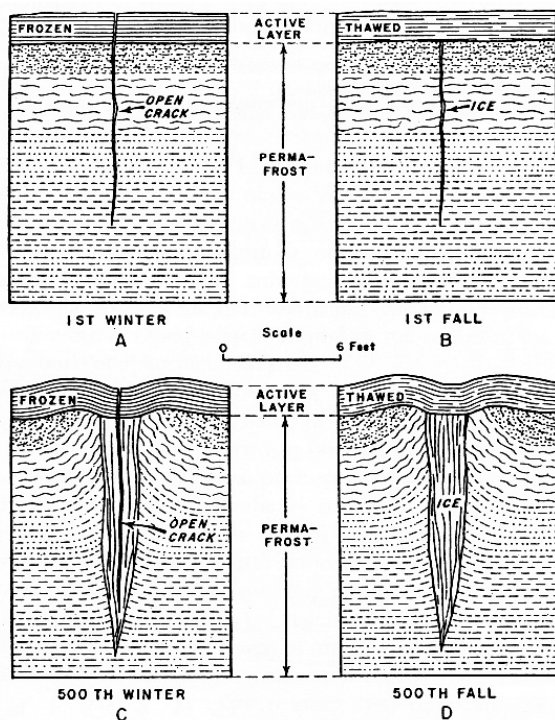
Fig. 2.10: Evolution of an ice wedge according to the contraction-crack theory (LACHENBRUCH, 1962, p. 5).
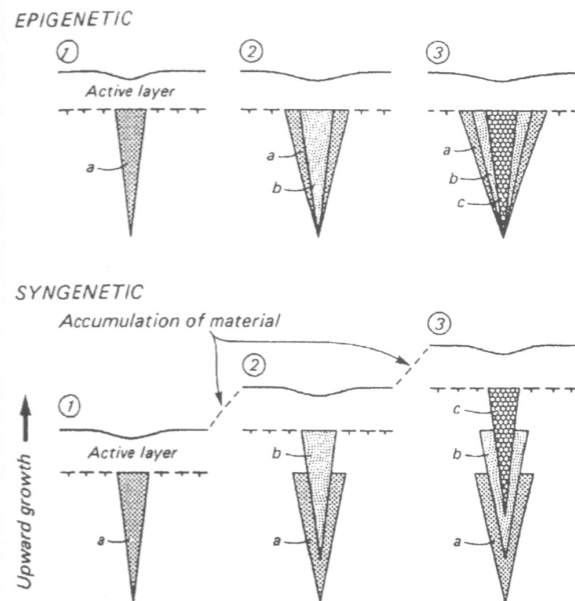
Fig. 2.11: Growth of epigenetic and syngenetic ice wedges (MACKAY, 1990, p. 18).

Thermokarst and thermal erosion

Alteration of the thermal regime in ice-rich permafrost deposits due to climate change, disturbance of vegetation cover, fire or the shift of drainage channels (WASHBURN, 1979) may increase the active layer depth and causes permafrost thaw beyond seasonal freeze-thaw cycles. This in turn leads to several changes in a landscape's inventory being typical for thermokarst and thermo-erosional processes. The extent of morphological change is mainly controlled by the magnitude of the increase in active layer depth and the amount of excess ice in the sediments (FRENCH, 1996). When massive ground ice melts the terrain subsides by the same amount it lost by melt and subsequent drainage. The development of water-filled or dry closed depressions and a hummocky irregular terrain are prominent features for thermokarst subsidence. In some cases thaw lakes (thermokarst lakes) being deep enough that freezing can not proceed through the whole water column, lead to a reinforced thaw process since water has a higher specific heat than ice and dry sediment (WEISE, 1983). In addition, the high specific thermal conductivity of water promotes the development and the extension of an unfrozen body (*talik*) beneath the lake (FRENCH, 1996; HARRIS et al., 1988).

In contrast to thermokarst, which forms solely because of melting of excess ice and drainage of supernatant water, thermal erosion needs an additive transport medium,

although the thaw process remains the essential precondition for permafrost destabilisation. Most prominent thermo-erosional features in the study area are (a) retrogressive thaw slumps, (b) active layer detachment slides and (c) large block failures in combination with thermoerosional niches at coastal bluffs.

(a) Coastal slopes on Herschel Island are subject to intense thermokarst and thermo-erosional activity. When ground ice is present as massive tabular ice bodies, retrogressive thaw slumps develop by backwasting of exposed ice-rich sediments. Such slumps are large bowl-shaped thaw structures (Fig. 2.12) that extend up to 500 m inland and reach a lateral extent of 1 km (LANTUIT, 2005). They generally consist of three major components (DE KROM, 1990; LEWKOWICZ, 1987): (1) A vertical or sub-vertical headwall, (2) a headscarp within the headwall, whose angle varies between 20° to 50° and which retreats by the ablation of ice-rich materials due to sensible heat fluxes and solar radiation (LEWKOWICZ, 1987); and (3) the slump floor, which consists of meltwater, fluid mudflow and plastic flow deposits that expand in a lob-like pattern at the foot of the slump (Fig. 2.12). On Herschel Island, slumps are initiated and maintained by wave erosion at the base of ice-rich coastal cliffs, which uncovers massive ice bodies leading to ice ablation (DE KROM, 1990) and which removes slumped material from the shore to sustain a high relief energy for further slumping.
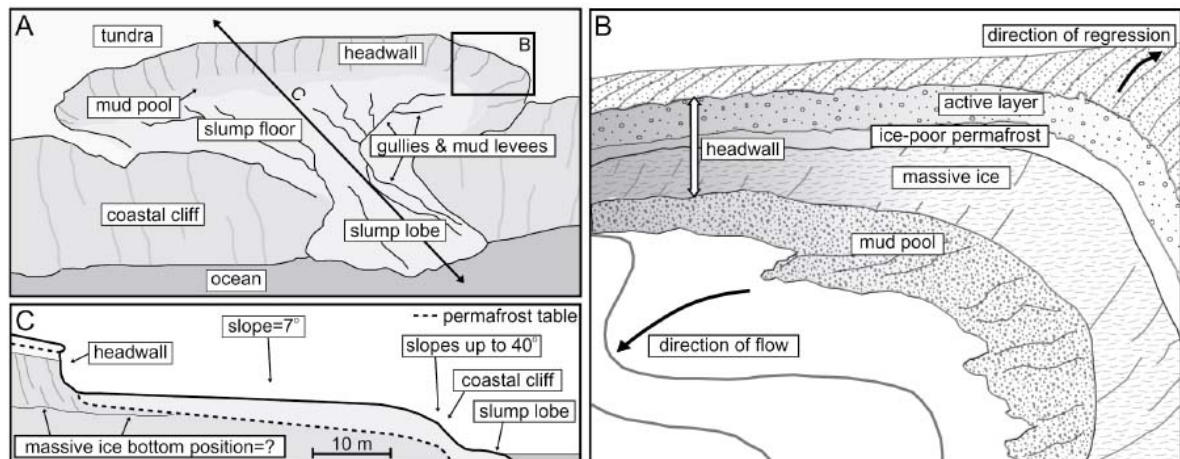
Fig. 2.12: Scheme of a retrogressive thaw slump. Inset B focuses on the slump headwall. Inset C is a cross-section of the slump. (LANTUIT & POLLARD, 2005, p. 415)

(b) Active layer detachments occur on almost planar surfaces right up to steep slopes and are characterised by the downslope movement of seasonally thawed supersaturated material (DE KROM, 1990). When the material's shear strength is exceeded, sliding occurs along an inclined planar surface or along a predetermined failure plane − the permafrost

table. In contrast to gelifluction, where the vegetation cover is not necessarily disrupted (WEISE, 1983), active layer detachments loose their cover due to greater shear stress because of higher sliding velocities. The morphological resultant is a scar of bare soil of varying extent and a downslope lobe containing a mixture of the former active layer components. Formerly divided mineral horizons become strongly scrambled and the organic cover is often thrusted, folded and buried. Active layer detachments on Herschel Island, especially on steep slopes, are often connected with retrogressive thaw slumps as they are supposed to be responsible for the initiation of slumps (besides wave action) and the reactivation of relic retrogressive thaw slumps (LANTUIT, 2005).

c) Coastal bluffs are largely exposed to thermal melting, storm surges and ice scour. While massive ice melts out in response of received radiation subsidence of the remaining material and, thus, destabilisation of the steep bluff occurs. Meanwhile, waves are not only capable of eroding by mechanical means, but also by thermal melting of permafrost (FRENCH, 1996). Hence, thermo-erosional niches undercut still frozen sediments that leads to the collapse of large blocks being washed to the sea.

2.4 Study sites

2.4.1 Herschel Island

Four different study sites on Herschel Island (Fig. 2.13) were treated in order to obtain sediment samples, recent waters and ice samples from different ground ice types. There exist several reasons for choosing outcrops at Collinson Head (COL) and within the retrogressive thaw slump, termed "Thaw Slump D (TSD)". Both sites are characterised by the presence of a relatively high and steep bluff and headwall, respectively. This was important for analyses since long and continuous profiles should be recovered. Moreover, the outcrops obviously promised a great variety of stratigraphic units, ice-thrust features and various ground ice types. And finally, the accessibility of the area in general and of the sites in particular was a reason for the decision.
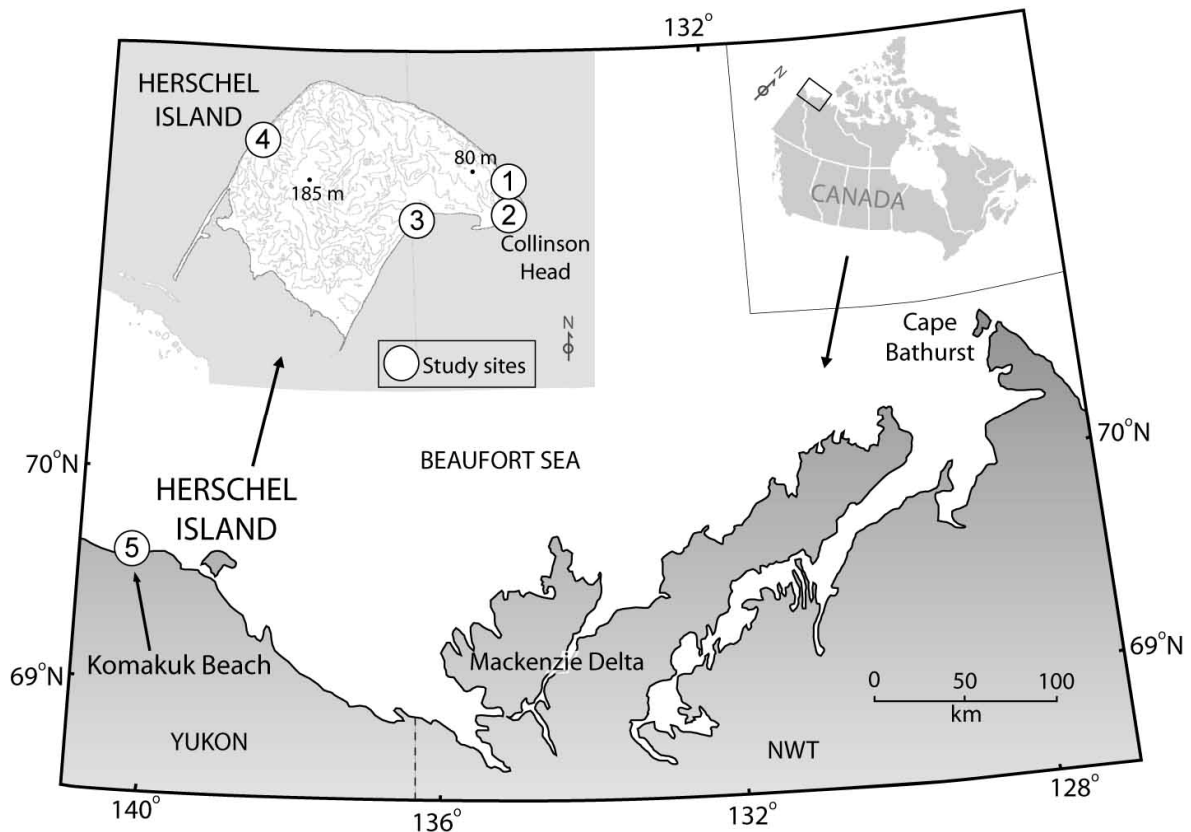
Fig. 2.13: Map of the study area with consideration of the study sites (marked with white circles) on Herschel Island and at Komakuk Beach on the mainland.
Figures 1-5 correspond to the following profiles and study sites as they are termed in the following work: **(1) Collinson Head No.1 − COL 1; (2) Collinson Head No.2 − COL 2; (3) Thaw Slump D − TSD; (4) HI-GI; (5) Komakuk Beach − KOM** (after LANTUIT & POLLARD, 2005, p. 414).

2.4.1.1 Collinson Head

Outcrop No.1 is located at the headwall of a retrogressive thaw slump at the northeastern edge of Herschel Island, named Collinson Head at 69°34'47.6"N, 138°51'49.8"W with an elevation of about 73 m above sea level. The slump is approximately 80 m in width possessing a headwall circa 3 m in height. The surrounding ground surface is gently sloping, non-hummocky and vegetated by tussock tundra. There is no direct visible evidence that the area was previously affected by creep and/or slump activity (Fig. 2.14 A).
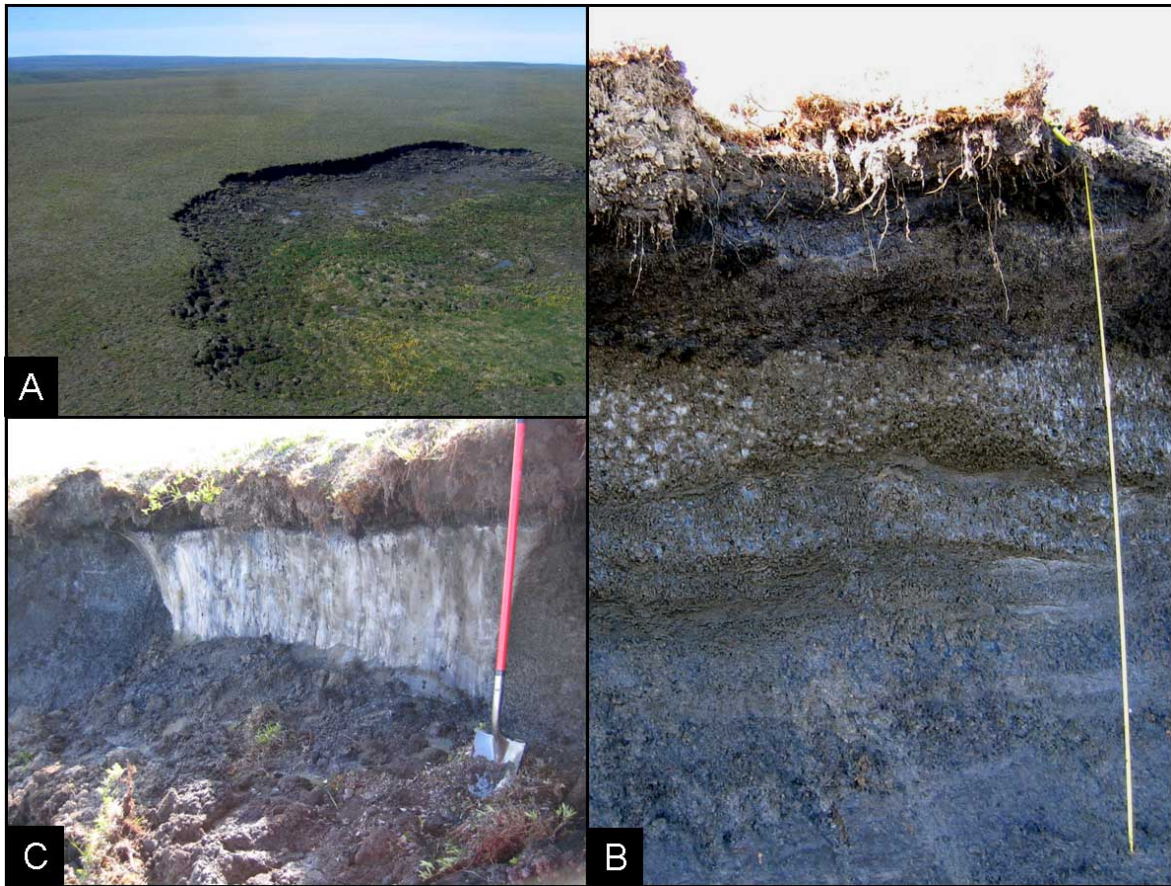
Fig. 2.14: Outcrop No.1 at Collinson Head.
Study site lies within a retrogressive thaw slump at Collinson Head. Picture A shows the slump within a surrounding being unaffected by slump or creep activity. Inset B shows the slump headwall, where the sediment profile was obtained. The sampled ice wedge HI-IW-1 is shown in inset C (Photos: Lantuit, H., Meyer, H., Schirrmeister, L., 2006).

The thaw slump reveals four ice wedges, which cut with the base of the active layer at 20-30 cm below surface. A sediment profile and one adjacent ice wedge (HI-IW-1) were sampled. (Fig. 2.14 B, C).

Outcrop No.2 is located within a second retrogressive thaw slump at Collinson Head. The slump faces the east coast at 69°34'19.4"N, 138°52'19.9"W with an elevation of about 45 m above sea level. The slump is more than 100 m in width, possesses a headwall that is circa 6 m in height and has a direct contact to the shoreline (Fig. 2.15 A). The surrounding ground surface is sloping, non-hummocky and vegetated by tussock tundra. The slump is located just above the coastline and the adjacent terrain was previously affected by creep and/or former cycles of slumping. A continuous sediment profile could not be sampled because of limited accessibility of the headwall. Thus, three partial profiles covering the

whole height of the headwall were sampled with overlapping intervals between them (Fig. 2.15 B, C, D).
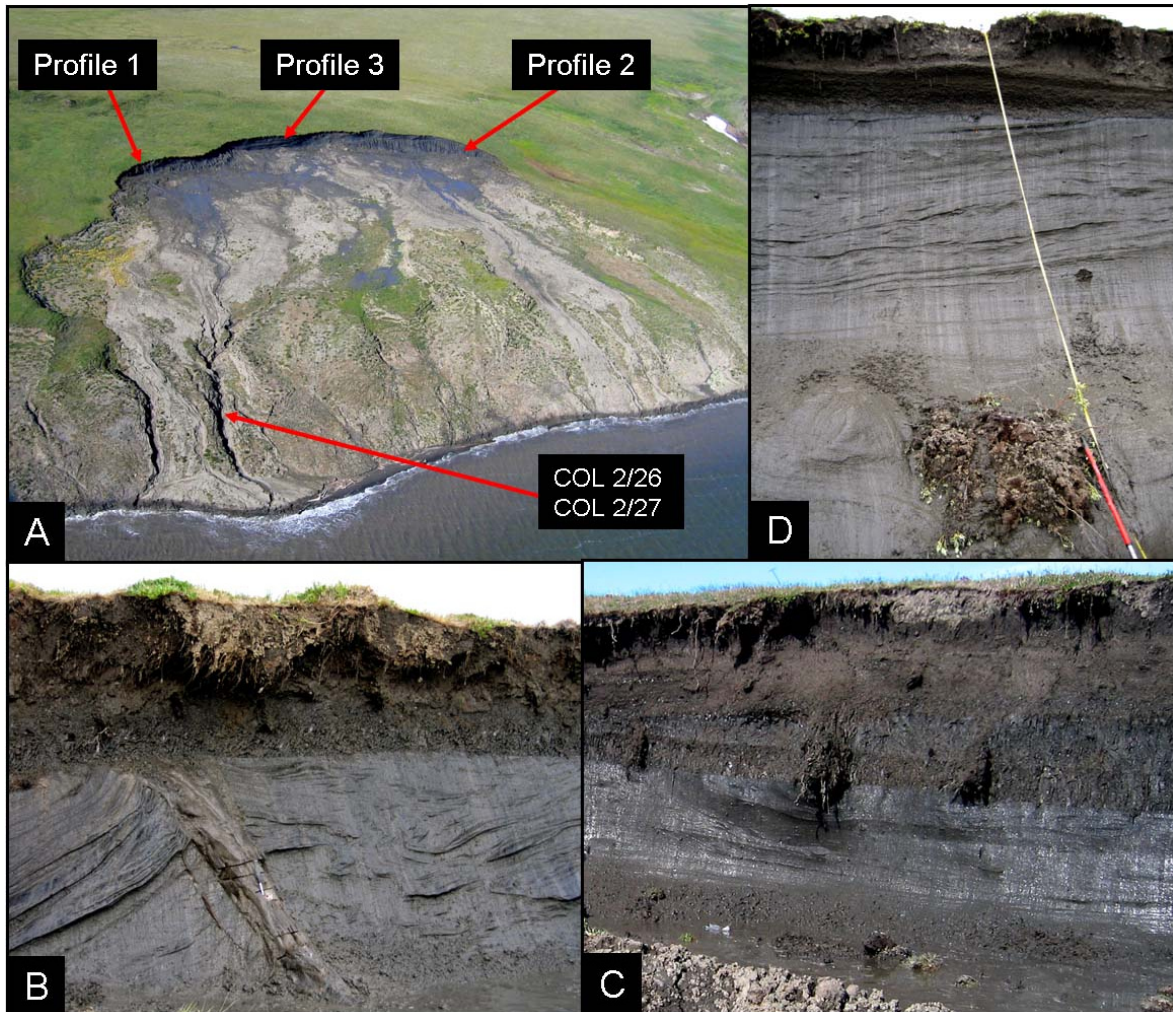
Fig. 2.15: Outcrop No.2 at Collinson Head.
Study site within a retrogressive thaw slump at Collinson Head. Inset A shows the slump within the surrounding that was affected by previous cycles of slump activity. Inset B shows the slump headwall, where the *Profile 1* was obtained as well as the sampled ice wedge HI-IW-2. Further sediment *Profiles 2 & 3* were sampled in the slump headwall shown on picture C & D (Photos: Lantuit, H., Meyer, H., Schirrmeister, L., 2006).

An ice wedge (HI-IW-2) that penetrates the adjacent sediments vertically and a snow patch were sampled in terms of ground ice (Fig. 2.15 B) besides supernatant water received from thawed sediment samples.

2.4.1.2 Thaw Slump D

This large slump is located in the south-eastern coastal zone of the island facing Thetis Bay at 69°35'52.1''N, 139°13'56.8''W with an elevation of 50 m above sea level. The area surrounding the slump is part of the hilly terrain typical for the island and can either feature

hummocky terrain in the higher part of the slump or non-hummocky sloping surfaces previously affected by slump and/or creep activity in the lower part. The slump is more than 400 m in width, owns a vertical headwall that is approximately 10 m in height and has a direct drainage-contact to the shoreline (Fig.2.16).

Fig. 2.16: Retrogressive Thaw Slump D (TSD).
White line frames the recently active slump area. Note that there are several other slumps around TSD within a relic slump affected area (Photo: Lantuit, H., Meyer, H., Schirrmeister, L., 2006).

A great variety of sediment profiles and ground ice features were sampled at different locations within the slump yielding four sediment profiles and adjacent ground ice samples that comprise an injection ice vein, a massive ice body, three ice wedges and two supposedly relic snow patches. Additionally, supernatant water was taken from thawed sediments for stable isotope analyses.

2.4.1.3 Herschel Island−Glacier Ice (HI-GI)

A further outcrop in an erosional valley on the northwest coast of the island (69°38'27.9"N, 139°05'41.0"W) was visited as it revealed a very interesting body of

massive ice of unknown origin. This large ice body is at least 40 m in diameter and about 9 m in height (Fig. 2.17). The top of the outcrop lies approximately 18-20 m above sea level while the ice body is covered by unconsolidated deposits with a thickness between 3 and 6 metres. Since the ice was assumed to be of maybe glacial origin, it was termed HI-GI (Herschel Island-Glacier Ice).

Fig. 2.17: Outcrop *HI-GI* containing a body of massive and almost pure ice (Photo: Lantuit, H., Meyer, H., Schirrmeister, L., 2006).

2.4.2 Komakuk Beach

The sampling location (Fig. 2.18) is situated between two deltas in the supposedly unglaciated western part of the Yukon Coastal Plain. The outcrop lies within a coastal bluff with a height of 7 m above sea level and is fronted by a beach with a width of approximately 10-15 m. The cliff faces the Beaufort Sea to the north at 69°36'12.3''N, 140°30'11.8''W while the hinterland of the coastal zone is characterised by a sub-horizontal well-developed and dry polygonal terrain which is generally vegetated by cottongrass tussock tundra.
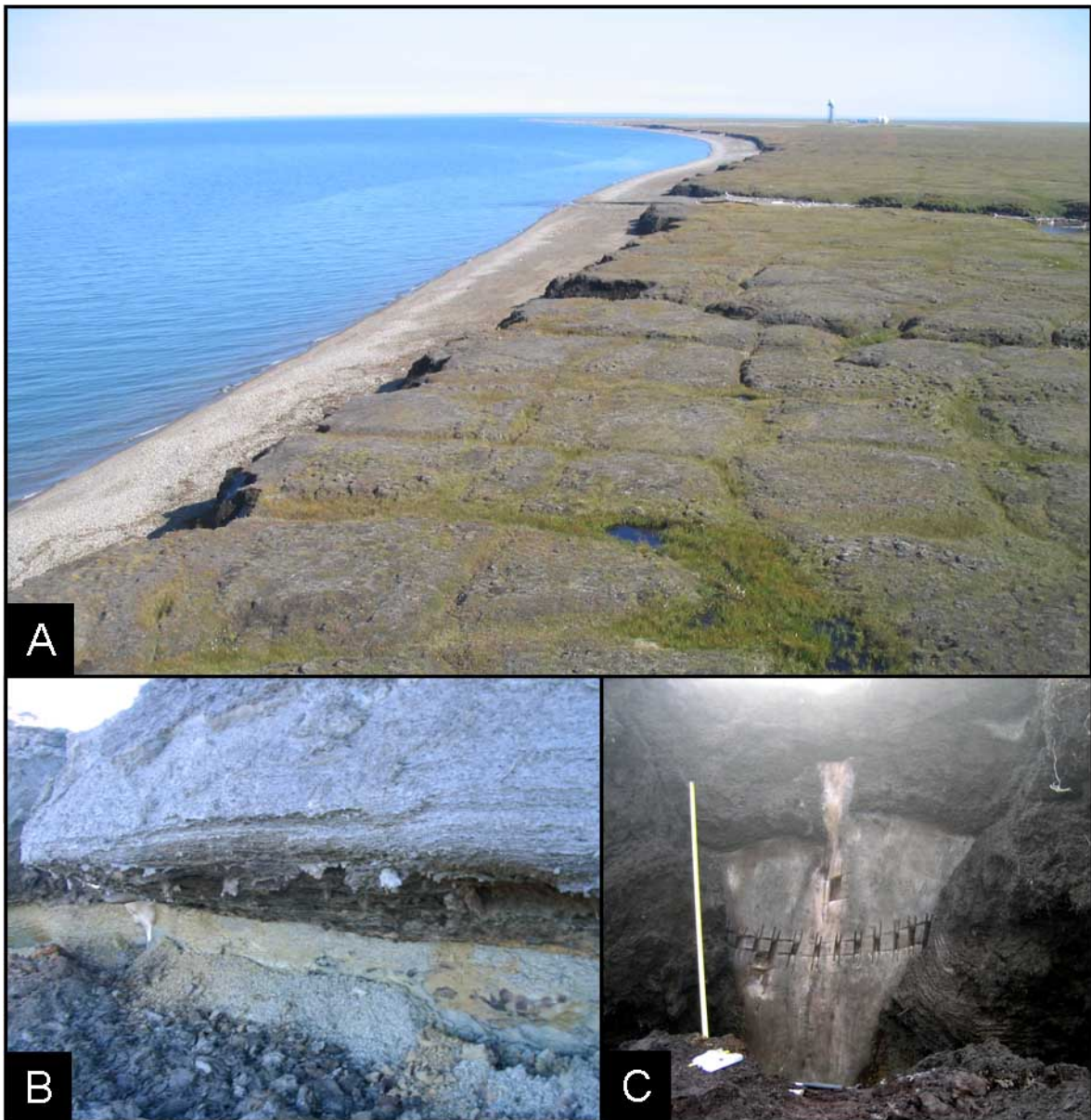
Fig. 2.18: Study site at Komakuk Beach.
Picture A shows the polygonal terrain above the coastal bluff. The general stratigraphy at Komakuk is shown in inset B. Note the yellowish and greenish layers overlain by organic rich and peaty horizons. Picture C shows the sampled ice wedge KOM-IW containing a younger wedge penetrating the older (Photos: Lantuit, H., Meyer, H., Schirrmeister, L., 2006).

3 METHODS

This chapter comprises the different procedures and measurements as well as the technical devices being used for analysing sediments, ground ice, and recent waters during field work and in the laboratory, respectively (Fig. 3.1). Measurements in a temporary field lab on Herschel Island include the determination of absolute and gravimetric ice contents, pH values, and electrical conductivity of supernatant waters of sediment samples as well as of thawed ground ice and recent waters. After return, the sediment samples were analysed for their grain size distribution, magnetic susceptibility, biogeochemical parameters and stable carbon isotope ratios. Recent waters and ground ice samples were measured according to their stable isotopic composition. Furthermore, age determinations in form of radiocarbon dating on organic matter within the obtained sediments were commissioned.
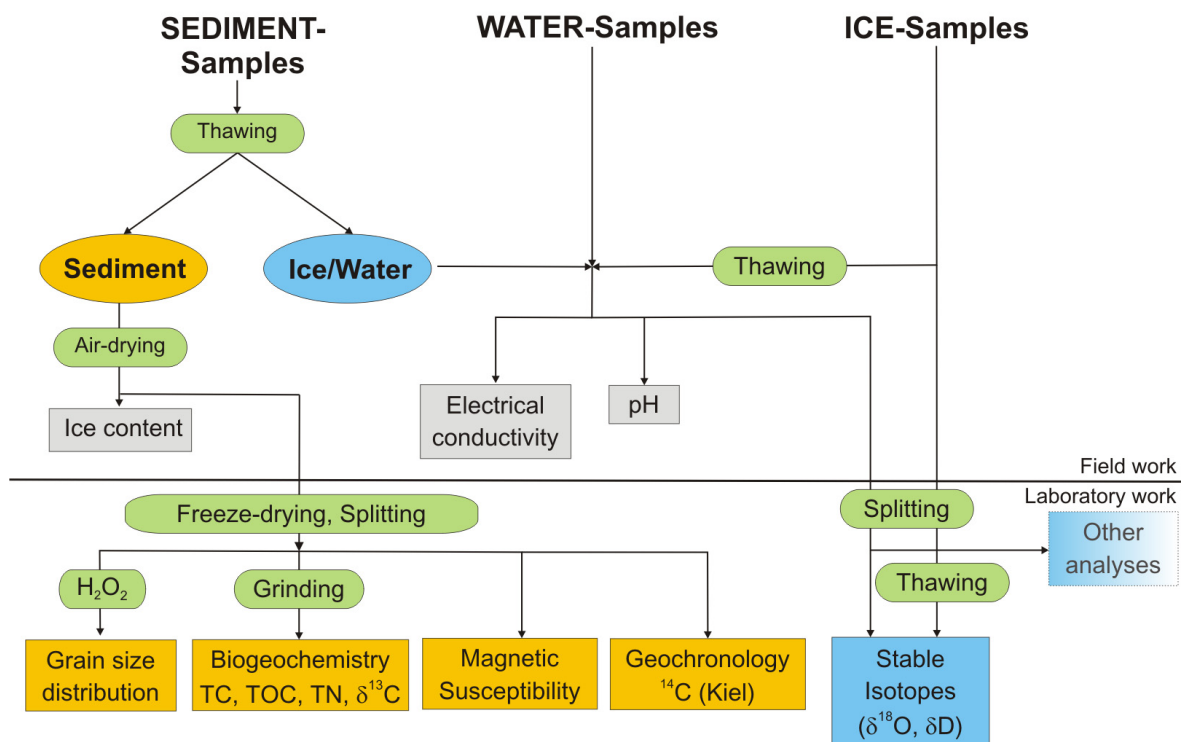
Fig. 3.1: Summarising scheme of methods for preparation and measurements for the majority of samples.

3.1 Field work

Sediments and ground ice samples from permafrost sequences were obtained at comparatively well accessible coastal bluffs and from headwalls of retrogressive thaw slumps. At first the geographical position and altitude of each study site was determined using a hand-held GPS device (Garmin GPS 12 Personal Navigator). Then, the vertical profile height was levelled and the headwall was cleaned from thawed material with a scraper. A detailed description and characterisation of each profile section yielded an overview of sedimentary and cryolithological features and their stratigraphic relationships.

3.1.1 Sediments

Frozen and unfrozen sediment samples were obtained from the different profiles and subprofiles for field description and further analytical lab work. A hammer or a small axe was used to dig out approximately 0.5-1 kg of frozen sediment. After thawing and if supernatant water was received, a water sample was extracted with a plastic syringe and transferred into a separate vial. The electrical conductivity was measured with a conductometer (LF 340-A, WTW). Values of pH were measured subsequently in order to avoid water contamination while using the electrode of the pH meter (PH 340-A, WTW) first, since the electrode contains a KCl buffer solution. For detailed description of measurement procedures see chapter 3.2.2.

Additional material was collected for determining the absolute and gravimetric ice content of permafrost deposits of the several profiles. After thawing and weighing the fresh sample it was dried in a portable oven to measure the dry weight subsequently in order to compute the absolute ice content (a). The difference between these two weights adds up to the gravimetric content (b) of the containing ice or the water, respectively.

> a) Absolute ice content [g] = Fresh sample weight [g] – Dry sample weight [g]
> b) Gravimetric ice content [%] = Absolute ice content [g] × 100 / Fresh sample weight [g]

3.1.2 Ground ice & recent waters

After thawing, a sample of supernatant water was extracted with a plastic syringe for further hydrochemical and stable isotope analyses. The samples were stored in narrow mouth PE-plastic flasks with a volume of 30 ml, which were tightly closed to avoid evaporation. In this context the received waters from sediment samples derive from texture

ice and are treated like this in the following. Sampling of ground ice, regardless of which origin, was mostly combined with sampling of the surrounding sediment and vice versa in order to reveal possible genetic interrelationships.

Different types of ice in form of ground ice (e.g. recent and fossil ice wedges, snow patch ice, massive ice of unknown origin, and segregated ice) were likely encountered and sampled. Therefore, the different types were described carefully in terms of following characteristics:

- altitude
- colour
- cryostructure
- existence of organic matter
- width and height of ice veins and ice wedges

- spatial elongation
- sediment content
- content, orientation, and size of bubbles
- allocation in the surrounding sediments

Depending on ice type and cryostructure, sampling was carried out with the help of ice screws, a small axe or a chain saw. Furthermore, several recent waters (e.g. lake water, rain water, recent snow patches) were collected from different sites throughout the island and at Komakuk Beach for comparing data sets about climate and hydrologic conditions in the past with recent ones.

3.2 Laboratory methods

The following laboratory analyses were all performed at the AWI in Potsdam except the age determination via radiocarbon dating, which was committed to the Leibniz-Laboratory for Radiometric Dating and Stable Isotope Research in Kiel.

This thesis works on overall *75 sediment samples* and ca. *225 ground ice* and *recent water samples*.

3.2.1 Sediments

Before any laboratory measurement, all samples were freeze-dried. Macroscopic organic remains were obtained from selected samples for age determination.

3.2.1.1 Magnetic susceptibility

The mass-specific susceptibility (χ) is defined as the volume susceptibility (κ) divided by the density (ρ), so that $\chi = \kappa/\rho$ with the unit [m^3/kg^{-1}] (BUTLER, 1992). It expresses the ratio of magnetisation in a sample while it is exposed to a magnetic field of known intensity (TAUXE, 1998). Thus, the mass-specific susceptibility of a sediment sample can be assumed as the concentration of magnetisable minerals in an aliquot. The received results give therefore evidence for the content of ferro- and ferrimagnetic minerals, especially magnetite (Fe_3O_4) and pyrrhotite ($Fe_{1-x}S$). Measurements were carried out with a *MS meter Bartington MS2*. For this purpose, the dried but otherwise untreated sample material was filled into a 12.5 ml PVC sample container and weighed afterwards since the sensor is calibrated for a sample mass of 10 g. The value of mass-specific susceptibility is computed as:

χ = mean of measured values [in SI] $\times$ calibration weight [10g] / sample weight [g]

The measured values are not applicable to interpret their absolute values (OPERATION MANUAL BARTINGTON MS2, 1990) but to compare them within a certain profile and to detect invisible boundaries and differences in sedimentary deposits. In addition to other parameters this may yield evidence for the existence of distinctive genetic and chronological strata within a profile.

3.2.1.2 Grain size analysis

The general purpose of grain size studies and the investigation of statistical distributions of grain size fractions in a sediment sample is to reconstruct energetic and environmental conditions during deposition. To comprehend the force of transport energy and the general medium of detrital relocation grain size analyses are useful.

With the help of a laser particle sizer (Coulter LS 200) each sample was analysed in order to get information about its grain size spectrum and to measure quantities of distinct fractions within a sample. Since the analyses have to be carried out on samples free of organic components, they have been treated with a hydrogen peroxide solution (H_2O_2).
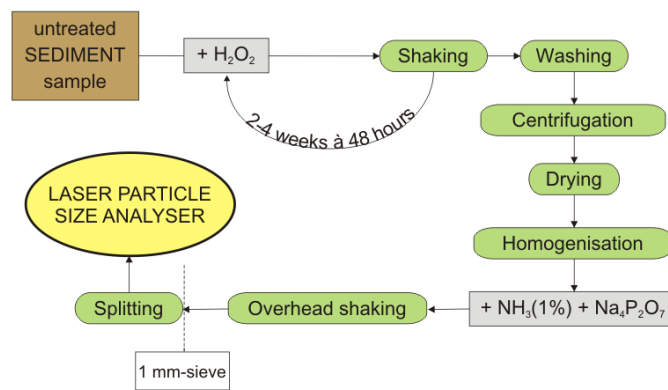
Fig. 3.2: Scheme of sample treatment for the analysis of grain size distribution.

Figure 3.2 shows the sample preparation needed before measuring. Components greater 1 mm were sieved out to avoid damage at the particle analyzer and weighed out to reintegrate them into the grain size spectrum afterwards. Each sample was measured at least two times and the results were averaged, leaving out extremely deviant results. The averaged results were exported to special software tools (e.g. Sedivision® 2.0, Gradistat) to make further statistical appraisals.

The basic principle of laser particle analyses relies on laser diffraction and the conversion of measured diffraction angles and light intensities to a certain grain size. A laser beam with a wavelength of 750 nm, which is focused by a filter and projection lenses on the particle flow (HANDBOOK COULTER LS SERIE TEIL III, 1993) passes the measuring cell at a right angle wherein the sample suspension flows through continuously. Consequently, the laser beam is scattered and diffracted so that a grain size specific pattern develops. A system of Fourier-lenses focuses the diffracted light of different intensities on a detector array consisting of photodiode detectors. In the computer the optical data are converted into digital signals to calculate an integral flux pattern of all particles in a given sample with grain sizes between 0.375 and 2000 μm (HANDBOOK COULTER LS SERIE TEIL III, 1993). Note that granules >1 mm were sieved out manually and reintegrated in grain size statistics.

According to Table 3.1, single grain size fractions can be differentiated to get an overview about the general quantities and distribution of a sample's grain size pattern.

Tab. 3.1: Grain size fractions according to DIN 4022 (from: FÜCHTBAUER, 1988, modified).

phi-grades	9	7	6	4	2	1	-1	-3	-4	-6	-8
µm	< 2.0	< 6.3	< 20	< 63	< 200	< 630	< 2000	< 6300	< 20,000	< 63,000	< 200,000
mm	< 0.002	< 0.0063	< 0.02	< 0.063	< 0.2	< 0.63	< 2.0	< 6.3	< 20	< 63	< 200
		Fine	Middle	Coarse	Fine	Middle	Coarse	Fine	Middle	Coarse	
	Clay	Silt			Sand			Gravel (pebbles, cobbles)			Rocks

3.2.1.3 Biogeochemical Parameters: TC, TOC, TN

Sediments deliver the substratum for living plants and are the most important depositional locations for dead organism remains (DEGENS, 1968). Environmental conditions in a terrestrial or aquatic environment such as temperature regime, precipitation, and sedimentary characteristics (aeration, pH, biological activity) play an important role during formation, decay and accumulation of organic substances. Measuring the contents of total carbon (TC), total organic carbon (TOC) and total nitrogen (TN) give evidence about bioproductivity, decomposition of organic material or their accumulation in the surrounding sediment. Calculations of the C/N ratio and the additional measurement of stable carbon isotope contents (see ch. 3.2.3.2) give information, not only about organic contents or their degree of decay, but also about their biological origin and affiliation.

Principle of measurement

The contents of TOC, TC and TN in the sediment samples were measured quantitatively with a CNS elementar analyzer (Elementar vario EL III). The principle of measurement is based on catalytic tube combustion by means of oxygen supply at high temperatures (HANDBOOK ELEMENTAR VARIO EL III, 2001).

To gain representative analytical results a subsample of about 20 ml by volume was grinded and thereby homogenised with the help of a flint mill (Fritsch) at 3600 RPM. For each sample a weight of 5 mg was encapsulated in tin capsules twice and released to the analyzer via sample disposer.

During combustion in a high oxygen environment, the elements C, H, N and S are oxidised explosively into the gaseous phases CO_2, H_2O, NO_x, SO_2, SO_3 and molecular N_2. Copper

oxide serves as catalyst for the reduction of nitric (NO_x) to N_2, while a lead chromate fill absorbs SO_2 and SO_3. Helium (He) serves as carrier gas for the remaining components CO_2, H_2O and N_2. Specific adsorption columns separate the distinctive components that are subsequently detected by a thermal conductivity detector (HANDBOOK ELEMENTAR VARIO EL III, 2001). Finally, the percentage share of carbon and nitrogen is calculated from its absolute gravimetric content compared to the input sample weight.

Measurements of TOC contents were performed in the same way with different calibration standards and, most notably, samples free of carbonate.

Blanc capsules are analysed to detect background noise while different calibration standards are measured in the supposed range of content for each element to determine the correlation between the measured value and the absolute content since vario EL III is no device for absolute measurements. Measuring control standards after every 20 sample ensures correct analytical values with a device-specific accuracy of ±0.1 %. Although, the content of inorganic carbon ($CaCO_3$) was not determined quantitatively, almost every second sample was tested for its approximate content of carbonate using a field test with HCl (10 %) that provides semi-quantitative results (Tab. 3.2).

Tab. 3.2: Characterisation of carbonate content in fine soil in the field (AD-HOC−AG BODEN, 2004, p.169, altered)

	Carbonate content ($CaCO_3$-equivalent)		CO_2-development and its impact on cohesive sediments
Abbreviation	**Characterisation**	**Mass-%**	
c0	free of carbonate	0	no reaction
c1	very poor carbonate	< 0.5	very weak reaction, not visible, only audible
c2	poor carbonate	0.5 − <2	weak reaction, hardly visible
c3	carbonaceous	2 − <10	not continuous flare-up
c3.2	weakly carbonaceous	2 − <4	weak, not continuous, but visible bubbling
c3.3	medium carbonaceous	4 − <7	clear, not continuous bubbling
c3.4	strongly carbonaceous	7 − <10	strong, not continuous foaming
c4	carbonate-rich	10 − <25	
c5	very carbonate-rich	25 − <50	strong, continuous foaming, no further subdivision possible
c6	extremely carbonate-rich	50 − <75	
c7	pure carbonate	≥75	

3.2.2 Water analytics

This chapter merely deals with the measurements of values of pH and electrical conductivity on sediment solutions and ground ice. Unfortunately, it was not possible to determine the sought values for each sample in the field (see ch. 3.1.1) due to the lack of supernatant water in several samples. However, it seems necessary to obtain the values for a complete sediment profile in order to define distinctive changes and chemical boundaries in the sediment. As Kokelj et al. (2002) and Kokelj et al., (2005) investigated, soil properties like pH and electrical conductivity in addition with other parameters can help to identify paleo-thaw unconformities and the maximum active layer development (paleo-active layer depths) during different climatic conditions. Moreover, it is able to reveal effects of permafrost degradation on soil chemistry.

3.2.2.1 Determination of pH

Table 3.3 shows how sediments' reaction is subdivided according to their value of pH.

Tab. 3.3: Categorisation of reaction in subjection to its pH (SCHEFFER & SCHACHTSCHABEL, 2002, altered).

pH range	Characterisation
≥ 10.7	extremely alkaline
10.0 – < 10.7	very highly alkaline
9.3 – < 10.0	highly alkaline
8.6 – < 9.3	moderately alkaline
7.9 – < 8.6	weakly alkaline
7.2 – < 7.9	very weakly alkaline
6.8 – < 7.2	neutral
6.1 – < 6.8	very weakly acidic
5.4 – < 6.1	weakly acidic
4.7 – < 5.4	moderately acidic
4.0 – < 4.7	highly acidic
3.3 – < 4.0	very highly acidic
< 3.3	extremely acidic

Potentiometric measurements were carried out with the help of a pH meter (MultiLab 540, WTW). The device calculates the value of pH using the voltage between a glass and a reference electrode (HANDBOOK WTW, 1989) when the electrode is plugged into the

solution. A mixture of 10 g of dry but otherwise untreated sediment (<2 mm) and a 25 ml-solution ($H_2O_{deionised}$, 0.01 mol/l $CaCl_2$) was measured according to DIN 19684-1, DIN ISO 10390.

3.2.2.2 Determination of electrical conductivity

Nearly all solutions possess a certain content of total dissolved, dissociated electrolytes. This sum parameter of soluble inorganic anions and cations can be assumed to be responsible for the electrical conductivity (K) of a liquid sample (HÖLTING, 1996), which is defined as the reciprocal of electric resistance (R).

$$K = \frac{1}{R} \quad [S \times cm^{-1}]$$

The higher the concentration of ions, the higher is the electrical current created by the movement of ions between two electrodes (HANDBOOK WTW, 1993).

A subsample of 10 g of dry (<2 mm) sediment and 25 ml of deionised water ($H_2O_{deionised}$) (AD-HOC-AG BODEN, 2004) was stirred well and abandoned for 24 hours (DIN 19684-1, DIN ISO 10390). Next day supernatant water was extracted with a pipette and measured immediately with the conductivity electrode. Since 25 ml did not give enough supernatant water for peaty samples, 75 ml were used. Conductivity values were recalculated by the empirically-found factor of 2.08 (standard deviation: 0.19) to make results relatively comparable with those measured within 25 ml samples.

3.2.3 Stable isotope geochemistry

3.2.3.1 Oxygen & Hydrogen isotopes (^{18}O, ^2H)

Scientific background

Oxygen owns three stable isotopes in a globally stable proportion, whereas ^{16}O holds 99.76 % compared to a share of 0.04 % and 0.20 % for the heavier isotopes ^{17}O and ^{18}O, respectively. The stable deuterium isotope (^2H = D) occurs with an abundance of 0.02 % in comparison to ordinary hydrogen atoms (^1H). Although, these proportions are stable against the background of the global water cycle, they can differ significantly due to changes in regional temperature and humidity as well as phase changes of water (EPSTEIN & MAYEDA, 1953) (Fig. 3.3).
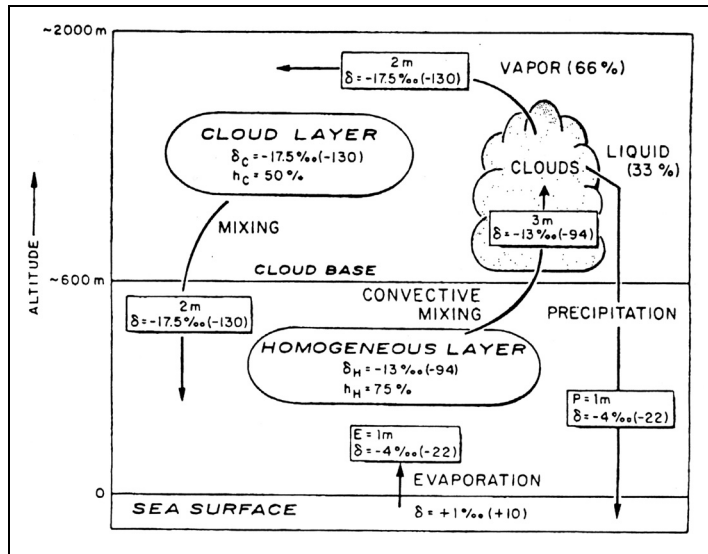
Fig. 3.3: The Craig and Gordon model (1965) for the isotopic composition of atmospheric water vapour over the oceans. δ-values in ‰ are presented for ^{18}O (δD in parentheses); relative mass fluxes are given in metres of water (CRAIG & GORDON, 1965; cited in CLARK & FRITZ, 1997, p. 46).

According to Fig. 3.3 the isotopically uniform and well mixed oceans serve as the main moisture source as well as they provide the initial isotopic composition of ±0 ‰, termed as standard mean ocean water (SMOW). Isotopic fractionation processes between the light and heavy components are strongly temperature dependent (DANSGAARD, 1964), which lead to a deviation from the initial equilibrium value that is expressed as δ-value in per mille against SMOW.

$$\delta D = {}^{2}H / {}^{1}H$$
$$\delta^{18}O = {}^{18}O / {}^{16}O$$

Positive δ-values suggest a relative enrichment of heavy isotopes towards SMOW, whereas negative values show a relative depletion against SMOW (GAT, 1996). Since there exists a strong correlation between $\delta^{18}O$ and δD in fresh waters, Craig (1961) showed this relationship by establishing the Global Meteoric Water Line (GMWL), expressed as:

$$\text{GMWL:} \qquad \delta D = 8 \times \delta^{18}O + 10 \text{ ‰ SMOW}$$

Isotopic fractionation processes are the result of different strengths of chemical bonds while the bond involving the lighter isotope is usually weaker and therefore easier to disintegrate (GAT, 1996). There exist several fractionation processes involving $\delta^{18}O$ and δD leading to a relative enrichment/depletion of heavy/light isotopes in a solid, liquid or gaseous system as well as to displacements in slope and d-excess, respectively. Fractionation processes are strongly temperature-dependent since they are thermodynamic reactions.

This leads to four general expressions concerning isotopic behaviour in the study area.

(1) Isotopically depleted meteoric waters are associated with cold regions.

(2) According to the Rayleigh rainout, continental areas receive isotopically more depleted precipitation than regions close to the vapour source.

(3) Areas of high latitude receive isotopically more depleted precipitation than areas of lower latitude.

(4) High altitudes favour isotopically more depleted precipitation than lower elevations.

Dansgaard (1964) first introduced the term "*d-excess*" as a parameter regarding Craig's GMWL to characterize the deuterium excess in global precipitation, which describes the deviation from the GMWL due to kinetic (non-equilibrium) effects accompanying evaporation from the ocean surface, as consequence for ^{18}O being more sensitive to kinetic fractionation than D.

$$d = \delta D - 8 \times \delta^{18}O$$

On a global scale the d-excess is close to 10 ‰ SMOW (see Craig's GMWL) but varies regionally due to changing humidity (most effective), wind speed and sea surface temperature (SST) during initial evaporation over the oceanic vapour source (CLARK & FRITZ, 1997; JOUZEL et al. 2007). This leads to the formation of a site specific Local Meteoric Water Line (LMWL), which shows deviant values of slope and d-excess. These values provide further information about the evolution of precipitation (DANSGAARD, 1964) and secondary changes. When humidity is low, d-excess will become high and vice versa (MERLIVAT & JOUZEL, 1979; JOUZEL et al., 1982).

Another important parameter that describes the linear relation between δD and δ^{18}O is the *slope (s)* of the linear regression line (MERLIVAT & JOUZEL, 1983). Differences in vapour pressures account for the enrichment of ^{2}H (D) in water during evaporation, which is roughly **8** times greater than for ^{18}O (see Craig's GMWL) under equilibrium conditions (CLARK & FRITZ, 1997; JOUZEL et al., 1997). The slope largely depends on relative humidity at vapour formation over the ocean but can also be affected by secondary evaporation. At low humidity, kinetic fractionation is maximised and thus the slope will be lower than 8 (CLARK & FRITZ, 1997).

Since this study deals with ground ice rather than ice caps or oceanic water bodies, it is important to keep in mind that Rayleigh distillation also occurs in continental water

reservoirs. As a main general implication, meteoric waters are depleted in heavy stable isotopes while waters in evaporative systems such as soils and lakes are relatively enriched (GAT, 1996).

In the solid-liquid system isotope fractionation occurs in a similar manner as noted for the liquid-gaseous system. Heavy isotopes are preferentially enriched in the ice whereas the remaining water becomes relatively depleted (MICHEL, 1982). If freezing rates exceed 2 mm per hour, a significant decrease in fractionation occurs so that it can be neglected (MICHEL, 1982; MACKAY, 1983).

This assumption provides a very important tool for paleo-temperature reconstructions using massive ice bodies, especially ice wedges that are fed by meteoric waters and thus preserve conditions of water mass formation during rapid freezing in the wedge's crack.

Principle of analysis

A Finnigan MAT Delta-*S* mass spectrometer was used for determination of deuterium (δD) and oxygen ($\delta^{18}O$) isotopic contents connected with two equilibration units (MS Analysentechnik, Berlin). The principle of measuring different isotopic contents within a sample is based on mass spectrometric detection of atoms with different mass that cause specific ion beams and motions in a magnetic field (HOEFS, 1997).

Measurements for deuterium and oxygen could be performed on a single sample aliquot. The equilibration technique is based on Horita et al. (1989). Each unit was kept in a water shaking bath with a constant temperature (18°C ± 0.01°C) to prevent condensation and therefore isotopic fractionation within the flasks. A platinum coated stick is used as catalyst to ensure and accelerate hydrogen isotope exchange. In a similar manner, the equilibration procedure for oxygen is done, using CO_2 as equilibration gas without a catalyst (MEYER et al., 2000). As the first position of each unit is assembled with the laboratory reference standard NGT1 (snow of the *North Greenland Traverse*), which is transferred into the standard bellow after equilibration, it serves as reference standard for the whole unit. Thus, sample and standard gas are alternately introduced into the mass spectrometer and measured against the standard gas.

The values of $\delta^{18}O$ and δD are calculated against the global reference standard VSMOW (Vienna Standard Mean Ocean Water) with the help of the commercial software ISODAT® and are subsequently displayed as the relative ‰-difference to this standard. For the oxygen ratio it follows:

$$\delta^{18}O_{sample} = [(R_{sample} - R_{standard}) / R_{standard}] \times 1000 \text{ ‰ VSMOW} ,$$

while R represents the particular ratio ($^{18}O / ^{16}O$) of the sample and the reference standard (VSMOW), respectively.

Three standards per unit were used for quality control and to ensure that the measured values are representative. This leads to the awareness that the internal accuracy is generally better than 0.8 ‰ for δD and 0.1 ‰ for $\delta^{18}O$.

3.2.3.2 Carbon isotopes (^{13}C and ^{12}C)

Scientific background

Plant growth in general reflects environmental conditions during their growth period and sometimes keeps these information post mortem. Analysing organic sedimentary properties may provide information about prevailing temperature regime, the availability of water in a landscape, soil properties (e.g. supply of nutrients, pH) as well as about biogeochemical mechanisms of decay.

Natural carbon consists of three isotopes in different proportions, whereas ^{12}C (98.89 %) and ^{13}C (1.11 %) occur as stable forms in contrast to ^{14}C (1×10^{-12} %) being radioactive (WAGNER, 1995; WILLKOMM, 1976). Since isotopic fractionation processes occur during metabolism of living plants as well as during decomposition after their death, the analysis of stable carbon isotopes provides a useful tool for the reconstruction of paleoenvironmental conditions of areas plants lived in and are laid down, respectively (DEGENS, 1969). The abundance of carbon isotopes in a given sample is usually stated by the ratio of ^{13}C to ^{12}C-atoms, reported as ‰-difference against the international reference standard PDB, regularly expressed as $\delta^{13}C$ (CRAIG, 1953; DANSGAARD, 1953),

$$\delta^{13}C_{sample} = [(R_{sample} - R_{standard}) / R_{standard}] \times 1000 \text{ ‰ PDB} ,$$

while R represents the particular ratio ($^{13}C / ^{12}C$) within the sample and the reference standard (PDB), respectively.

Plant remains are divided into two geochemically distinct groups on the basis of their biochemical compositions. (1) Vascular plants, living typically on land and as emergent plants in shallow waters only, contain woody and cellulosic tissue. (2) Non-vascular plants can be found mainly in the water column, such as algae, and lack these kinds of tissue (MEYERS & ISHIWATARI, 1993). During photosynthesis a kinetic effect occurs, leading to

an enrichment of ^{12}C in organic matter against the atmospheric isotopic composition (e.g. DEGENS, 1969; HOEFS, 1987). Most photosynthetic plants incorporate carbon into organic matter using the C_3 Calvin-Benson pathway, which preferentially incorporates ^{12}C into organic matter, leading to a significantly negative shift from the isotope ratio (MEYERS, 1994, 1997). Other plants use the C_4 Hatch-Slack pathway producing negative shifts from the isotope ratio but to a lower degree (MEYERS & ISHIWATARI, 1993). Most C_3-plants have $\delta^{13}C$ values that range from −24 ‰ to −30 ‰ in contrast to C_4-plants having $\delta^{13}C$ values between −10 ‰ and −16 ‰ (MEYERS, 1994, 1997; MEYERS & LALLIER-VERGÈS, 1999; GLASER, 2005).

In general, terrestrial C_3 plants own the most negative $\delta^{13}C$ values followed by mostly aquatic plants (e.g. algae), whereas marine organisms, especially carbonate incorporating communities are further isotopically enriched due to the uptake of isotopically enriched bicarbonate ions (HCO_3^-) (HOLLERBACH, 1985).

Principle of analysis

The determination of stable carbon isotopic composition were carried out with a combination of an elementar analyzer (Flash EA 1112 Series, Thermo Finnigan), a CONFLO III gas mixing system and a Thermo Finnigan MAT Delta-*S* mass spectrometer. The first device acts an oven based on catalytic tube combustion by means of oxygen supply at high temperatures (see ch. 3.2.1.3) producing the sample gas (CO_2) for further mass spectrometric determination of carbon isotopic ratios. In order to measure the isotopic composition of organic remains only, samples free of carbonate were used, as described in chapter 3.2.1.3. The calculated sample weight $\left[m\ [g] = 45\ /\ TOC\ [g] \right]$ was encapsulated in tin capsules and released to the analyzer via autosampler system. Measuring control standards and performing repeated determination after every seventh measurement ensures correct analytical values.

After combustion at about 950°C, CO_2 is induced into the sample tube of the mass spectrometer while other gases (byproducts) are reduced. A standard gas (CO_2) of known isotopic composition is measured against the sample gas to determine the isotopic ratio. After ionisation of the CO_2, the ions are accelerated and focused into a single beam. Ion beams are separated according to their mass, and an electrical current is released and detected. The mass specific current peaks are recalculated in order to record the single isotopic contents and their ratio δ ($^{13}C\ /\ ^{12}C$), too (DANSGAARD, 1953; DEGENS, 1969).

Measurements at AWI Potsdam are reproducible with an accuracy generally better than ±0.15 ‰.

In order to report the measured values in an international comparable system, $\delta^{13}C$ of the sample is given in ‰-difference relative to V-PDB[1].

3.2.4 Age determination

Organic matter was picked out of selective sediment samples for radiocarbon dating via accelerator mass spectrometry (AMS) at the Leibniz-Laboratory for Radiometric Dating and Stable Isotope Research in Kiel.

Dating of autochthonous organic remains in the adjacent deposits gives evidence about the minimum point in time the sedimentary layer was deposited. In addition, age determination of autochthonous and not relocated sediments in correlation with depth may yield an average rate of sediment accumulation.

The analytical principle is based on the fact that radioactive carbon isotopes (^{14}C) are produced in the upper atmosphere by the reaction of nitrogen atoms (^{14}N) with solar neutrons. In connection with oxygen, ^{14}C nuclides form $^{14}CO_2$ – next to the stable forms of $^{13}CO_2$ and the most abundant $^{12}CO_2$ – and are applied to the global carbon cycle (e.g. photosynthesis) (WIGLEY, 2000). Living organisms hold the same isotopic ratio like the atmosphere since they all are in equilibrium with the atmosphere by their metabolism. This equilibrium shuts down when organisms die so that the radioactive ^{14}C nuclides decay to ^{14}N with a half-life time of 5730 years while no further nuclides can be incorporated.

On the basis of Libby (1952), the period of time since death – described as the radiocarbon age – can be calculated on the basis of following equation,

$$t = \ln (^{14}C_{t=0} / {}^{14}C_{t=1}) / \lambda \qquad (\lambda = \ln2 / t_{1/2})$$

while t is the calculated age, $^{14}C_{t=0}$ is the original ^{14}C content, $^{14}C_{t=1}$ is the ^{14}C content after a certain time span and λ is the decay constant (CLARK & FRITZ, 1997), described as the natural logarithm of 2 divided by the half-life time ($t_{1/2} = 5730$ a). There exists a detection

---

[1] Since the formerly used standard gas (CO_2), which derived from a Cretaceous belemnite (Belemnitella americana) from the Peedee formation in South Carolina, U.S., is almost exhausted, the International Atomic Energy Agency (IAEA) produced a synthetic standard with PDB isotopic characteristics, known as V-PDB (Vienna-PDB).

limit due to the specific half-life time of radiocarbon. Despite special enrichment techniques and the possibility of using very small sample volumes, the AMS dating method has a limit of 40-50 ka, not exceeding 60 ka at its best (WAGNER, 1995).

Radiocarbon ages are reported in years *Before Present* (BP) on the base year 1950 AD. A calibration data set based on dendrochronology and uranium/thorium series on corals is used to convert conventional radiocarbon ages into calendar ages, stated as *cal BP* (STUIVER & REIMER, 1993; WIGLEY, 2000).

The yielded dates are considered to serve as a first orientation since not all profiles have been dated and there are mostly large gaps between the dated horizons in a very complex stratigraphy of Herschel Island.

4 RESULTS

This chapter comprises the results of the laboratory analyses compiled for each study site, which in turn sometimes contains several outcrops or sub-profiles. Sediment samples as well as ground ice samples of different genetic origin were taken at every outcrop, except at study site *HI-GI* (see ch. 2.4.1.3), where a massive ground ice body was recovered only. Therefore, a sub-chapter towards the characterisation of sedimentary and ground ice properties is implemented each. On the one hand, results regarding sedimentary properties cover all quantitatively measured parameters, i.e. the gravimetric ice content, magnetic susceptibility, grain size distribution, biogeochemical parameters (TOC, TC, TN, C/N-ratio), as well as values of $\delta^{13}C$, pH, electrical conductivity and ^{14}C-age determinations. On the other hand, this sub-chapter also includes qualitative information about the horizon's stratigraphic placement within the sediment body, statements about bedding, cryostructure, colour and about the presence or absence of coarse-grained material.

The ground ice paragraph includes quantitative data towards the isotopic composition of ice and waters as well as qualitative remarks − if suitable and necessary − to describe the different types of ground ice regarding colour, existence of organic matter, width and height of ice veins and ice wedges in addition to their allocation in the surrounding sediments. Information about spatial elongation, sediment content, and the content, orientation, and size of bubbles within the icy body might be added. Samples from the outer rim of an ice wedge may have undergone secondary exchange processes with the adjacent sediment (MEYER et al., 2002a). Consequently, these values have been left out from calculations of the mean isotopic composition as their isotopic composition might not reflect climatic trends. Unfortunately, it was not possible to gain supernatant water from all sediment samples after thawing due to low ice contents, so that for those there are no values available. Detailed information on every single sample can be obtained from Appendix 1 (sediments) and Appendix 3 (ground ice).

4.1 Collinson Head No.1 (COL 1)

4.1.1 Sediments (COL 1)

Profile COL 1 (Fig. 4.1) has an undisturbed surface since the outcrop lies within a retrogressive thaw slump that was obviously not affected by previous slump activity. With a thickness of 30-40 cm the outcrop holds a shallow active layer, which is characterized by low values of pH near 5.
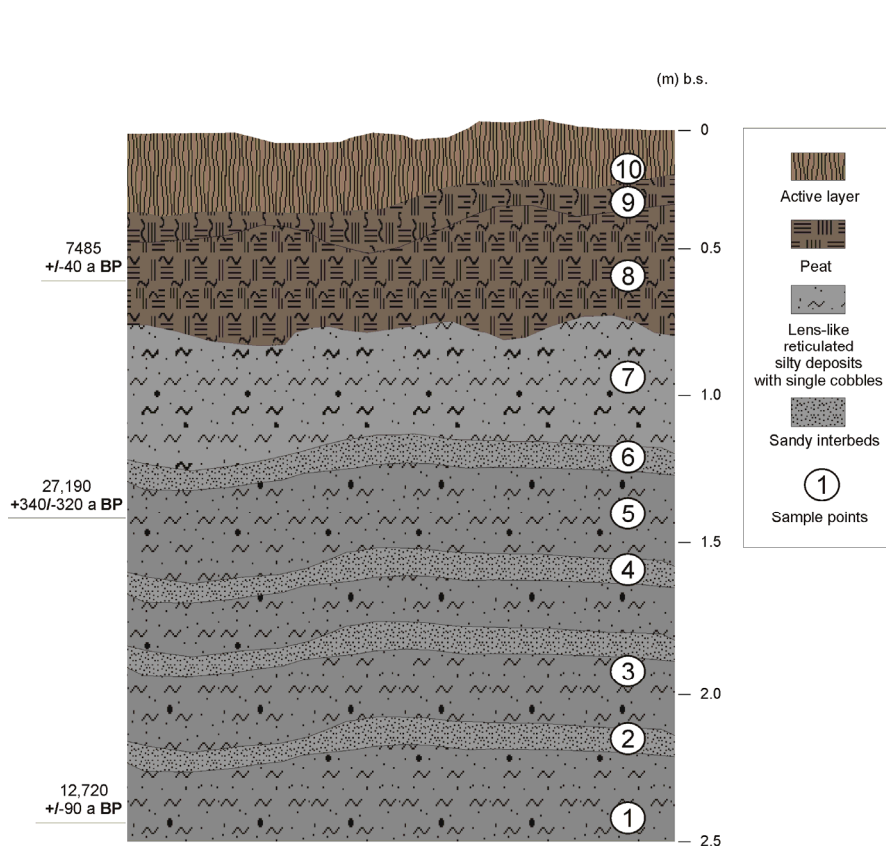
Fig. 4.1: Profile COL 1.
Numbers indicate the sample points.

The lowermost unit (Unit A) is greyish-brown in colour with a lens-like cryostructure, no more peat occurs but cobbles are present from ~ 0.6 m down. The upper sequence (Unit B) beneath the active layer is peaty, dark brown in colour and very ice-rich having a lens-like reticulated cryostructure and a gravimetric ice content of 137-365 %. The magnetic susceptibility shows low values throughout the profile ranging from 12 to 23 SI $(10^{-8}\,\mathrm{m^3 kg^{-1}})$ with mean values about 17 SI (Fig.4.2) having its maximum at ~1 m below

surface (b.s.). The whole profile mainly consists of a diamicton; i.e. very poorly sorted[2] (2.2 to 3.3) sandy silts to silty loams (according to AD-HOC-AG BODEN, 2004) with a qualitative fraction of single pebbles and cobbles. Grain size fractions greater than 2 mm are not included in any profiles' distribution graphic but qualitatively mentioned. A main peak in the grain size distribution curve occurs in the fine silt fraction with a minor peak in fine sand fraction (Fig.4.3). The mean grain size ranges from 6 to 25 μm..

Fig. 4.2: Summary of physical, biogeochemical and stable isotope parameters for profile COL 1. Age determinations are annotated next to the horizon they were sampled in and are recorded as uncalibrated ^{14}C years BP. Different grey scales mark distinctive units within the profile. Note that the mean grain size is plotted as rhombi within the grain size fraction pattern.

Also regarding the contents of TOC, it becomes obvious that the profile is divided into two sections. The lower part (Unit A) between 2.4 m until about 1 m b.s. has low TOC contents between 1.1 and 1.6 % whereas the upper section (Unit B) owns values ranging from 5 to 12 % with a maximum at ~ 1 m below surface (b.s.). At this certain depth there is a distinct change of many parameters (besides TOC) that have been measured (Fig. 4.2).

(1) C/N-ratios rise from values of about 12 to 16 and decreases again.

(2) Electrical conductivity decreases from about 500 to 360 μScm^{-1} while pH-values decrease from 7.7 towards values between 5 and 7.

(3) CaCO$_3$ occurs in depth (c3) as it was estimated according to Ad-hoc-AG Boden (2004) with the help of a pre-test using a small amount of dry sediment and HCl (10 %) (see ch. 3.2.1.3 − Tab. 3.2).

---

[2] Sorting was computed after Inman (1952): $So = \dfrac{\phi 84 - \phi 16}{2}$

(4) Values of $\delta^{13}C$ rise at this significant depth from about −26.5 ‰ to −26.0 ‰ and
remain relatively stable within the discrete divisions.

Fig. 4.3: Grain size distribution of profile COL 1.
Left inset shows the very poorly sorted and bimodal character of all horizons. The sediment triangle after
Shepard (1954) depicts the clayey but silt-dominated character with slight variations within the profile.

Radiocarbon dating at 0.6 m b.s. yielded an age of 7485 ±40 a BP. Organic matter from the
basis of the profile at 2.4 m b.s. shows an age of 12,720 ±90 a BP and dated material at 1.4
m b.s. with an age of some 27 ka BP reveals a distinct inversion that will be taken into
closer consideration in chapter 5.

4.1.2 Ground ice (COL 1)

As a standard procedure to combine sedimentary, cryostratigraphic and stable isotope
studies, ground ice recovered from the sediment profile is usually used for determination of
pH, electrical conductivity as well as for oxygen and hydrogen stable isotope analysis. A
δD-$\delta^{18}O$ scatter diagram in Fig. 4.4 shows the isotopic composition of ice throughout the
profile, while oxygen isotopic variations with depth are shown in Fig. 4.2. It becomes
obvious that there is a gradual transition from lower $\delta^{18}O$ (−22.9 ‰) and δD values (−173
‰) at the basis towards higher ones near the surface (−17.2 ‰, −129 ‰). With a slope of
8.0 and a d-excess of 9.4 ‰ the samples lie almost exactly on the GMWL (Fig. 4.4).
Ice wedges have been recovered and sampled in addition to segregation ice. Within a
distance of 100 m and intervals of 20 to 30 m four ice wedges were spotted alongside the
headwall of the retrogressive thaw slump, so that the diameter of polygons is the same as
the distance between the ice wedges. A representative, 3.1 m wide ice wedge (HI-IW-1)
was taken into closer consideration. It is made of milky-white ice that is rich in bubbles
and organic remains but has a low content of dispersed sediment. Moreover, the wedge

cuts off with the base of the active layer in the surrounding sediment. A 2 cm thick slice was cut off the ice wedge in a horizontal transect every 10 cm for isotope analyses. Values for δ^{18}O and δD lie within a narrow range between –21.1 ‰ and −19.4 ‰ and between −162 ‰ and −146 ‰ for δD, respectively (Fig. 4.4). Moreover, HI-IW-1 has a slope of 7.2 and ranges in d-excess between 6.0 ‰ and 10.2 ‰ with an average of 8.7 ‰, what is close to the GMWL.

Texture ice obtained from sediment samples show great variations throughout the profile, whereas the ice wedge exhibits minor variations.
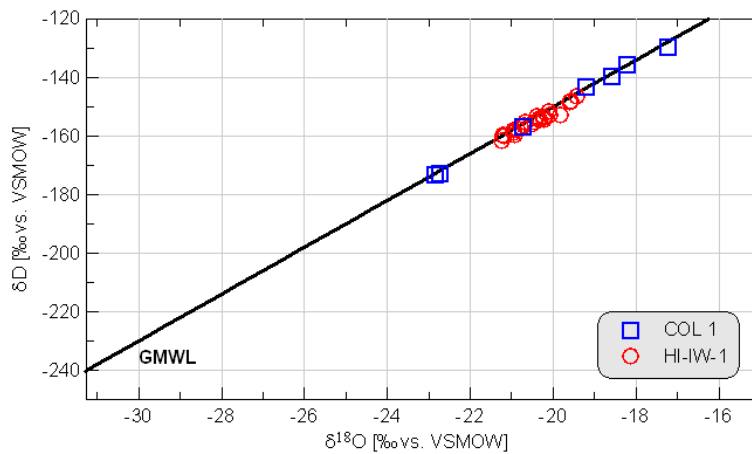
Fig. 4.4: δD-δ^{18}O diagram for COL 1 (texture ice) and HI-IW-1 (ice wedge ice).
Note that both data sets fit the GMWL.

4.2 Collinson Head No.2 (COL 2)

As mentioned in ch. 2.4.1.1, the sample site was previously affected by creep and/or former cycles of slump activity. Because of limited accessibility, a continuous sediment profile could not be sampled at the headwall. Thus, three partial profiles were sampled with overlapping intervals (*Profile 1, Profile 2, Profile 3*) between them to cover the whole height of the headwall (Fig 4.5).

1 − Active layer: 30-40 cm
2 − Transition horizon: brown, 50 cm
3 − Greyish-brown, very ice-rich, coarse cryotexture, peat pods
4 − Massive icy sediments, very ice-rich, banded and partly contorted cryostructure
5 − Very ice-rich, pressed up as a fold, cobbles incorporated
6 − Bedded, fine-grained, massive cryostructure
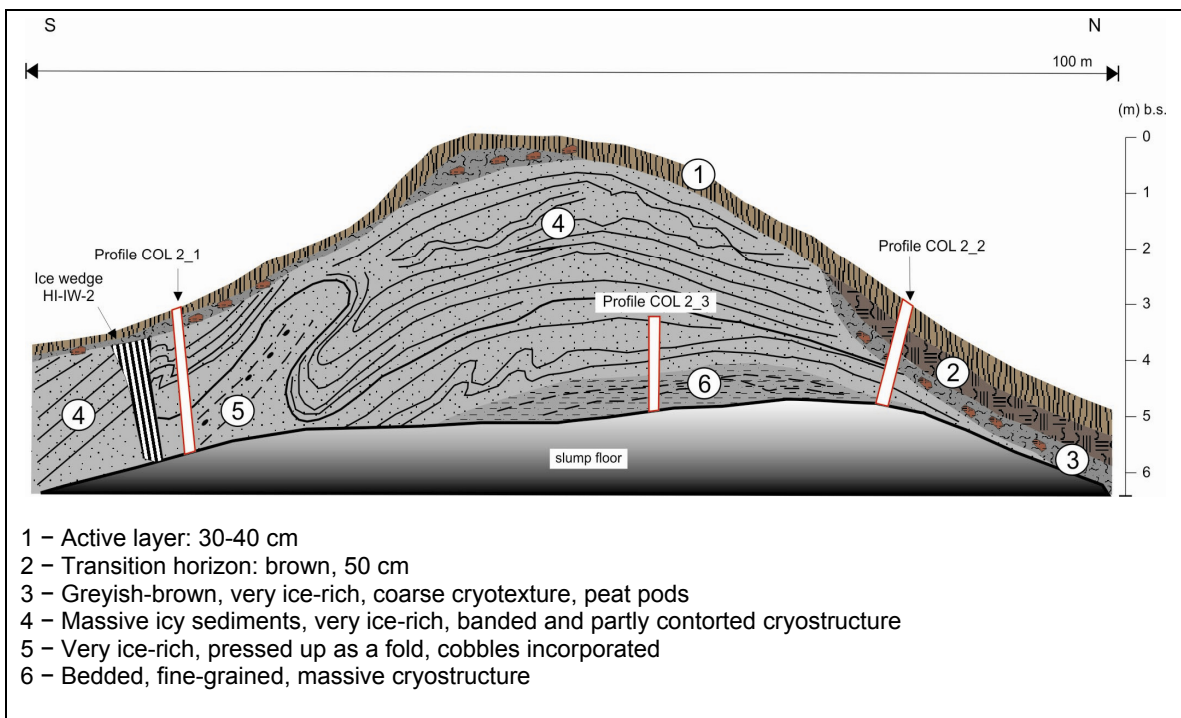
Fig. 4.5: Thaw slump at Collinson Head 2.

4.2.1 Sediments (COL 2)

Profile 1 (COL 2_1)

The first profile is situated towards the left margin of the slump (Figs. 2.15, 4.5) and covers a continuous sequence from 3.5 m to 0.6 m below surface on the right hand side of an adjacent ice wedge sampled (HI-IW-2) (Fig. 4.6).

Cryostructures are very complicated and vary strongly within the profile. The lowermost part (Unit 1) looks dark grey and is very ice rich. Texture ice basically occurs as ice bands, which are partly folded, probably as a result of deformation by mass wasting processes such as gelifluction, active layer detachments or slumping. The uppermost layer directly below the active layer has a horizontal lens-like reticulated cryostructure whereas the layer

below possesses subvertical ice veins although both beds are very similar in their sedimentary characteristics.
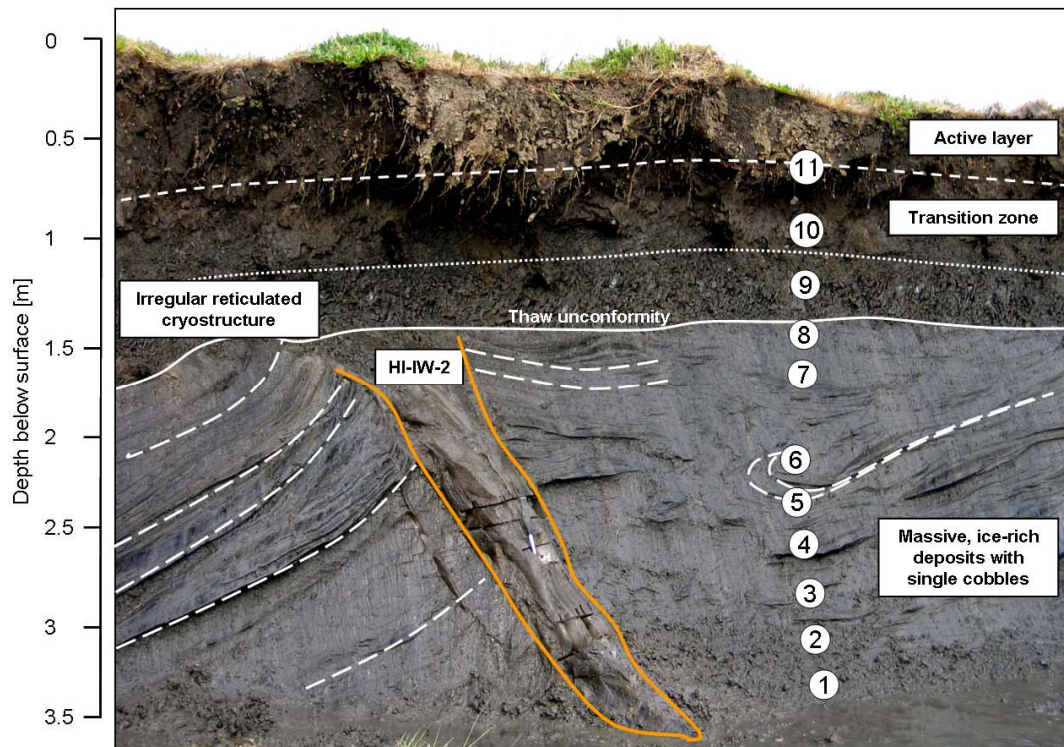
Fig. 4.6: Profile COL 2_1.
Numbers indicate the sample points. Solid white line marks the thaw unconformity. Orange line borders the ice wedge (HI-IW-2).

Both are greyish green in colour and are enriched in well-rounded to subangular cobbles up to 8 cm. The active layer reaches a depth of 0.7 m but has otherwise no remarkable features that distinguishes this stratum from the next directly beneath.

The whole profile has a relatively high $CaCO_3$ content (c3) that is underlined by pH-values above 7.1 and shows a high electrical conductivity of generally more than 1500 μScm^{-1} in contrast to profile COL 1 were most values remain below 500 μScm^{-1}. At a depth of ~1.5 m b.s. there exists a distinct boundary in terms of cryostructure and sedimentary properties (Figs. 4.6, Fig. 4.7).

(1) The gravimetric ice content decreases above the discontinuity, however, the transition horizons are very ice-rich (~100 %).

(2) A step in susceptibility occurs from 35 to 26 SI, although on a still low level.

(3) Between Unit 1 and Unit 2, the grain size distribution pattern shows a distinct rise in the clay content by 12 % and a parallel drop in sand content by 11 % with a likewise decline in mean grain size (Fig. 4.7).
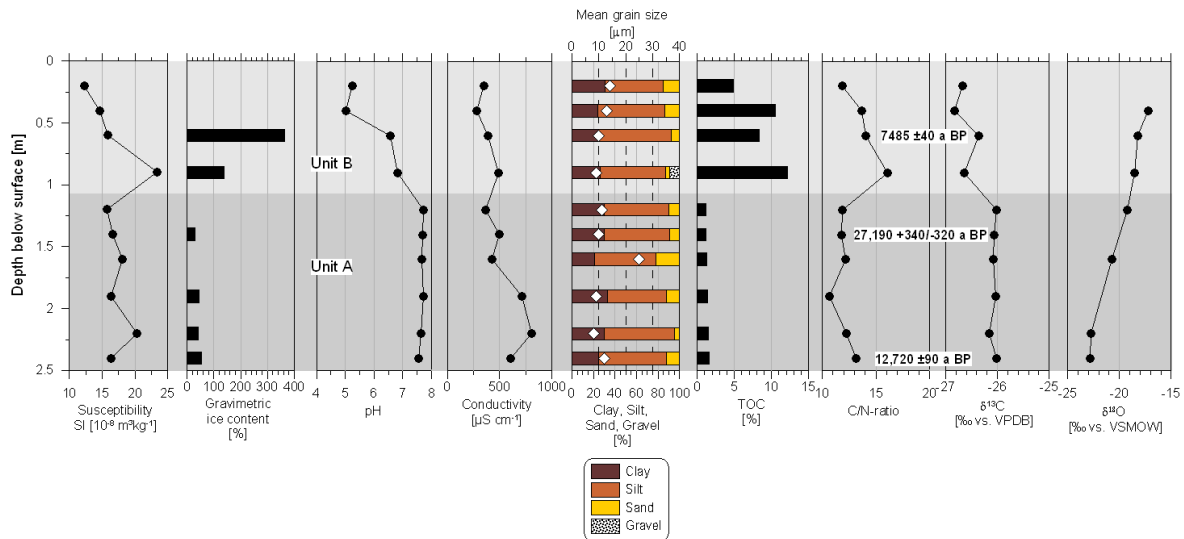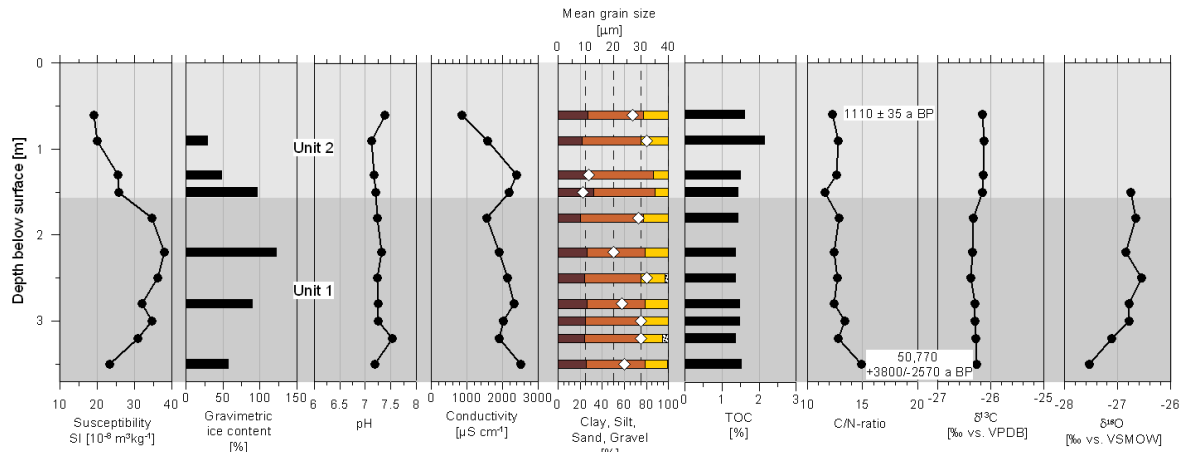
Fig. 4.7: Summary of physical, biogeochemical and stable isotope parameters for profile COL 2_1.
Age determinations are annotated next to the horizon they were sampled in and are recorded as uncalibrated ^{14}C years BP. Different grey scales mark distinctive units within the profile. Note that the mean grain size is plotted as rhombi within the grain size fraction pattern.

But in general, the profile is strongly dominated by silt-sized material with the above mentioned variations in sand and clay content. Although not every horizon contained skeletal soil, especially the part between 1.5 and 2.5 m b.s., the matrix-based diamicton usually consists of very poorly sorted (2.6 to 3.5) silty loams with a sometimes variable content of granules, pebbles and cobbles. The figure of grain size distribution (Fig. 4.8) shows a bimodal to trimodal character with a main peak in the fine silt fraction, a minor peak in fine sand and sometimes a third peak in coarse silt to very fine sand. Both median and mean grain size with values ranging from 8-14 μm and 9-32 μm, respectively, support the silty character of the whole profile.

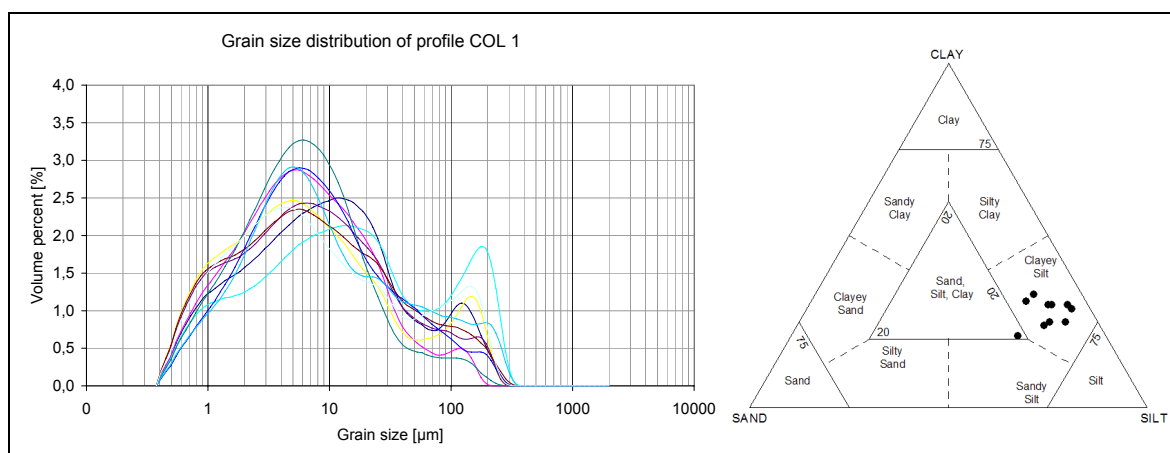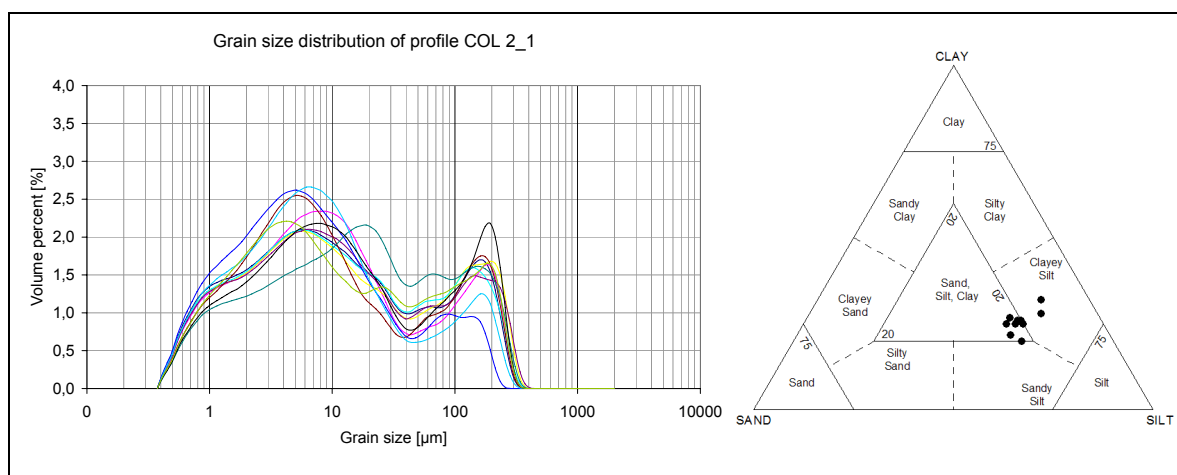**Fig. 4.8**: Grain size distribution of profile COL 2_1.
Left inset shows the very poorly sorted character of all horizons. The sediment triangle after Shepard (1954) exhibits the silt-dominated character although all grain size fractions are present to a significant degree.

Biogeochemical parameters show minor variations throughout the profile (Fig. 4.7). Organic carbon is present with 1.4 to 2.1 % by weight, leading to C/N-ratios of 12 to 15 without any remarkable trend within the profile. Stable carbon isotope analyses yielded extremely constant values of about −26.4 ‰ to −26.1 ‰ thus proposing a quite stable source of organic remains or an intense mixing process within the profile.

Radiocarbon dating from the basis of the profile at 3.5 m b.s. yielded a ^{14}C-age of 50,770 a BP (+3800/−2570 a), which represents the greatest age that was determined during this study. Another sample obtained 0.9 m b.s. shows a ^{14}C-age of 1110 ± 35 a BP.

Profile 2 (COL 2_2)

The second profile within the large retrogressive thaw slump is located on the right edge of the slump (Fig. 4.5) were the headwall was accessible up to the surface. A continuous sequence from 0.5 m to 3.0 m below surface was sampled (Fig. 4.9).
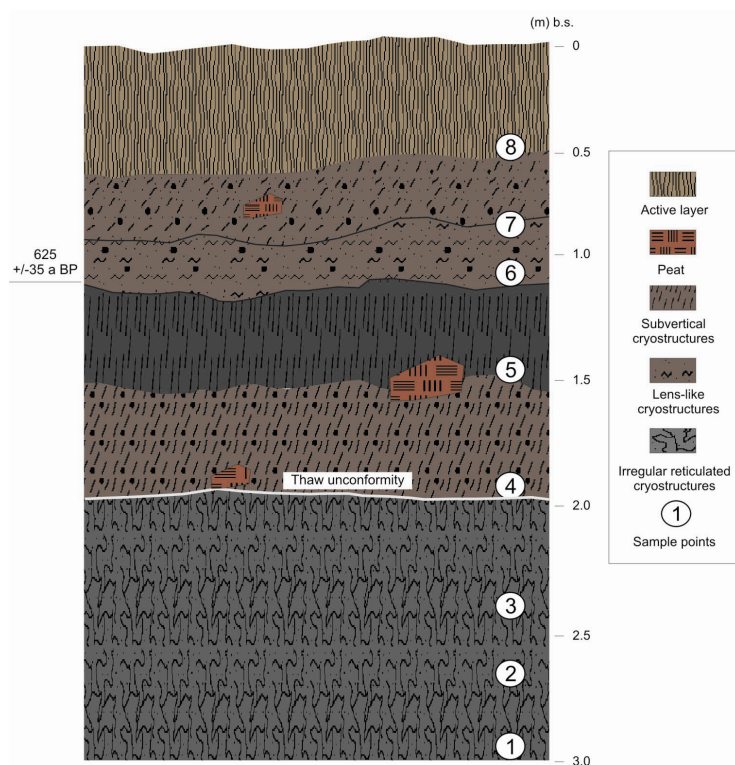
Fig. 4.9: Profile COL 2_2.
Numbers indicate the sample points. Solid white line marks the thaw unconformity.

Unit a comprises the lowermost metre of the profile that is grey to dark grey and has an irregular reticulated cryostructure and ice bands at the basis, respectively. This unit

represents a very ice-rich part of the profile with ice contents of around 80 % in contrast to the overburden, which holds less than 35 % ice.

The upper *Unit b* is generally greyish brown and extends from 2.0 m up to 0.5 m below surface. It is characterised by a horizontal to diagonal lens-like reticulated cryostructure and has a significantly higher content of sand (11-12 %) than the underlying material. It contains some peat and well-rounded pebbles (Fig. 4.9), that are absent in Unit a. At 1.5 m b.s. a weakly bedded, dark grey horizon without any peat or pebbles is intercalated underlain by a 20 cm thick horizon that is very similar to the remaining unit having peat inclusions, rounded cobbles up to 12 cm and a slightly higher TOC content (Fig. 4.10) as well as a minor drop in pH. These facts should be discussed in terms of a paleo-surface with pedogenetic processes.
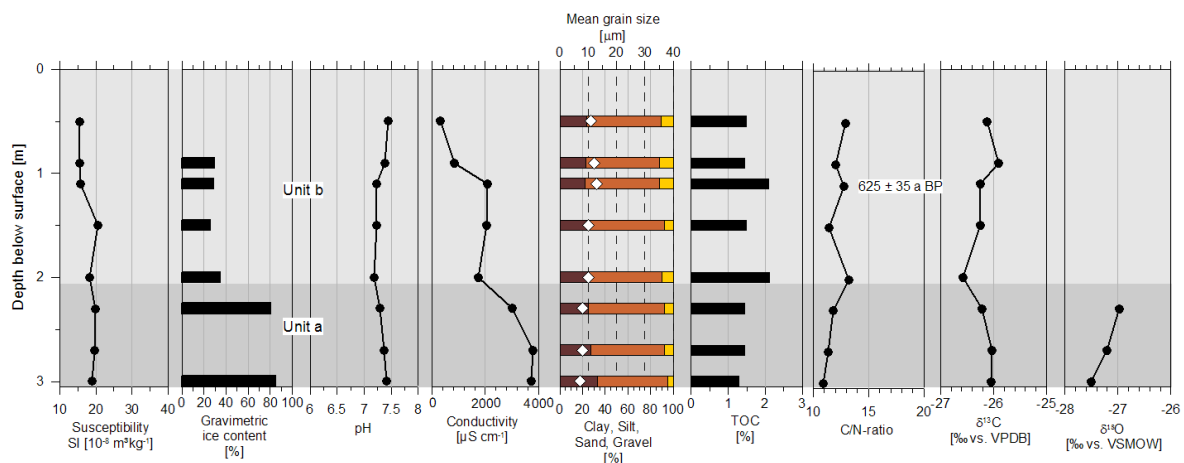
Fig. 4.10: Summary of physical, biogeochemical and stable isotope parameters for profile COL 2_2. Age determinations are annotated next to the horizon they were sampled in and are recorded as uncalibrated ^{14}C years BP. Different grey scales mark distinctive units within the profile. Note that the mean grain size is plotted as rhombi within the grain size fraction pattern.

Generally speaking, this profile is very similar to the previously mentioned one (Profile 1) in terms of sedimentary properties, however some differences are obvious that should be mentioned.

(1) Values of magnetic susceptibility (15-20 SI) and C/N-ratios (11-13) are somewhat lower and remain almost stable.

(2) There are two significant steps amongst the electrical conductivity profile. The values drop twice by more than 1000 µScm^{-1} at depths of about 2 and 1 m b.s. towards values of 3000 and 2000 µScm^{-1}, respectively (Fig. 4.10).

(3) Grain size distribution shows a generally higher content of silt by at least 10 % compared to *Profile 1* while the sandy peak is only less prominent and significantly lower (Fig 4.11). This leads to the classification as a very clayey silt in the lower part of the profile and the occurrence of a diamicton in the upper part.

Age determination at 1.1 m b.s. yielded a ^{14}C-age of 625 ±35 a BP.
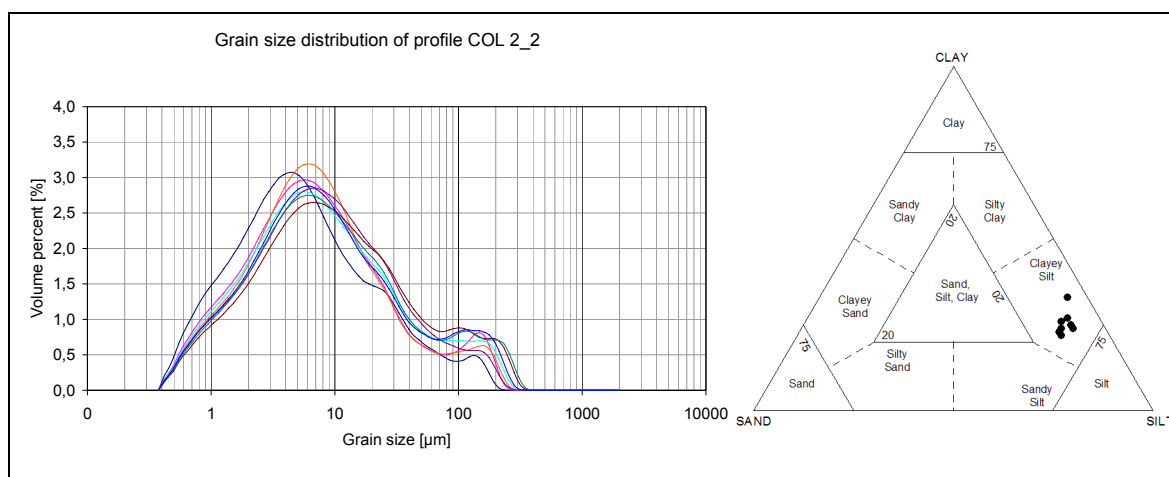
Fig. 4.11: Grain size distribution of profile COL 2_2.
Left inset shows the very poorly sorted character of all horizons. The sediment triangle after Shepard (1954) depicts the clayey but silt-dominated character with slight variations within the profile.

Profile 3 (COL 2_3)

The third profile was sampled at the central part of the slump's headwall (Fig. 4.5) beginning at the interface between slump floor and headwall (5.8 m b.s.) towards the top up to 2.9 m below surface. All samples were obtained from an ice-rich section well below the widespread observed unconformity, where segregated ice in the form of ice bands (lower part) and diagonal ice veins (upper part) is present.

Regarding sedimentary properties on the whole it becomes obvious that they seem very similar to the lower unit of *Profile 1* beneath the unconformity. Though, values of magnetic susceptibility (19-22 SI) are somewhat lower within the profile considered here, while C/N-ratios (11-13) remain within the same range (Fig. 4.12). TOC-values are low throughout the profile (1.2−1.6 %), $CaCO_3$ is present (c3) thus leading to pH-values above 7.3; and the gravimetric ice content decreases upwards (Fig. 4.12). δ^{13}C-values are quite constant and in the same range (−26 ‰ ± 0.2 ‰) as usually observed. Very poorly sorted

silty loams with a mean grain size between 20 and 31 μm prevail, thus leading to a diamictic appearance in combination with occurring pebbles.
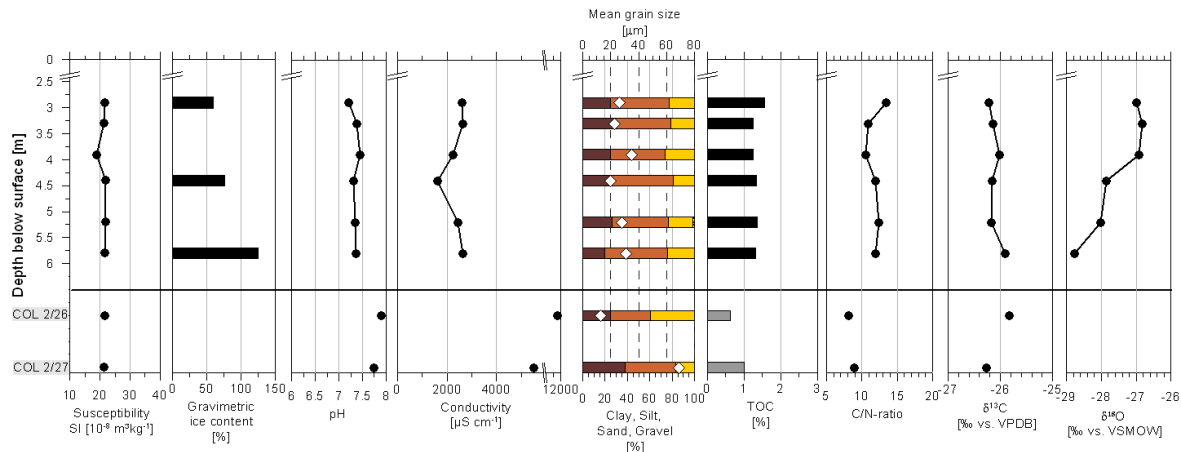
Fig. 4.12: Summary of physical, biogeochemical and stable isotope parameters for profile COL 2_3 including samples COL 2/26 & COL 2/27.
Note that the y-axis breaks between 0 and 2.5 m below surface. X-axis breaks within the conductivity plot as well.

Two further samples (COL 2/26, COL 2/27) were obtained within the retrogressive thaw slump in addition to the treated headwall that do not originate from a certain profile but from an escarpment within a narrow erosional valley (Fig. 2.15) near the end of the slump. Since both samples were taken near the slump's mouth, they are considered to be located relatively below all three profiles. Sample *COL 2/27* is dark grey, and contains lots of shells and shell fragments, thus indicating a marine origin. Moreover, it shows high values of pH (7.8) and electrical conductivity (5510 μScm^{-1}) in contrast to a low value of magnetic susceptibility (21 SI), C/N-ratio (9) and TOC content (1.0 %) as shown in Figure 4.12. This specific sample holds a comparatively low medium grain size, contains the highest content of clay (38 %) amongst all samples (Fig. 4.12) and is therefore classified as a marine mud with an apparently high carbonate content (c3.4).

At a position about 1.5 m higher than COL 2/27 but within the same gully, *COL 2/26* was sampled out of a greyish brown diamicton with abundant well-rounded pebbles and cobbles (⌀ 1-10 cm). This sample exhibits the lowest C/N-ratio by 8, the lowest content of TOC (0.6 %) and the highest value of electrical conductivity (11,500 μScm^{-1}) measured during this study. Furthermore, CaCO$_3$ is present (c3.3) but to a lower degree as it is in COL 2/27, the value of pH is highest (7.9) and magnetic susceptibility remains low at 21 SI. However, the most striking feature distinguishing this sample from others is its strongly

deviant grain size distribution. In addition to a greater mean grain size at about 70 μm, it holds large shares of all grain size fractions (Fig. 4.13) thus being the worst sorted (3.7) bed that was encountered during this study. There occur two peaks in grain size distribution. The first broad but relatively low one lies within clay and fine silt; the second peak is located within fine and medium sandy material and is very pointed (Fig. 4.13). This leads to a classification as a very poorly sorted and fine skewed medium sandy loam in contrast to all other samples uncovered in this slump which are normally coarse skewed or appear almost symmetrically.

Data of both additional samples are integrated in the figures 4.12 and 4.13 that describe subprofile No.3 to highlight differences as well as similarities between sequences of a most likely diverse genetic origin.
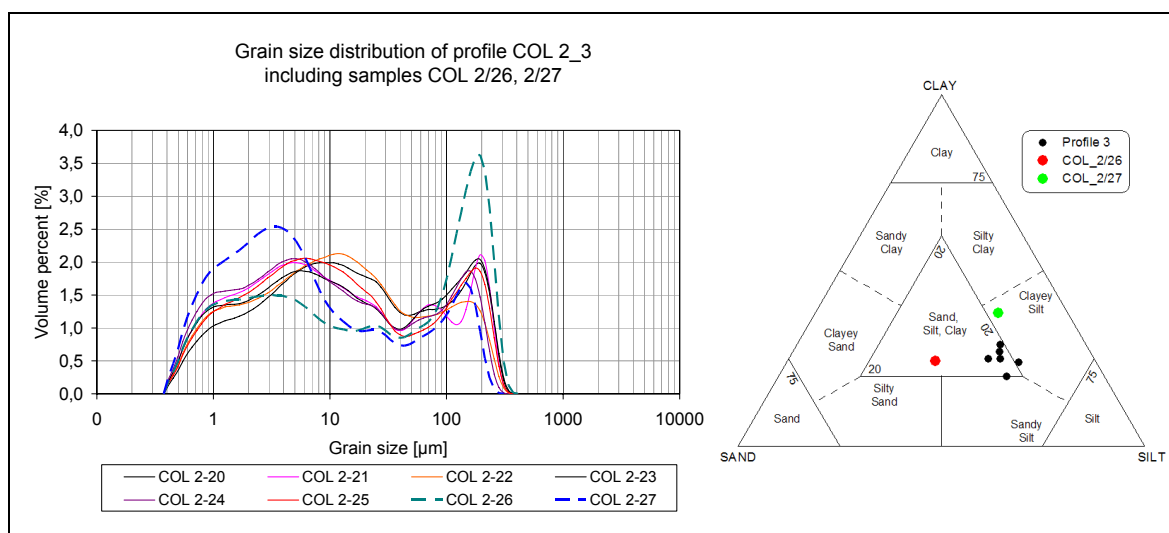
Fig. 4.13: Grain size distribution of profile COL 2_3 including samples COL 2/26 & COL 2/27.
Left inset shows the very poorly sorted character of all horizons and that COL 2/26 is more sandy in contrast to COL 2/27, which exhibits a higher clay content. The sediment triangle after Shepard (1954) depicts the silt-dominated character although all grain size fractions are present to a significant degree.

4.2.2 Ground ice (COL 2)

The δD-$\delta^{18}O$ scatter diagram (Fig. 4.14) shows the isotopic composition of texture ice throughout the three subprofiles, also in comparison to a parallel sampled ice wedge that will be addressed in the course of this chapter. Additionally, oxygen isotopic variations are plotted against depth (Fig. 4.15) to examine if there may exist a relationship between the formation of ground ice in deeper strata and the preservation of paleotemperatures in the $\delta^{18}O$ value. In contrast to isotope data from profile *COL 1* (Fig. 4.2), all samples measured here, reveal that there is only a minor, even a neglectable transition from lighter values at

depth towards slightly more positive values near the surface besides the fact that texture ice from COL 2 exhibits much lighter values than ice of COL 1 does. Values of $\delta^{18}O$ (δD) range between -28.8 ‰ (-225 ‰) at depth and -26.8 ‰ (-209 ‰) near the surface (Fig. 4.15).

A slope of 7.1 and a low d-excess of 3.3 ‰ indicate that the samples lie below the GMWL and that either secondary non-equilibrium processes after precipitation, for example repeated phase changes, or somehow anomalous conditions at the initial vapour source changed the isotopic signal.

An epigenetic ice wedge (HI-IW-2) within the ice rich sediments of profile No.1 was recovered and sampled in two horizontal transects (Fig. 4.6). The wedge has a visible length of about 2.8 m and is 80 cm wide at its broadest section. Very remarkably, it is sharply truncated at a depth of ~1.5 m (Fig. 4.6), the same depth where a significant change in cryostructure and sedimentary properties occurs. The ice wedge consists of vertically-foliated yellowish and sediment-rich ice in the outer section and very pure transparent ice with big non-elongated bubbles in its interior.

Comparable light mean values for $\delta^{18}O$ of around -29 ‰ and for δD of -232 ‰ have been measured for HI-IW-2 (Fig. 4.14) what is on average more than 8 ‰ lighter than HI-IW-1 and thus indicating strongly deviant conditions during its formation than present as well as during the formation of HI-IW-1. Only a minor isotopic and thus climatic trend within the ice wedge becomes obvious since values for $\delta^{18}O$ lie within a narrow range between -30.2 ‰ and -28.2 ‰ and between -224 ‰ and -243 ‰ for δD (Fig. 4.14), although the central section exhibits the lightest values of around -30 ‰ ($\delta^{18}O$) and -242 ‰ (δD), respectively. The mean d-excess (-0.3 ‰) is rather low and deviant from the GMWL.
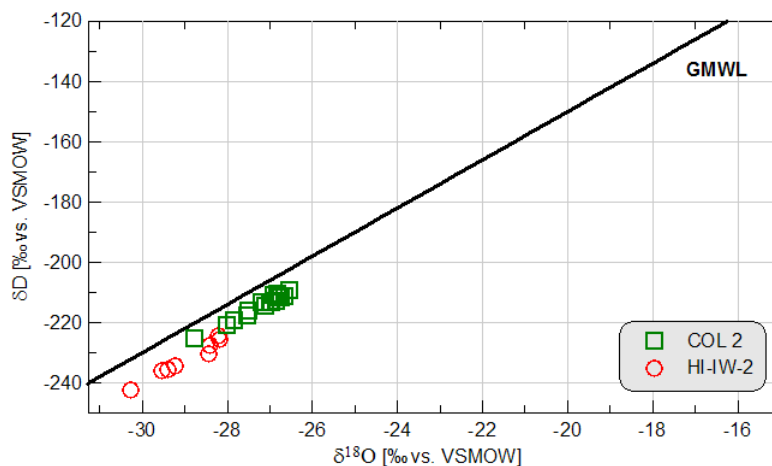
Fig. 4.14: δD-δ^{18}O diagram for COL 2 (texture ice) and HI-IW-2 (ice wedge ice).
COL 2 comprises texture ice from the three profiles as shown in Fig. 4.5. Note that both data sets plot below the GMWL.
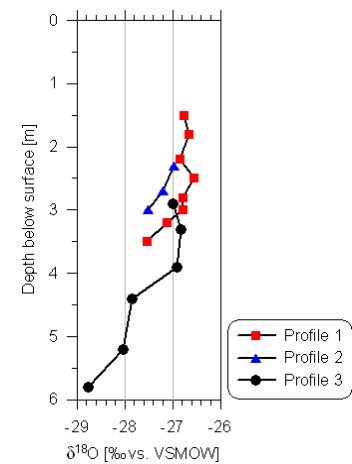
Fig. 4.15: δ^{18}O variations with depth regarding all three sub-profiles that have been sampled at the outcrop (Fig. 4.5). Generally, δ^{18}O becomes enriched upwards.

4.3 Thaw Slump D (TSD)

This huge retrogressive thaw slump (Fig. 2.16) holds a great variety of different sedimentary structures and cryostructures that have been affected by aggrading and degrading permafrost as well as by mass wasting processes. To unravel the landscape history of Herschel Island as accurate as possible, the prevailing ground ice types have been sampled in connection and with respect to the enclosing sedimentary sequences. Hence, four sediment profiles have been sampled and analysed in close vicinity to massive ground ice features. For a better understanding, sediment profiles No.2 & No.3 that have been sampled adjacent to ice wedges are considered first. Deposits of profiles No.1 & No.4 are of a most likely different origin as they are associated with massive ice bodies and are thus treated afterwards.

4.3.1 Sediments (TSD)

Profile 2 (TSD 2)

The second profile was sampled 1.2 m to the right of an adjacent ice wedge. The whole profile is characterised by the absence of CaCO$_3$ and values of pH below 7.0. From bottom to top, cryostructures shift at a depth of about 1.6 m b.s. from a reticulated structure with fine lenses towards a strongly cryoturbated pattern with large ice lenses. The active layer

was encountered at a depth of 0.5 m as a cryoturbated transitional horizon between vegetation cover and an upper very peaty ice-rich unit (Unit 2).

At the transition between Unit 1 & 2 at about 2 m b.s., pH drops significantly from 6.4 to 5.4 and generally decreases upwards to 4.6. Especially, the upper two metres (Unit 2) show strongly to moderately acidic conditions. Low values of pH coincide very well with high TOC contents between 9.9 and 17.5 % in the upper two metres, thus indicating acidification during the accumulation of peat as it was discovered here. TOC and pH seem to be more or less anti-correlated (Fig. 4.16).

The lowermost metre (Unit 1) has only minor TOC contents between 2 and 4 %.
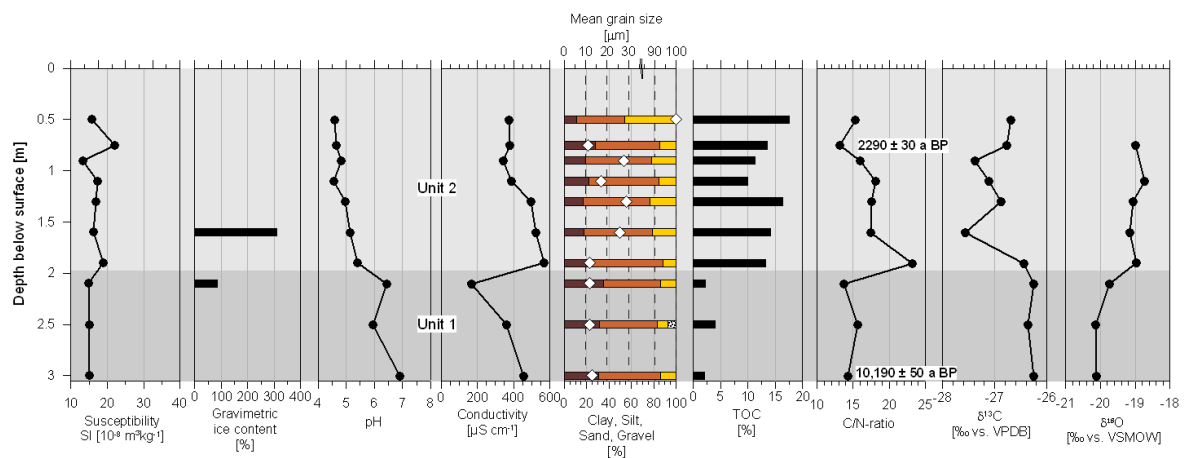
Fig. 4.16: Summary of physical, biogeochemical and stable isotope parameters for profile TSD 2. Age determinations are annotated next to the horizon they were sampled in and are recorded as uncalibrated ^{14}C years BP. Different grey scales mark distinctive units within the profile. Note that the axis of the mean grain size plot is broken and that their values are shown as rhombi within the grain size fraction pattern.

Determination of magnetic susceptibility yielded low values throughout the profile ranging from 13 to 23 SI without any trend. Also low values of electrical conductivity occur (168-566 μScm^{-1}), namely as they are almost one order of magnitude lower than measured at disturbed sites at Collinson Head. The only major shift appears in a depth of 2 m b.s., where conductivity rises from 170 to 570 μScm^{-1}. That is the same depth, where other parameters like pH, TOC, C/N-ratio and $\delta^{18}O$ shift significantly, too (Fig. 4.16). C/N-ratios vary between 13 and 23 with its maximum at about 2 m b.s. but do not show any trend. Although values of $\delta^{13}C$ are somewhat more variable than in other profiles studied, they appear in the same range between –26 and –28 ‰.

Regarding the grain size distribution (Fig. 4.17), it becomes obvious that the whole profile mainly consists of a diamicton with two major variations within the profile.

(1) The lowermost metre is composed of very poorly-sorted medium silty clay with a mean grain size of 12-13 μm as it is enriched in clay towards ca. 30-35 %. Single pebbles are present.

(2) Unit 2 consists of a very poorly sorted silty loam interspersed with pebbles in comparison to the uppermost horizon that is defined as a silty loamy sand with a mean grain size of 100 μm as it is more sandy than the lower part of the profile.

Age determination at the basis of the profile at 3.0 m b.s. yielded a ^{14}C-age of 10,190 ±50 a BP while dated peat at 0.75 m b.s. shows an age of 2290 ±30 a BP.

Fig. 4.17: Grain size distribution of profile TSD 2.
Left inset shows the very poorly sorted character of all horizons. The sediment triangle points out that the dominating silt owns variable contents of clay and sand.

Profile 3 (TSD 3)

A further profile was sampled to the left of an adjacent ice wedge that will be addressed in terms of ground ice analyses in chapter 4.3.2 and covers the interval between 1.8 and 3.2 m below surface. Within the profile at about 2 m b.s. there occurs a distinct discontinuity between a lower section that is dark grey, ice-rich and whose cryostructure is clearly cut at the unconformity (Fig. 4.18) and an upper not further differentiated sequence that is brownish grey and − in contrast − has a lens-like reticulated cryostructure.
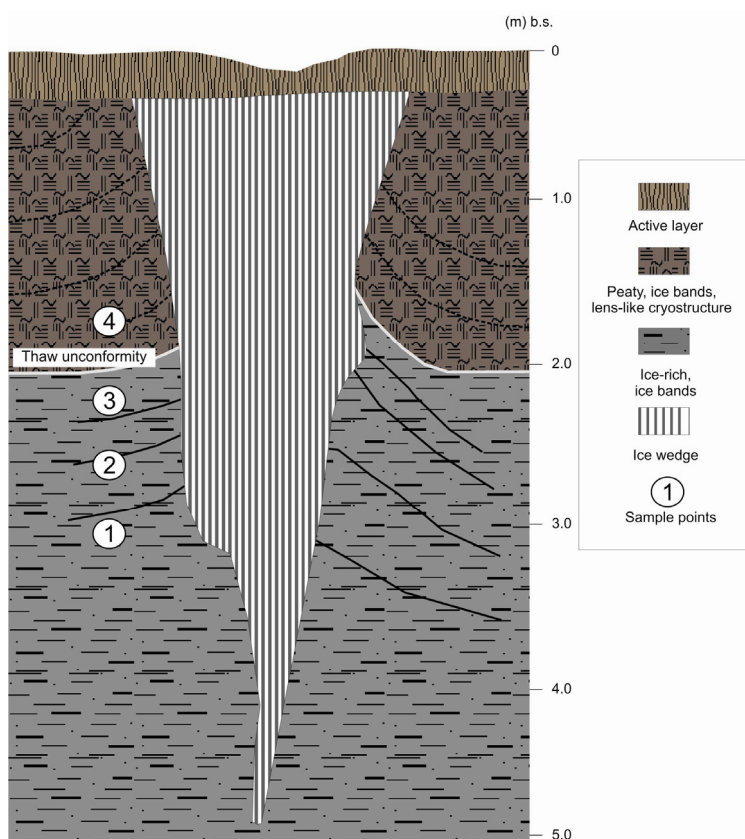
Fig. 4.18: Profile TSD 3. Numbers indicate the sample points. Solid white line marks the thaw unconformity. Ice wedge TSD-IW was sampled in terms of stable isotope geochemistry.

In general, all performed analyses show quite homogeneous properties (Fig. 4.19). In summary, TOC is present by about 1.2 % and C/N-ratios are stable at relatively low values (11-12). Determination of magnetic susceptibility yielded constant values of 23-24 SI and a peak in the uppermost horizon with 34 SI. Electrical conductivity values rise upwards from 1097 to 1353 μScm^{-1}, whereas values of pH decrease slightly but constantly in a neutral range from 7.2 to 6.9. Stable carbon isotopic ratios ($\delta^{13}C$) show minor variations at values around −26.0 ‰.
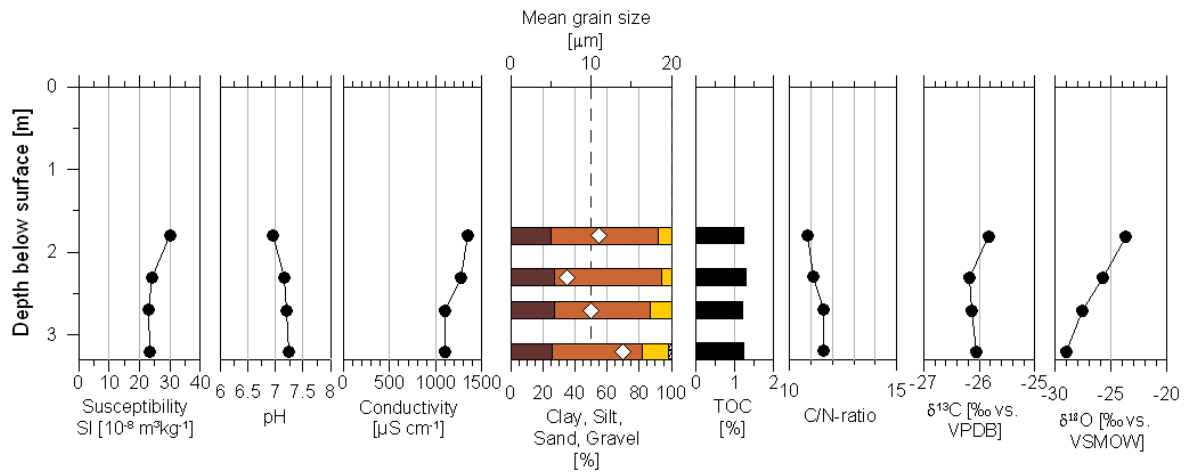
Fig. 4.19: Summary of physical, biogeochemical and stable isotope parameters for profile TSD 3.
Note that the mean grain size is plotted as rhombi within the grain size fraction pattern.

Also grain size distributions show only minor variations (Fig. 4.20).

Deposits of the lower part can be defined as a silty loam because of relatively higher sand and lower silt contents in comparison to the upper two horizons which are dominated by a very silty clay, though, all samples are very poorly sorted at a mean grain size between 7 and 14 μm. The occurrence of about 2 % of gravel in the lower horizon and single pebbles in the upper one leads to the classification as a diamicton. On the whole, physical and biogeochemical properties of this profile are very similar to those measured at *Profile 2* within the thaw slump at Collinson Head No.2 (see ch. 4.2).
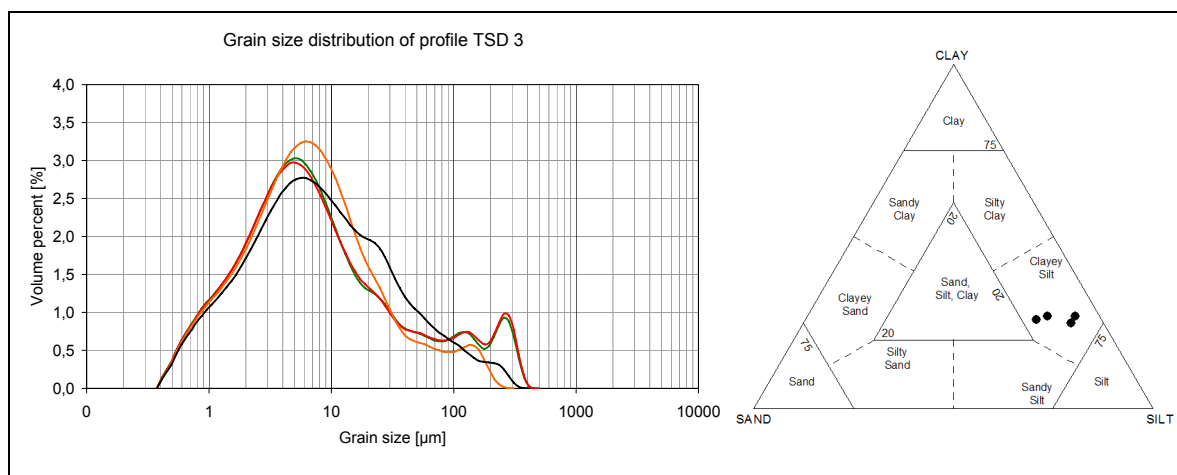
Fig. 4.20: Grain size distribution of profile TSD 3. Left inset shows the very poorly sorted and bimodal character of all horizons. The sediment triangle shows the silt dominance with clayey admixtures but with low variations throughout the profile.

Profile 1 (TSD 1)

The first profile represents an exception since it was not sampled in the typically vertical way but horizontally. Vertically-oriented ice-rich sediments occur immediately on the left hand side of an extremely deformed massive ice body (Fig. 4.28) that will be addressed as TSD-MI in chapter 4.3.2. The samples were taken at about 1.0 m b.s. out of the slump headwall with increasing distance − from 0.3 to 1.5 m − to the massive ice body (Fig. 4.28). In general, the profile is divided into three units (Fig. 4.21).

(1) The section with greatest distance to the massive ice body (Unit 3) has a coarse lens-like cryostructure and is not very ice-rich (<50 %). Sediments are greyish brown and have a low magnetic susceptibility (≤18 SI). $CaCO_3$ is present (c1-c2) but to a lower degree than the other units. The horizons located farther to the massive ice, contain well-rounded pebbles and cobbles up to 10 cm in diameter and are comparably rich in sand.

(2) The part right beside the massive ice (Unit 1) is very ice-rich with a gravimetric ice content of 146 %. It is bedded, holds more carbonate (c3) and slightly higher values of magnetic susceptibility (23 SI). Additionally, coarse granules (>2 mm) are absent.

(3) Between both greyish brown units, a black to dark grey and very massive horizon (Unit 2) with a thickness of 25 cm occurs. There, magnetic susceptibility is highest with 34 SI, a peak in electrical conductivity (3530 μScm^{-1}) is evident and the value of $\delta^{13}C$ is lightest, although all values range within −26.7 and −26.1 ‰. Though, the horizon appears very dark to almost black, the content of TOC remains low at about 1.5 %. Regarding grain size distribution the clay content is enhanced by about 6 to 10 %, although the whole profile generally consist of a diamicton that is dominated by a very poorly sorted silty loam (Fig. 4.22).
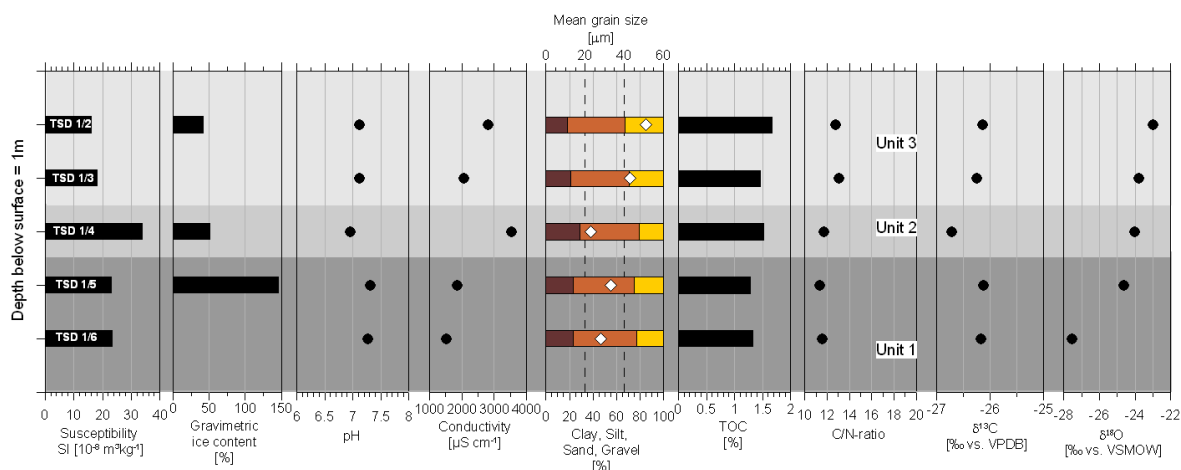
Fig. 4.21: Summary of physical, biogeochemical and stable isotope parameters for profile TSD 1.
Note that all horizons were sampled horizontally in a depth of ~1 m below surface. Different grey scales mark distinctive units within the profile. Note that the mean grain size is plotted as rhombi within the grain size fraction pattern.

Biogeochemical parameters such as TOC, C/N-ratio and δ^{13}C isotopic ratios show minor variations throughout the profile (Fig. 4.21). Organic carbon is present with 1.4 to 2.1 % by weight, leading to stable C/N-ratios of 11 to 13. Stable carbon isotope analyses yielded extremely constant values of about −26.4 ‰ to −26.1 ‰ thus proposing a quite stable source of organic remains.
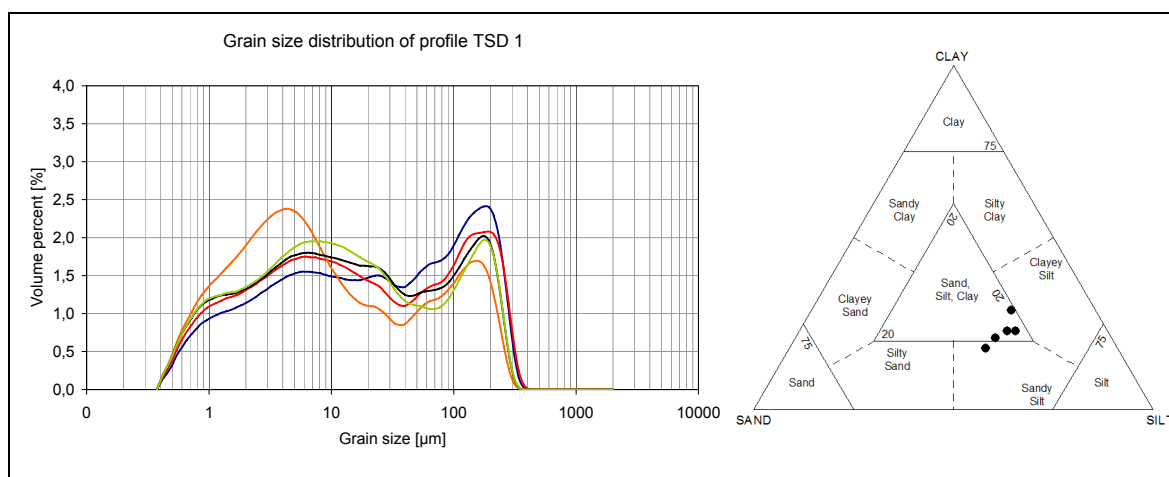
Fig. 4.22: Grain size distribution of profile TSD 1.
Left inset shows the very poorly sorted and silty to loamy character of all horizons. The sediment triangle points out the silty character with significant presence of all grain size fractions and a low variation throughout the profile.

Profile 4 (TSD-SP)

Sampling of *Profile 4* is directly associated with the detection of a massive ice body that likely represents a buried snow patch in a depth of 2.5 m below surface. The overburden obviously holds a recent active layer of 0.7 m although it seems to have thickened by 0.3 m

in modern times because of cut-effects. Sediments of the whole outcrop are generally brownish grey since they are rich in organics and possess a lens-like reticulated cryostructure. Patches of peat are intercalated at depths of 2.0 and 1.0 m b.s. leading to relatively high TOC contents between 5.8 and 17.3 % that increase upwards (Fig. 4.23). With lower depth, values of pH and electrical conductivity show contrasting trend directions insofar as pH decreases from a weakly to a moderately acidic reaction and conductivity rises on a quite low level from about 280 to 400 µScm^{-1}. Determination of C/N-ratios, magnetic susceptibility and δ^{13}C show constant values at about 15, 15 SI and −27 ‰, respectively (Fig. 4.23).
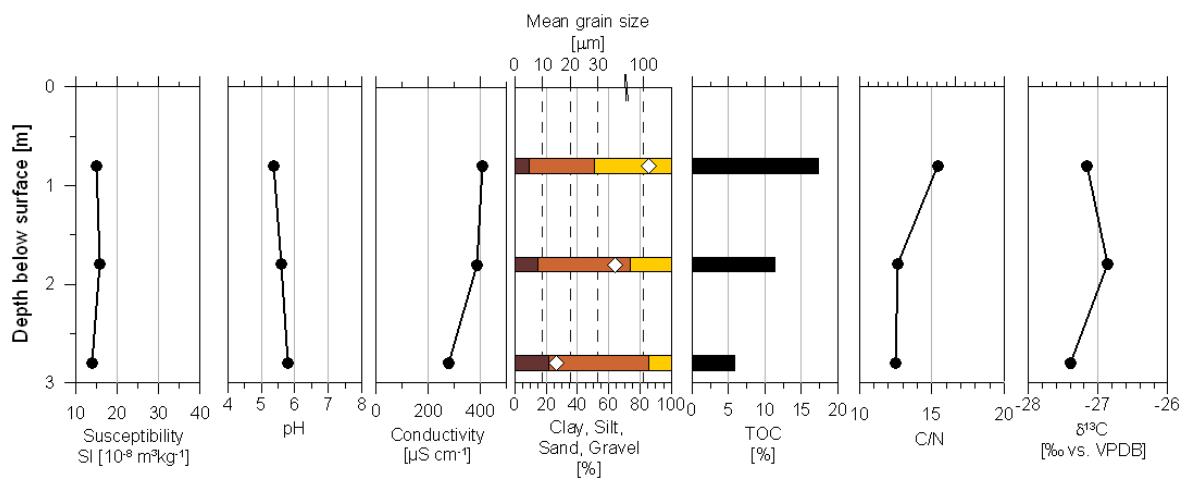
Fig. 4.23: Summary of physical, biogeochemical and stable isotope parameters for profile TSD-SP. Note that the mean grain size is plotted as rhombi within the grain size fraction pattern.

Grain size analyses show a strong coarsening trend from bottom to top, although single pebbles are ubiquitous. In spite of strongly variable contents of clay (9-22 %), silt (42-64 %) and sand (14-49 %), the silty character of the diamicton keeps prevalent (Fig. 4.24) except the uppermost part being more sandy. The mean grain size supports this view as it increases from 15 to 100 µm from bottom to top (Fig. 4.23).
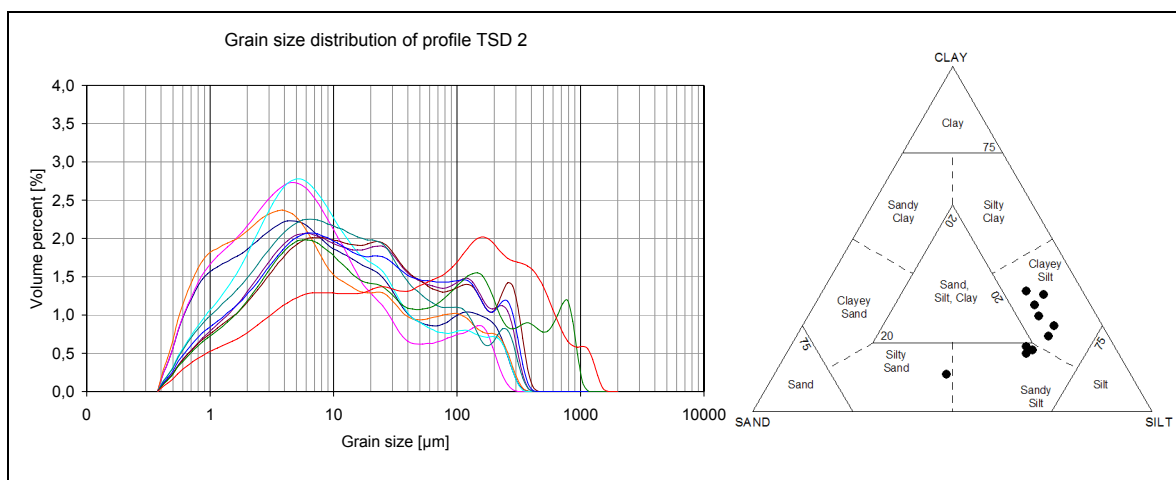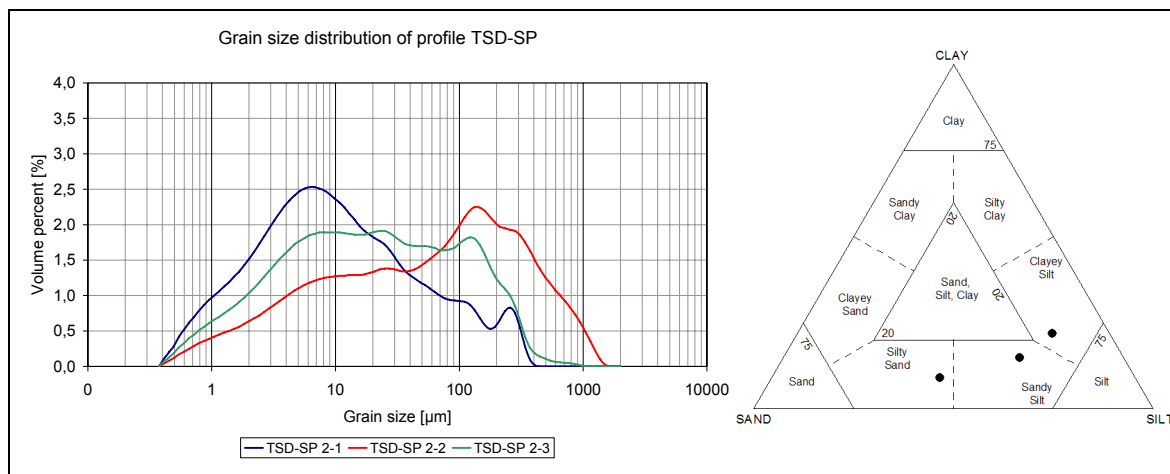
Fig. 4.24: Grain size distribution of profile TSD-SP.
Left inset shows the very poorly sorted character of all horizons. The sediment triangle points out the strong variation between the horizons.

Unfortunately, no age determination was performed at the base of the overburden so that an age of the ice body and its date of burial by mass wasting processes can not be estimated.

4.3.2 Ground ice (TSD)

Texture ice

The δD-$\delta^{18}O$ scatter diagram (Fig. 4.25) depicts the isotopic composition of texture ice throughout three profiles, also in comparison with an ice wedge that was sampled adjacent to *Profile 3*. Additionally, oxygen isotopic variations are plotted against depth (Fig. 4.26) for reasons mentioned in chapter 4.2.2.

At first, it becomes obvious that the isotopic composition of *Profile 1 & 3* lies within almost the same broad range for $\delta^{18}O$ (−29 ‰ to −23 ‰) and δD (−229 ‰ to −175 ‰); in contrast to *Profile 2*, which exhibits heavier values between −20.1 ‰ to −18.7 ‰ for $\delta^{18}O$ and −154 ‰ to −140 ‰ for δD in a very narrow span (Fig. 4.25). Second, figure 4.26 reveals that *Profile 2* becomes continuously enriched in $\delta^{18}O$ with decreasing depth and that *Profile 1* does as well with increasing proximity to the massive ice body; in contrast to *Profile 2* that shows only minor variations with depth, except a little step towards higher values at about 2 m below surface.
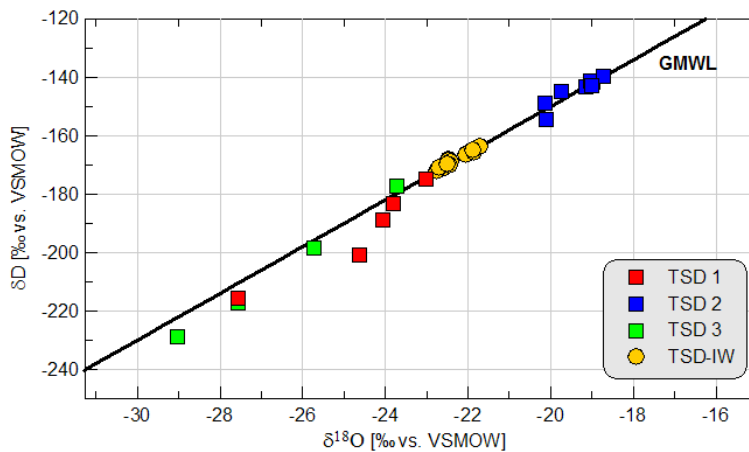
Fig. 4.25: δD-δ^{18}O diagram for TSD (texture ice) and TSD-IW (ice wedge ice).
The sub-profiles (TSD 1, TSD 2, TSD 3) are shown separately because of their broad range.
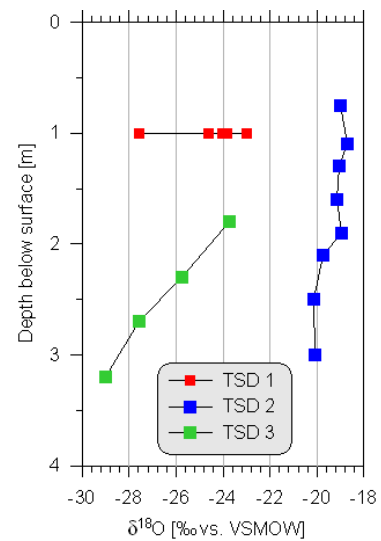
Fig. 4.26: δ^{18}O variations with depth regarding all three sub-profiles that have been sampled at the outcrop.
Note that TSD 1 was sampled at a constant depth of ~1 m below surface due to the vertical orientation of structures.

With a slope of 8.0 and a mean d-excess of 10.3 ‰, *Profile 2* fits the GMWL compared with the other ones that show slopes above 8.0 (*Profile 1*: 8.7, *Profile 3*: 9.9) and mean values of d-excess below 10.0 ‰ (*Profile 1*: 4.3 ‰, *Profile 3*: 6.8 ‰) thus indicating different temperature and hydrologic conditions during the formation of initial waters and/or texture ice.

Ice wedge ice

Adjacent to *Profile 3*, an ice wedge (*TSD-IW*), being ca. 4 m high and up to 1.8 m wide, penetrates through the cryostructural unconformity and is cut at the base of the modern active layer (Fig. 4.18). At a depth of ca. 2.0 m b.s. a widening of the ice wedge as a shoulder is established where sedimentary structures are curved upwards. This leads to the assumption that at least the upper two metres of the ice wedge grew syngenetically within an extensive polygonal system that is exposed throughout the slump headwall (Fig. 27).

Values for δ^{18}O and δD lie within a very narrow range between –22.8 ‰ and −21.7 ‰ and between −172 ‰ and −164 ‰ for δD, respectively (Fig. 4.25). Moreover, *TSD-IW* has a slope of 7.4 and ranges in d-excess between 9.4 ‰ and 11.9 ‰ with an average of 10.3 ‰, what is close to the GMWL.

Fig. 4.27: Syngenetic ice wedges that are exposed along the slump's headwall.

Hence, isotopic values for the ice wedge lie well above those measured for segregated ice within sediments, where the ice wedge grew in, although isotopic characteristics between texture ice and wedge ice become similar above the unconformity, not only in isotopic ratios but also in d-excess.

Snow patch ice

A massive ice body that is buried 2.5 m under land surface and presumably made of diagenetic altered snow was sampled in connection with sediment *Profile 4* (*TSD-SP*). The snow patch (*TSD-SPI-2*) reaches 0.5 m in thickness and has distinct margins to the underlying and overburden without any melting margin. The ice is milky grey and the dispersed bubbles have no orientation.

Another ice body that is supposed to be a relic and buried snow patch (*TSD-SPI-1*) at ~5 m b.s. was also sampled to determine its stable isotope composition. These two ice bodies of rather similar appearance exhibit minor differences regarding their isotopic composition but a somewhat greater variation regarding their slope and d-excess. Mean values for TSD-SPI-2 are −19.1 ‰ for $\delta^{18}O$ and −141 ‰ for δD compared to −21.1 ‰ and 159 ‰ with respect to *TSD-SPI-1* (Fig. 4.28). With a slope of 7.6 and a mean d-excess of 9.9 ‰, *TSD-SPI-1* lies almost exactly on the GMWL whereas *TSD-SPI-2* holds values for slope and d-excess of 5.5 and 12.2 ‰, respectively, which differ slightly from the GMWL.
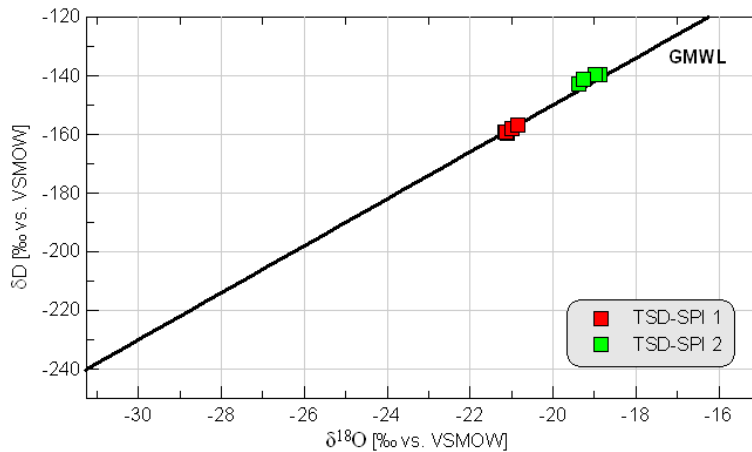
Fig. 4.28: δD-δ¹⁸O diagram for buried snow patches TSD-SPI-1 and TSD-SPI-2.

Massive Ice of unknown origin

A very curious body of massive ice was encountered in the headwall of the retrogressive thaw slump on the right of *Profile 1*. It is generally composed of clear to milky white ice with a strongly variable content of sediment bands that are folded together with the ice structures leading to anticlinal and synclinal as well as vertically and horizontally bedded structures within the ice body (Fig 4.29).
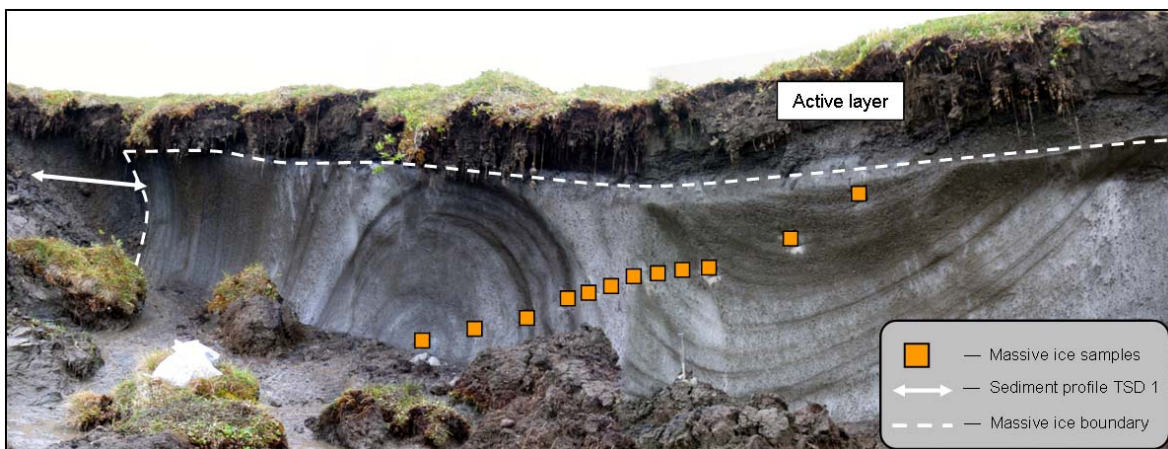
Fig. 4.29: Massive ice body of unknown origin (TSD-MI).
The surface of the ice body is truncated by the basis of the modern active layer. The internal structure of the ice body is strongly deformed.

The top is discordantly truncated, either by erosion due to slope processes or by the modern active layer in consequence of seasonal thaw and freeze. By contrast, the basis of the massive ice could not be observed as the slump's headwall was exposed only the upper ~3 m and the slump floor was covered by thaw flow deposits. Regarding cryolithology, it becomes obvious that the ice characteristics change significantly over short distances as though originally horizontally layered cryostructures have been deformed by thrusting and

folding. This assumption becomes reinforced as sediment inclusions and gas bubbles are elongated and oriented in the same direction and inclination of folding. Samples for stable isotope analyses were taken in diagonal direction from bottom to top of the exposed massive ice body (Fig. 4.29).
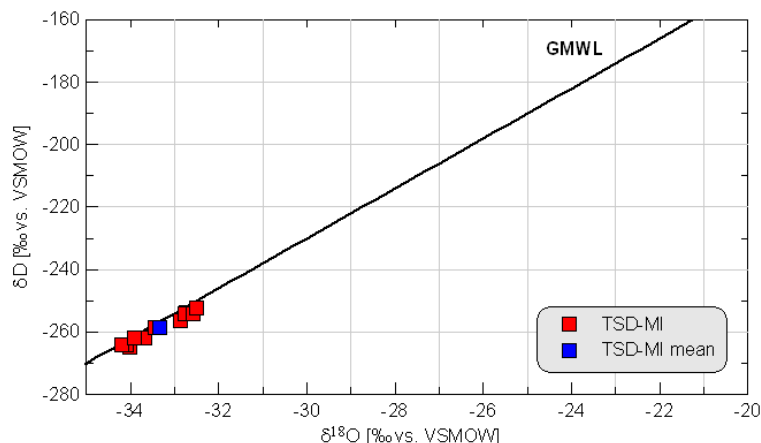
Fig. 4.30: Isotopic composition of the massive icy body (TSD-MI) of unknown origin.
Note the strongly depleted isotopic composition.

The isotopic composition differs strongly from all ice types analysed before since $\delta^{18}O$ and δD show strongly depleted mean values of -33.3 ‰ and -259 ‰ within a narrow range from -34.2 to -32.5 ‰ and -265 to -252 ‰, respectively (Fig. 4.30). With a mean d-excess of 8.0 ‰ and a slope of 7.2, the massive ice body lies only little below the GMWL, similar to ice wedges and some snow patches that have been recovered and that are normally fed by winter precipitation. Isotopic values are very deviant from those being measured at texture ice of *Profile 1* (Fig. 4.26) indicating completely different conditions during the formation of both ice types.

4.4 Herschel Island−Glacier Ice (HI-GI)

This large body of massive ice (Fig. 4.31) was exposed by fluvial erosion due to meltwater incision and thermoerosion in connection with mass wasting processes in consequence of disturbances in vegetation cover.

At the sample location the ice body is ~7 to 8 m high, discordantly overlain by several metres of sediments and with almost no gradual transition (i.e. no sediment incorporation into melted margins) towards the overburden. Obviously, the ice body is not homogeneous but consists of different realms with distinctive cryolithological characteristics (Fig. 4.32).

Fig. 4.31: Outcrop Herschel Island−Glacier Ice (HI-GI).
The ice body is exposed in an erosional valley along the west-facing coast of Herschel Island and is composed of parts with different habit. Inset A exhibits the sample location and a sampled transect of very pure ice. Inset B shows large striated boulders in direct neighbourhood to the ice.

(1) The first part that makes up the largest portion covers a very clear ice with few gas inclusions, visible crystal boundaries, a visible crystal size of 0.6 to 0.8 mm and without any sediment.

(2) A second part is of the same characteristics but has some sediment inclusions as fine sediment bands.

(3) The third part is of milky white ice with seemingly high gas content in contrast to

(4) another kind of ice being of bluish cloudy appearance.

On one side the ice is overlain by ~6 m of dark grey clays, whereas the most widespread cover is made up of brownish-grey deposits with a significant content of organic macro-remains like roots and peaty inclusions. Another very striking feature is the occurrence of large striated boulders of more than 1 m in diameter (Fig. 4. 31 B) at the mouth of a narrow erosional valley in approximately the same height the ice body is located.

Every single portion of the ice body that could be differentiated was sampled in terms of stable isotope analyses. Although one continuous ice body was encountered, isotopic values vary greatly by nearly 16 ‰ ($\delta^{18}O$) within a range from −36.7 to −21.0 ‰ for $\delta^{18}O$ and from −276 to −169 ‰ for δD (Fig. 4.33). Values of d-excess also range widely between −3.9 to 20.0 ‰, thus indicating extremely deviant conditions in terms of water source, vapour source, winter temperatures and secondary phase changes that will be discussed later on.
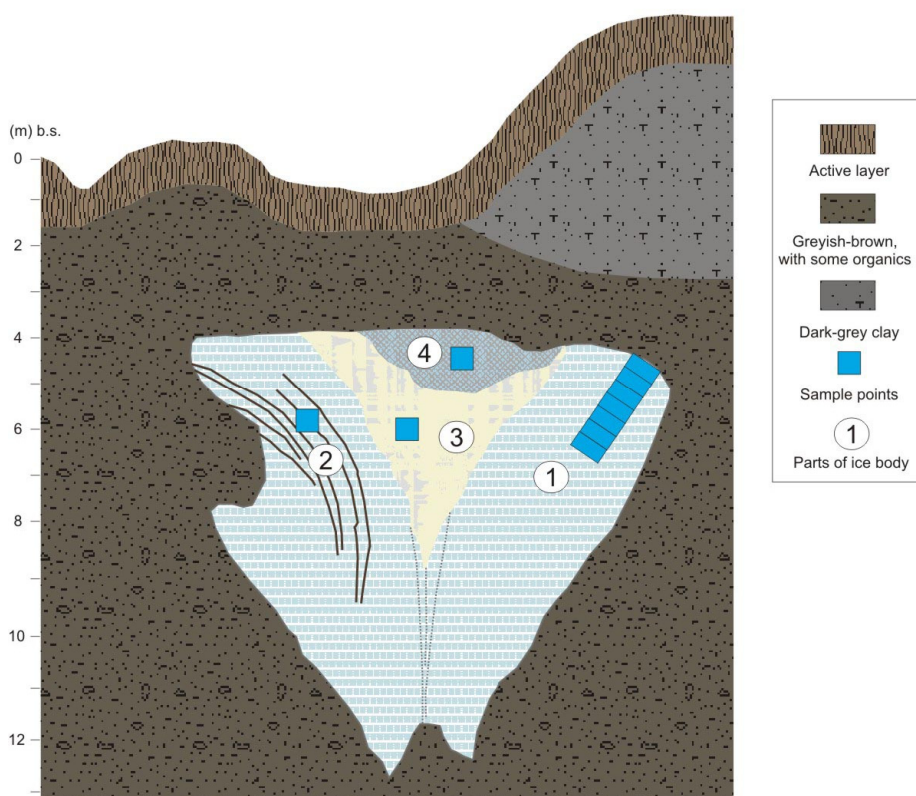
Fig. 4.32: Massive ice body (HI-GI) of unknown but probably
glacial origin.
Note that the ice body consists of several parts.

Part (1) was sampled as a ~80 cm transect from the interior to the outer edge of the ice body (Fig. 4.32). Six adjoining blocks were subsampled into thirty-three slices and measured subsequently. It becomes obvious that there exists a strong gradient from heavier values (−21.0 ‰, $\delta^{18}O$) towards lighter ones (−29.9 ‰, $\delta^{18}O$) from the outside inwards (Fig. 4.33). This gradient is strongest within the first 10 to 15 cm; from −21.0 to −26 ‰, where the ice is in contact with adjacent sediments. D-excess values between −3.9 and 3.5 ‰, Part (1) lie well below the GMWL.

Part (2) fits isotopically to the interior of Part (1) with a mean value for $\delta^{18}O$ of −28.3 ‰ (Fig. 4.33) and a d-excess of −1.2 ‰.

With −36.8 ‰ on average for $\delta^{18}O$ and −274.5 ‰ for δD (Fig. 4.33), the milky white ice of Part (3) exhibits the lowest isotopic values that have been measured on ground ice on Herschel Island during this study. A mean d-excess of 19.5 ‰ makes this sample series unique and absolutely diverse to all other parts of this outcrop.

Finally, the bluish cloudy ice of Part (4) at the top of the ice body yielded values of −30.5 ‰ for $\delta^{18}O$ and −239 ‰ for δD with a mean d-excess of 5.1 ‰ that may fit to the lower end of Part (1) (see Fig. 4.33).
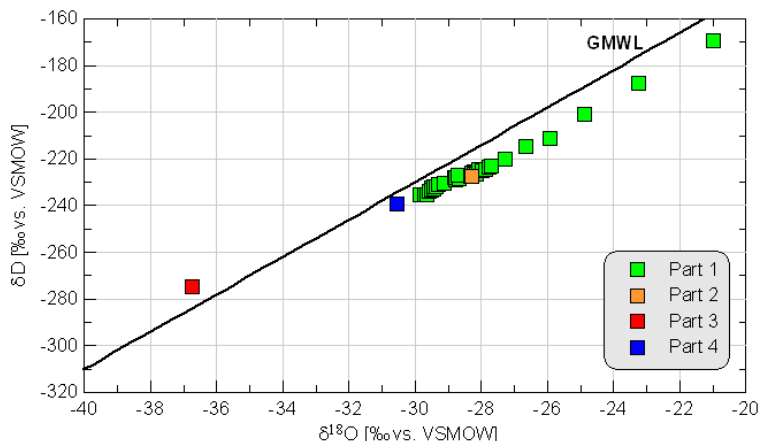
Fig. 4.33: Isotopic composition of the single parts of the massive ice body (HI-GI) of unknown origin. Note the strongly depleted isotopic composition of Part 3 and the gradient from low to higher values of Part 1.

4.5 Komakuk Beach (KOM)

4.5.1 Sediments (KOM)

The outcrop at Komakuk Beach was sampled with respect to its exceptional position as a most likely unglaciated site on the Yukon Coastal Plain, at least during Wisconsin glacial times. An obviously undisturbed and relatively dry polygonal surface (high-centred polygons) (Fig. 2.18) with a thick peat cover overlies the mineral horizons. The active layer was encountered at low depths between 30 and 40 cm since the thick peat cover insulates the permafrost very well.

In general, the continuous profile being 4.3 m in height has to be divided into two parts that differ in almost every parameter while the upper section might be subdivided twice, again. The lowermost section (X1) from 4.3 to 2.7 m b.s. has a homogeneous lens-like reticulated cryostructure and appears quite colourful with greenish, yellowish and brown horizons, and owns intercalated humic bands as well as macroscopic organic remains. Furthermore, it possesses a very significant content of carbonate (c3) as the field test performed with HCl (10 %) indicates. Relatively high values of pH (7.0 to 7.8) support this view. In contrast, organic carbon is only present to a low to very low degree, ranging from 0.5 to 4.6 % (Fig. 4.34). Also C/N-ratios remain low within a range from 8 to 12.

Measurements of magnetic susceptibility yielded low values of around 16 SI, although the lowermost horizons show values of ~25 SI. In contrast to most outcrops on Herschel Island, highest gravimetric ice contents occur in the upper part (173-536 %), whereas the lower part has ice contents no greater than 65 % (Fig. 4.34). Measurements of electrical conductivity in the lower section yielded somewhat inconsistent values as exploratory measurements in the field indicated very high values above 6000 μScm^{-1}, in contrast to some of the laboratory values that range widely between 700 and 3200 μScm^{-1}. Nevertheless, most of these values are at least twice as high as those of the upper part. Except a few small irregularities, δ^{13}C shows a slight but steady depletion from −25.6 ‰ at the profile's basis to almost −29 ‰ at the surface. With respect to grain size distribution the section *X1* shows a dominance of silt (by ~60-70 %), especially coarse silt, leading to a mean grain size between 20 and 46 μm. Sand is present to 13-30 % with a strong dominance of fine and very fine sand (63-200 μm). Clay-sized material occurs by 9-18 % and single cobbles are present, however they disappear in horizons at a depth of 3.8 and 3.1 m b.s. where organic patches have been encountered.
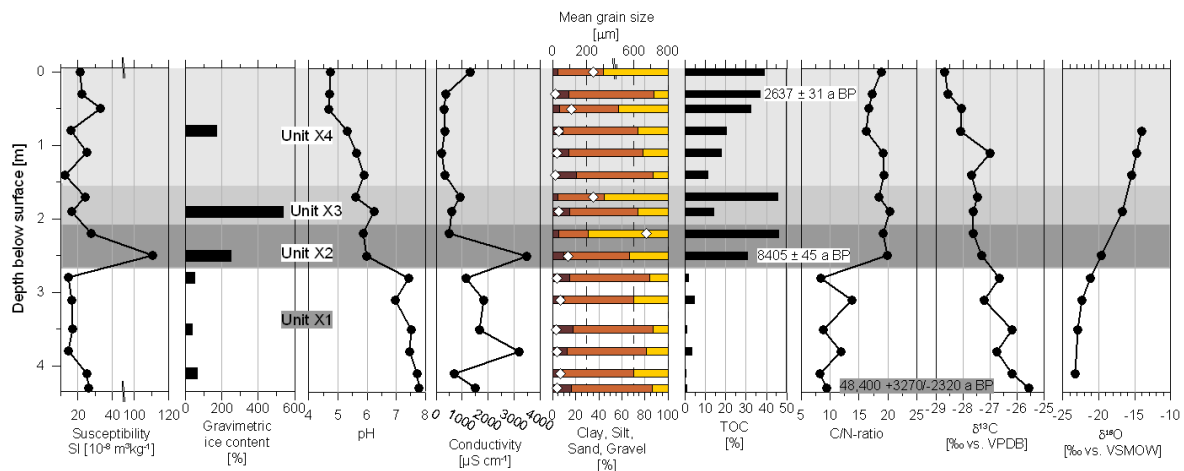
Fig. 4.34: Summary of selected physical, biogeochemical and stable isotope parameters for profile KOM. Age determinations are annotated next to the horizon they were sampled in and are recorded as uncalibrated ^{14}C years BP. Different grey scales mark distinctive units within the profile. Note that the axis of the mean grain size plot is broken and that their values are shown as rhombi within the grain size fraction pattern. X-axis of magnetic susceptibility is broken, too.

The section above unit *X1* differs in almost every parameter. However, the most striking difference is best illustrated by the rise in the content of organic carbon from on average less than 2 % to more than 10 % (Max = 45.8 %, Fig. 4.34). The deviation of TOC within the upper section is also the decisive criterion for a sub-differentiation into three further units (X2, X3, X4). In general, all three upper units are free of CaCO$_3$. They almost

entirely show a low pH below 6.0 and depleted values of $\delta^{13}C$ below -27 ‰, and exhibit highest values of TOC (11-46 %) having measured. C/N-ratios remain quite stable at values between 17 and 20.

Within Unit X2, the content of TOC rises up to 31 and 46 %, respectively, while pH drops significantly. Very interesting sedimentary analytical values have been obtained at the boundary between units X1 & X2 at ~2.5 m below surface. At this certain depth, TOC rises from 2 to 31 %, C/N-ratios advance likewise from 8 to 20, pH lowers spontaneously from very weakly alkaline (~7.5) to a weakly acidic reaction (6.0) and electrical conductivity exhibits an isolated peak at ~3500 μScm^{-1} (Fig. 4.34). Cryostructures change abruptly from a lens-like reticulated pattern with less ice (50 %) to a banded structure with a high ice content (~250 %). And most notably, determination of magnetic susceptibility that normally yielded values between 14 and 33 SI throughout the profile shows an extreme outlier (111 SI) at this transition (Fig. 4.34). With the help of a binocular, a strongly magnetic black crust was observed that coats organic remains.

The base of the overlying Unit X3 between 2.0 and 1.5 m b.s. is characterised by a very high ice content (536 %), a minor increase in electrical conductivity and a drop in TOC from 46 % in the underlying (X2) down to 14 % (Fig. 4.34). Values of pH decrease continuously what is probably due to humic acids originating from high peat contents. Upwards, electrical conductivity advances to more than 900 μScm^{-1} as well as TOC content rises again up to 46 %.

At the transition from X3 to Unit X4 TOC drops to ~11 % as well as conductivity which is reduced from 1000 to 400 μScm^{-1} (Fig. 4.34). The uppermost unit covers the profile's upper ~1.5 m and shows a banded cryostructure below the active layer. The content of TOC increases continuously up to 39 % at the surface in same way as the value of pH decreases from 5.9 to 4.7. Measurements of electrical conductivity reveal quite low values (200-390 μScm^{-1}), except the surface, which is enriched to 1300 μScm^{-1}.

Radiocarbon dated material at the boundary between Unit X1 and X2 exhibit a ^{14}C-age of 8405 ±45 a BP. Further age determinations have been performed at the base of the profile at a depth of 4.3 m b.s. and on peat deposits at 0.3 m b.s. yielding ages of 48,400 +3270/-2320 a BP and 2637 ±31 a BP, respectively.
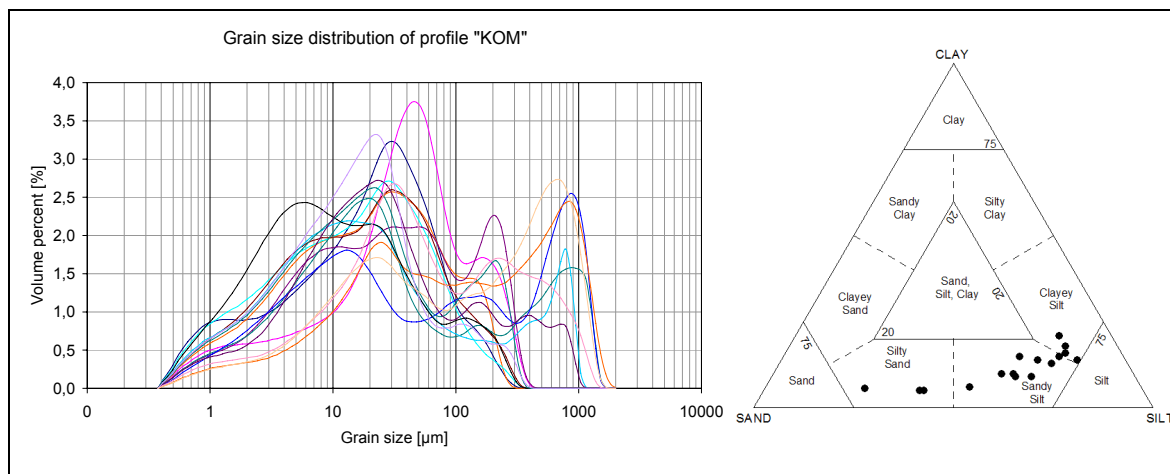
Fig. 4.35: Grain size distribution of profile KOM.
Left inset shows the very poorly sorted and strongly variable character of all horizons. The sediment triangle exhibits a silty dominance for most of the samples but an enrichment in sand-sized material for some samples.

Discussing grain size parameters of a very organic-rich unit is little ambiguous and could lead to misunderstandings since six of ten horizons within the organic-rich units (X1, X2, X3) hold more organic components as they consist of mineral material to be analysed. According to Scheffer & Schachtschabel (2002) and Meyers & Lallier-Verges (1999), the total amount of organic matter is approximately twice the content of TOC. This leads to an amount of organic matter between ~22 and 91 %. Thus, grain size parameters should not be overestimated since mineral grains only make up the minor amount of the bulk sample. Nonetheless, the general trend that all units are dominated by fine-grained silty deposits (Fig. 4.35) remains upright, although those horizons showing great contents of TOC seem to be dominated by sand-sized material. However, this picture is most likely biased as the organic-free samples − after treatment with H_2O_2 − have been strongly affected by the build-up of aggregates that could not be completely resolved prior to laser-sizing and would lead to an overestimation of the sand content. Additionally, it has to be noticed that coarse granules >2 mm are completely absent within this section.

4.5.2 Ground ice (KOM)

The δD-$\delta^{18}O$ scatter diagram (Fig. 4.36) shows the isotopic composition of texture ice throughout the profile, also in comparison to a little distant ice wedge that will be addressed in the course of this chapter. Moreover, variations in $\delta^{18}O$ and d-excess are plotted against depth (Fig. 4.37). Figure 4.37 shows a strong continuous enrichment of

heavy isotopes with decreasing depth. Values of $\delta^{18}O$ vary between -23.3 ‰ near the basis of the profile and -14.0 ‰ at 0.8 m b.s., hence showing values that are enriched by at least 3 ‰ in comparison to Herschel Island profiles, especially in the upper section of the profile. In contrast to most of the other sediment profiles analysed on Herschel Island, the wide range in d-excess is conspicuous, which strongly decreases upwards from ca. 6 ‰ at the same depth, where the organic-rich section meets the mineralic one to values of around -8 ‰.
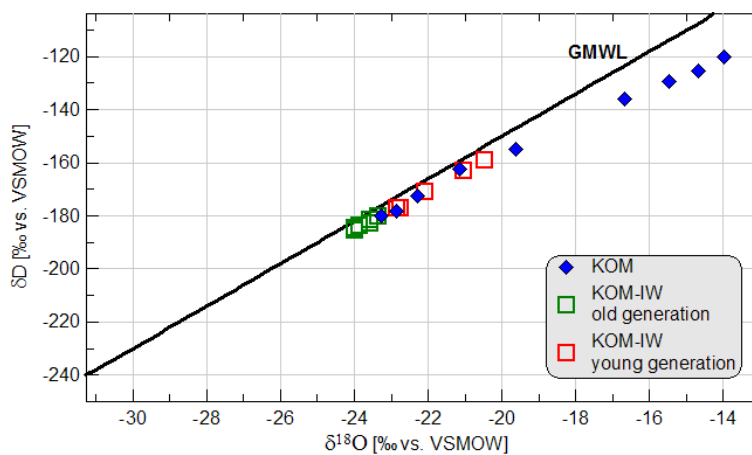
Fig. 4.36: δD-$\delta^{18}O$ diagram for texture ice (KOM) and ice wedge ice of different generations (KOM-IW).
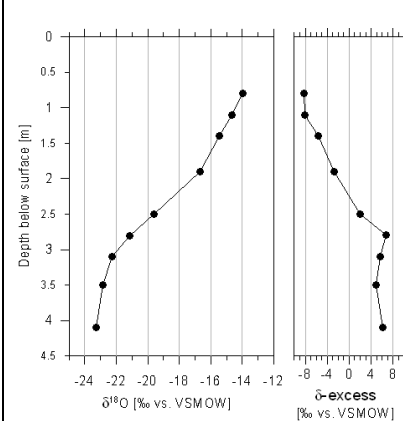
Fig. 4.37: $\delta^{18}O$ and d-excess variations with depth. Obviously, ^{18}O becomes enriched upwards in contrast to d-excess that is depleted.

One representative syngenetic ice wedge (KOM-IW) that consists of two generations was sampled in a horizontal transect, and two blocks were taken to cover the younger and the older wedge generation in particular (Fig. 4.38).
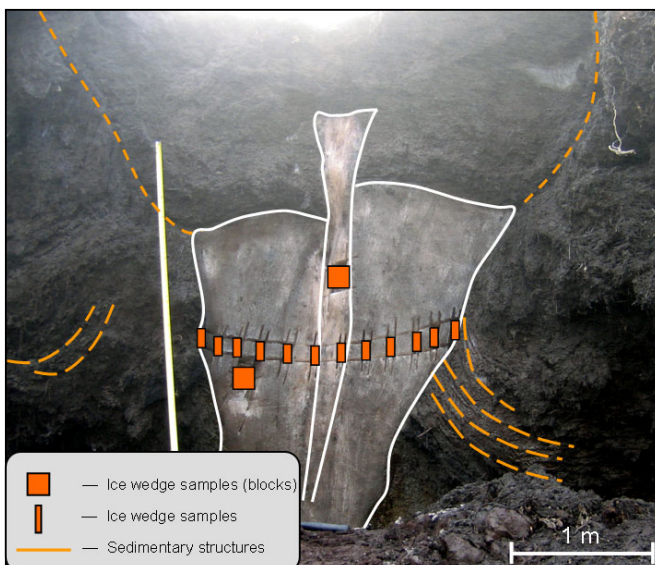
Fig. 4.38: Ice wedge (KOM-IW) that consists of two generations.

The older ice wedge is about 1.5 m at its broadest and is cuts at approximately 1.0 m b.s., whereas the upper and younger ice wedge is up to 25 cm wide and cuts with the base of the modern active layer (Fig. 4.38). Generally, the ice wedges are broader within the peat but penetrate into the clastic deposits as well, where they do not seem to be syngenetic. Differences in their stable isotope composition allow an analytical differentiation between both ice wedge generations. The older wedge is characterised by mean values of −23.7 ‰ for $\delta^{18}O$ and −183 ‰ for δD, whereas the younger ice wedge exhibits slightly enriched values (−21.8 ‰, −183 ‰) within a wider range (Fig. 4.36). Slopes are very similar (7.4 and 7.8) and close to the GMWL, though d-excess of the younger wedge (5.6 ‰) is little lower than that of the older wedge (7.1 ‰), both lying below the GMWL.

4.6 Recent ice and waters

To draw conclusions in terms of paleotemperatures, paleohydrology and probably about the atmospheric circulation of pre-recent times deduced from stable isotope ground ice characteristics, one has to consider recent conditions and their short-term variability. That's why several and most likely recent snow patches, ice veins as well as surface waters from lakes and ponds and rain waters deriving from different precipitation events have been sampled and measured. On the whole, recent material comprises three snow patches, two ice veins, four rainwater samples and eight surface waters. All samples were taken on Herschel Island, except one snow patch that was sampled at Komakuk Beach.

The δD-$\delta^{18}O$ scatter diagram (Fig. 4.39) shows that there are three isotopically similar groups within the wide scatter of all samples that range from −28.4 to −12.3 ‰ regarding $\delta^{18}O$ (−112 to −218 ‰ for δD). As assumed, snow patches that are fed by isotopically relatively depleted winter precipitation constitute the first group as they yield minimal $\delta^{18}O$ values between −28.4 and −26.6 ‰, and a d-excess between 5.7 and 10.5 ‰. However, one snow patch is isotopically enriched up to −23 ‰ and groups together with a recent ice vein (−22.2 ‰) and one summer precipitation event (−22.7 ‰) (Fig. 4.39). The third group comprises mainly surface and rain waters as well as a single ice vein that are significantly enriched in heavy isotopes (Fig. 4.39), so that values for $\delta^{18}O$ range from −22.7 to −12.3 ‰.
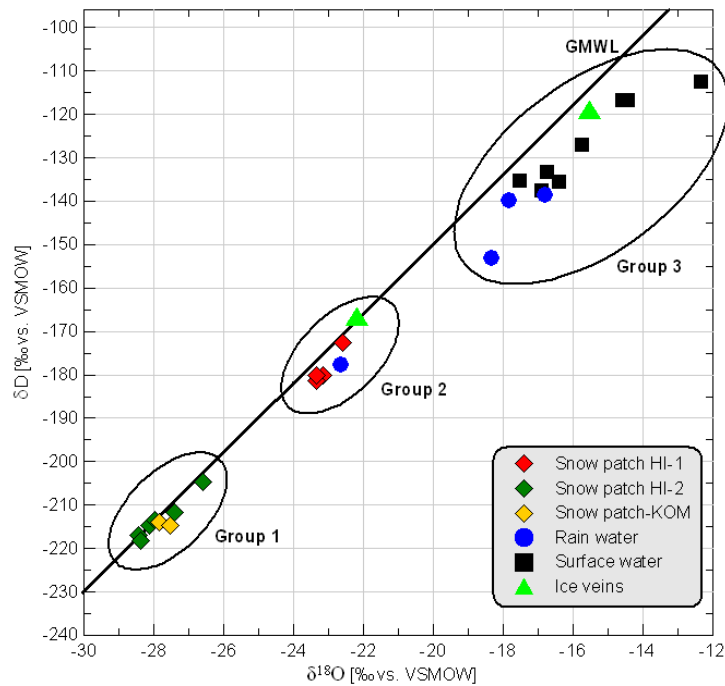
Fig. 4.39: δD-δ¹⁸O scatter diagram of recent ice and waters.
Three groups of similar isotopic characteristic are established.

Moreover, they show low values of d-excess between −13.7 and 3.8 ‰ that appear significantly below the GMWL. Surface waters exhibit most enriched isotopic values and lowest d-excess since waters in evaporative systems such as lakes or ponds are relatively enriched in heavy isotopes (GAT, 1996) and hold smaller d-excess values (GAT, 1995; BREZGUNOV et al., 2001).

5 DISCUSSION

This chapter is divided into three parts. The first one deals with the stratigraphic characteristics of the studied sediment sequences and correlates as well as it differentiates between the distinct sections. The second part examines the nature and origin of ground ice by cryostratigraphic and isotopic means in order to get information about the different processes related to permafrost aggradation and degradation history since deglaciation as well as to make assumptions about paleotemperatures during ground ice formation. And finally, a synthesis of ground ice and sedimentary characteristics will lead to a reconstruction of landscape and paleoenvironmental evolution on Herschel Island and in part at Komakuk Beach.

5.1 Stratigraphic characteristics & facies changes

Variations in the different physical and biogeochemical parameters indicate that facies changes took place in the study area during a period of time that is not yet defined exactly but goes back to at least the Late Wisconsin glacial interval. This in turn gives strong indications for environmental conditions having changed over time.

Herschel Island exhibits a very heterogenic landscape in terms of its geomorphology, which indeed has a glacial origin but that was and still is affected by numerous driving forces to alter its habit. This allows to set different stratigraphic layers within deposits of different facies. Unfortunately, the lack of good marker beds that can be correlated from site to site on Herschel Island (RAMPTON, 1982) makes it very difficult to establish a continuous stratigraphy for the island. Nevertheless, there is evidence for changing depositional environments through time although their spatial extent sometimes remained unknown during this study, although previously published data by Bouchard (1974) and de Krom (1990) give valuable additions regarding sediment analyses.

Glacially-deformed marine deposits

According to Mackay (1959), an important part of Herschel Island sediments consists of marine deposits deriving from Ptarmigan Bay (Herschel Basin) as they have been ploughed and pushed up by glacial activity to set a terminal moraine with a maximum elevation of more than 180 m above sea level. As described in chapter 4.2.1, unbedded dark grey clayey deposits without any clasts have been recovered at a relatively low position at the outlet of a retrogressive thaw slump at Collinson Head. These clayey silts are supposed to represent a deposit within a full-marine near-shore environment on the shelf since it is dominated by clay (38 %) and silt (45 %) but still holds a significant amount of fine sandy material (17 %). Moreover, it has a significant carbonate content leading to a value of pH near 8. The abundance of shells and shell fragments in the unstratified clayey silts is evidence for a marine environment, too.

An electrical conductivity of more than 5500 μScm^{-1} suggests an enriched content of total dissolved solids compared to sediments of other facies with values generally lower than 3000 μScm^{-1}. Organic matter is only present to a minor degree (~1 %). In Figure 5.1, the carbon stable isotopic ratios are plotted against C/N-ratios in order to get information about the organic carbon source. Carbon isotopic ratios are useful to distinguish between marine and continental plant sources of organic matter and to identify organic carbon from different types of land plants (MEYERS, 1994). C/N-ratios allow to distinguish between algal and land-plant origins of sedimentary organic matter (MEYERS, 1997). Thus, it becomes obvious that the organic carbon within the sediments treated here derives from an aquatic source and implies lacustrine algae being potentially responsible, although Rau et al. (1989) have shown that marine algae living in cold polar sea waters might have $\delta^{13}C$ values as low as −28 ‰, which is in the range of lacustrine algae. Therefore, with a narrow C/N-ratio of 9 and −26.3 ‰ for $\delta^{13}C$, a marine origin of organic matter is favoured in this case. With respect to the classification made by Bouchard (1974), this unit belongs to the "marine preglacial" deposits, although these sediments are of glacial origin by definition since they have been relocated by glacial action.
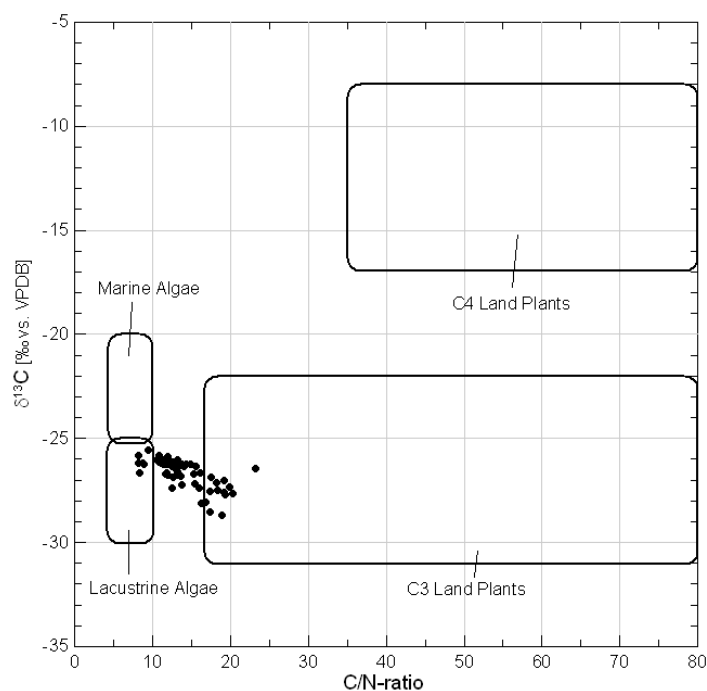
Fig. 5.1: Elemental (atomic C/N-ratio) and isotopic (δ^{13}C) identifiers of bulk organic matter produced by marine algae, lacustrine algae, C3 land plants, and C4 land plants (according to MEYERS, 1994 and MEYERS & LALLIER-VERGÈS, 1999, altered).
Note that all samples are included in this diagram.

Pebbly diamicton

Within the same slump and directly above the glacially-deformed marine unit, a greyish-brown pebbly diamicton occurred with abundant well-rounded pebbles and cobbles of 1-10 cm in diameter as well as few shell fragments. Its fine matrix consists of a sandy loam with quite equal proportions of clay (24 %), silt (36 %) and sand (39 %) and a mean grain size of 69 μm (median: 23 μm) (Figs. 4.12, 4.13). This unit is enriched in sand by at least 13 % compared to other units within the slump, which contain less clasts, thus making the pebbly diamicton clearly distinguishable from other units.

However, several physical and biogeochemical parameters are very similar to the underlying unit. So, pH is still high at about 8, the content of TOC remains low at 0.6 % and carbonate is still present (c3). A similar narrow C/N-ratio of 8 and −25.8 ‰ for δ^{13}C suggest the same marine algal source of organic carbon as the sediments underneath. This is affirmed by the presence of many clasts that should be largely absent in a lacustrine environment. A strong advocacy for a marine origin before glacial redeposition is given by the highest conductivity value (11,500 μScm^{-1}) of all stratigraphic units. Consequently, a marine littoral near-shore environment seems most likely for this unit before it experienced glacial reworking, although sediment and stratigraphic characteristics are inconsistent with the "mixed sediment" unit described by Bouchard (1974) that should have developed

within a similar near-shore environment. It seems most likely that Bouchard's mixed sediment unit, which is supposed to consist mainly of sands, was not recovered in any outcrop since it is believed to underlie marine sediments with a thickness between 1.2 and 11.2 metres.

Main diamicton

Within the retrogressive thaw slumps at Collinson Head No.2 (see ch. 2.4.1.1 & 4.2) and Thaw slump D (see ch. 2.4.1.2 & 4.3) a distinct discontinuity between 1.5 and 2.0 m b.s. was observed, which is overwhelmingly interpreted as a Holocene thaw unconformity (MACKAY, 1978, 1992; BURN et al., 1986; MURTON & FRENCH, 1994; BURN, 1997; FRENCH, 1998; KOKELJ et al., 2002) due to a warmer climate that led to an increase in active layer depth. This thaw unconformity, which is a widespread phenomenon along the Yukon coast has been identified by the truncation of ice wedges and variations in cryostructure of ground ice (MACKAY, 1975; MURTON & FRENCH, 1994; FRENCH, 1998).

At this boundary not only cryostructures change significantly but sedimentary properties do as well and remain conspicuously similar below. Unfortunately, the basis of these deposits was not uncovered, while the maximum depth of any outcrop reached 5.8 m b.s. without knowledge about the exact elevation above sea level. Although the here so termed "main diamicton" was not recovered in direct connection with the "glacially deformed marine deposits" and its overlying "pebbly diamicton" but within the same slump, the main diamicton seems to lie relatively above the other two sedimentary beds since it was met at a relatively higher position.

In general, the very ice-rich deposits are grey to greyish-brown and hold a massive, often lens-like reticulated cryostructure. Gravimetric ice contents are usually higher than 50 % and sometimes exceed 100 %. The unbedded to weakly-bedded silty loams usually consist of more than 50 % silt-sized material and almost equal proportions of clay and sand (Tab. 5.1) leading to a very poor sorting. Single pebbles and cobbles are almost ubiquitous although they are less frequent than in the pebbly diamicton. However, the presence of a grain-size spectrum covering all fine fractions to a significant amount (Tab. 5.1) and the addition of coarser clasts correspond to a diamictic sediment.

Tab. 5.1: Comparative summary of grain size parameters for the "Main diamicton".

	Clay [%]	Silt [%]	Sand [%]	Mean (grain size)	Median (grain size)	Sorting (*Inman*)
MIN	20.0	49.0	5.0	7.0	4.0	2.2
MAX	33.0	67.0	26.0	35.0	14.0	3.5
Mean	25.6	56.0	17.7	21.0	7.8	3.1
Median	25.6	53.2	21.0	23.0	8.0	3.3

Moreover, shell fragments and little gastropods as well as organic matter in variable proportions are present in almost every sample. These facts again lead to the assumption that this diamicton was originally deposited in a shallow marine, maybe coastal environment because of the parallel occurrence of aquatic and terrestrial carbon sources (Fig. 5.1). Narrow C/N-ratios (10-15) and constant $\delta^{13}C$ values of about -26 ‰ support this view as the origin of organic matter indicate a mixed signal of C3 plants and algae (see Fig. 5.1), therefore suggesting a terrestrial and aquatic impact, too. In other respects, narrow C/N-ratios between 10 and 15 suggest that organics are highly to moderately mineralised (WALTHERT et al., 2004-2006) (Tab. 5.2).

Tab. 5.2: Characterisation of C/N-ratios (after WALTHERT et al., 2004-2006, altered)

C/N-ratio	Description	Rate of mineralisation
<10	very narrow	high
10-12	narrow	
13-16	moderately narrow	
17-20	moderate	moderate
21-25	moderately wide	
26-35	wide	low
>35	very wide	

Other key features of this sediment bed − that on the one hand give no further information about its genetic origin but on the other hand help to distinguish it from the overlying − is its constantly low content of TOC (<2 %), the presence of $CaCO_3$ (c3), a pH greater than 7.0 and a conductivity generally greater than 1500 μScm^{-1}. High electrical conductivity at

depth indicates that these sediments have not been subject to leaching, and implies that they have remained in permafrost (KOKELJ et al., 2002).

The main diamicton below the early Holocene thaw unconformity shows evidences of considerable deformation (Fig. 4.5) as it was subjected to folding and tilting. According to Mackay (1959) and Bouchard (1974) most of Herschel Island sediments have been affected by thrusting and overfolding; shear planes and inclined beds are present in all preglacial deposits (BOUCHARD, 1974) that make up the main body of the island. Here, the question arises what process might be responsible for the observed deformations within the diamicton. Today, a glacial origin of the island as a terminal moraine that was formed by glacier ice thrust and plough is uncontroversial.

Thus, a first mechanism that probably caused the deformation of sediments is ice-thrusting and glacial bulldozing, what is favoured by most authors. Many general characteristics of ice-thrust moraines have been observed on Herschel Island and published by Bouchard (1974). These are for example a topographic emergence, the presence of ridges with a curvilinear outline, folds, overthrusts and shearing, and the occurrence of a till. If the diamicton experienced deformation solely and finally by ice-thrust, it represents a till by definition.

Another option to explain deformed structures, at least within the main diamicton recovered here, is mass movement within highly water-saturated unfrozen and cohesive deposits. Immediately after deglaciation or while the ice margin retrograded, temperatures must have been high enough not only to melt glacier ice but to thaw and mobilise frozen deposits, too. Although, areas of hummocky and rolling topography resemble morainic topography indeed (RAMPTON, 1974), the general smoothness of geomorphology appears to be due to thermokarst and slope processes rather than primary glacial deposition. Consequently, folding, shearing and overthrusting in a scale as it was discovered in Figure 4.5 might be due to gelifluction on a glacially, high-energy relief prior to ground ice aggradation and immediately following deglaciation.

Since neither the basis of the main diamicton was reached during this study, nor the basis of a deep thaw event could be observed or is reported in any publication before, the option presented here remains questionable (Schirrmeister, *personal communication*). Additionally, Mackay (1975) reported that most of Herschel Island sediments are composed of deformed beds of sands, silts, and silty clays, therefore indicating a glacial

causation. Depleted isotopic signatures from texture ice within the main diamicton indicate a colder (Pleistocene) origin of pore water than the overlying material (see ch. 5.2).

At a depth of 3.5 m b.s., one sample gives a radiocarbon age of 50,770 (+3800/−2570) a BP, thus dating well beyond the last glacial maximum (LGM) of 20-22 ka BP. Regarding the formerly mentioned sedimentary deformations and the absence of a pre-late Wisconsin weathering horizon, it seems possible that glacially-reworked organic matter within marine or littoral deposits was dated.

Holocene colluvium & lacustrine deposits

The sediments treated here comprise all sampled surficial deposits of colluvial and lacustrine origin, which lie noticeably above the thaw unconformity or that have certainly been redeposited by slope processes.

The diamicton above the unconformity (upper diamicton) was subjected to intense mass movement due to the initiation of thermokarst processes during climate amelioration since the early Holocene (e.g. RAMPTON, 1974; MACKAY, 1990; KOKELJ et al. 2002; MURTON et al. 2005). High contents of organic carbon up to 45 % (profile COL 1 – Fig. 4.2, TSD 2 – Fig. 4.16, TSD-SP – Fig. 4.23, KOM – Fig. 34) occur above the discontinuity and indicate peat growth and soil formation processes on relatively stable surfaces for periods that lasted at least for centuries, maybe millennia. However, a repeatedly stepwise decrease in TOC contents down to 2 m b.s. indicate that redeposition and burial of organic-rich sediments might have occurred several times. A repeatedly reactivation of thaw slumps on Herschel Island is reported by Lantuit & Pollard (2005) and Lantuit & Pollard (2008) leading to burial incidents of peat and/or vegetation cover after a period of stable surface conditions that favoured plant growth. Besides slumping, gelifluction and frost creep − as movements resulting from freeze and thaw − occur on all gentle slopes. This produces a seasonal downslope movement of thawed material above the permafrost table. Gelifluction and frost creep produce the characteristic terracettes and lobes, and are continuous processes on slopes in contrast to thermokarst processes (SMITH et al., 1989).

Although surficial deposits might be of various origin, the majority of recovered materials show a grain size distribution (Tab. 5.3) that is highly consistent with that of the underlying main diamicton (Tab. 5.1). Every unit is very poorly sorted and comprises a

grain size spectrum that is silt-dominated (mean: >50 %) with significant but variable proportions of clay (24 %) and sand (18 %). Single pebbles and cobbles are present in colluvial deposits but are absent within the uppermost peaty sequences and within the whole organic-rich units at Komakuk Beach.

Tab. 5.3: Comparative summary of grain size parameters for colluvial and lacustrine deposits.

	Clay [%]	Silt [%]	Sand [%]	Mean (grain size)	Median (grain size)	Sorting (*Inman*)
MIN	9.0	42.0	4.3	8.0	5.0	2.2
MAX	35.0	68.0	49.0	102.0	59.0	3.5
Mean	24.0	58.0	17.5	23.3	10.9	2.9
Median	24.0	59.5	14.0	13.0	6.5	2.8

Surficial units, where thick peat sequences have developed, are characterised by a general absence of $CaCO_3$ and a synchronously lowered pH (<7.0). As organic remains are humified and mineralised by microbial decomposition during summer months, when the active layer is unfrozen, humic acids are released to soil waters (SCHEFFER & SCHACHTSCHABEL, 2002). This leads to a lowering of pH and a subsequent decalcification of the calcareous sediments in combination with an increased CO_2-solubility in cold waters (HENDL & LIEDTKE, 1997; AHNERT, 1999).

Low values of pH, furthermore, increase solubility and mobility of ions to migrate together with pore water movement. Downward pore water migration during summer months causes leaching of electrolytes into deeper strata towards the basis of the active layer (permafrost table) (KOKELJ & BURN, 2005) that acts as an aquifuge, although some base ions may have also been drawn downward along with water, from the active layer into near-surface permafrost (KOKELJ et al. 2002). That is why active layers usually possess lower electrical conductivities than its basis and the uppermost centimetres of the permafrost table (Figs. 4.7, 4.16, 4.34). Leaching of seasonally thawed soils contributes to a geochemical contrast between the active layer and the subjacent permafrost (KOKELJ & LEWKOWICZ, 1999; KOKELJ et al., 2002).

As organics have been analysed towards its origin and its state of preservation using C/N-ratios and stable carbon isotopes ($\delta^{13}C$), it becomes obvious that surficial sediments are of a broadly terrestrial origin or show a mixed signal between C3 land plants and algae, respectively. Since − within profiles TSD 2 and KOM − C/N-ratios rise mostly above 15

(max. 23), mineralisation seems to be reduced due to a high moisture content during growing season and land plants contribute to a stronger degree to organic remains. This is broadly supported by the presence of peat within most superficial deposits.

Figure 5.2 summarises the general sediment and ground ice stratigraphy as well as the (cryo)lithology and typical (cryo)structures of the studied outcrops on Herschel Island.

In general, surficial deposits have been subjected to intense cryoturbation as well as thermokarst since deglaciation and their exposure to permafrost or periglacial processes, respectively. Postglacial thermokarst modification has resulted in extensive lacustrine deposits and the redeposition of material through retrogressive thaw slumps (WOLFE et al., 2001). In addition, recently drained thermokarst ponds on level ground as well as ill-drained flats (e.g. Komakuk Beach) contain peat sequences (FROHN et al., 2005) and lacustrine fine sediments until 2 m b.s., characterised by pH below 7, a low conductivity and high TOC contents.
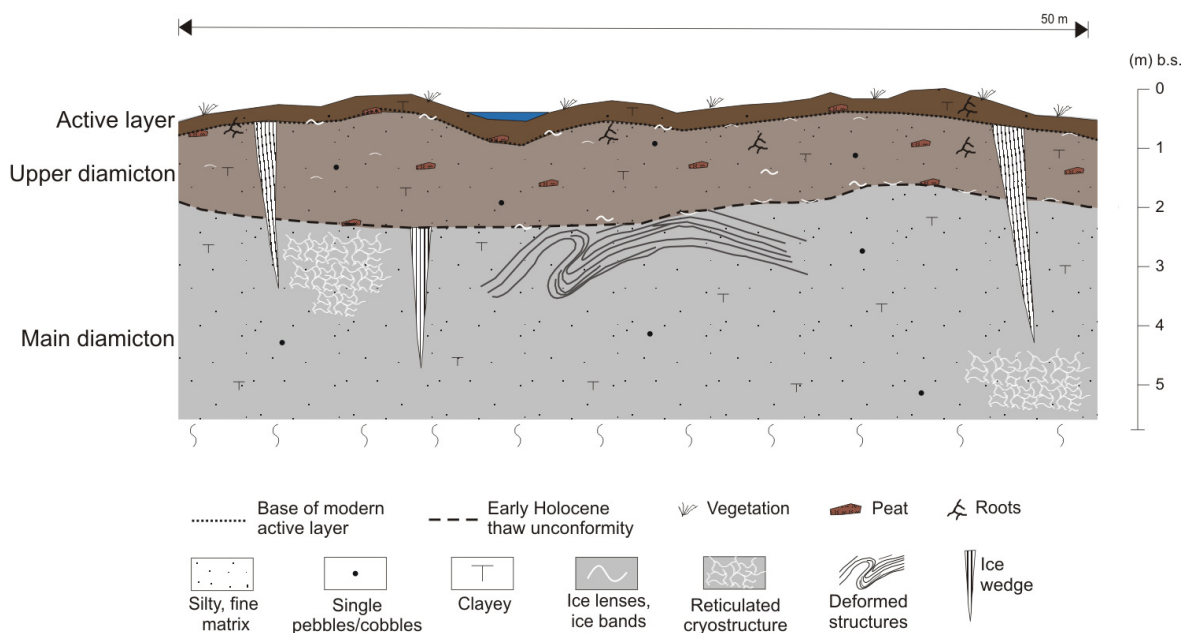
Fig. 5.2: Summarizing sediment and ground ice stratigraphy and lithology of studied outcrops on Herschel Island. Note that massive ice bodies of unknown origin are not integrated.

5.2 Nature and origin of ground ice

Ground ice, defined as all types of ice contained in frozen or freezing ground (HARRIS et al. 1998), is fed by meteoric waters sources (MEYER et al., 2002a) and can therefore be studied as paleoclimate archive by isotope methods (MACKAY, 1983; VAIKMÄE, 1989, 1991; VASIL´CHUK, 1991). Additionally, defining the cryolithological and cryostructural characteristics of ground ice with special regard to the adjacent or the incorporated sediments is helpful to unravel the stratigraphic subdivision of permafrost sequences (e.g. FRENCH, 1996; SCHIRRMEISTER et al., 2003) and for a distinction of different ground ice types (VAIKMÄE, 1991). Figure 5.3 summarises the isotopic composition of ice samples (and waters) according to their different genetic origin so that paleoclimate implications can be related to different ground ice types.
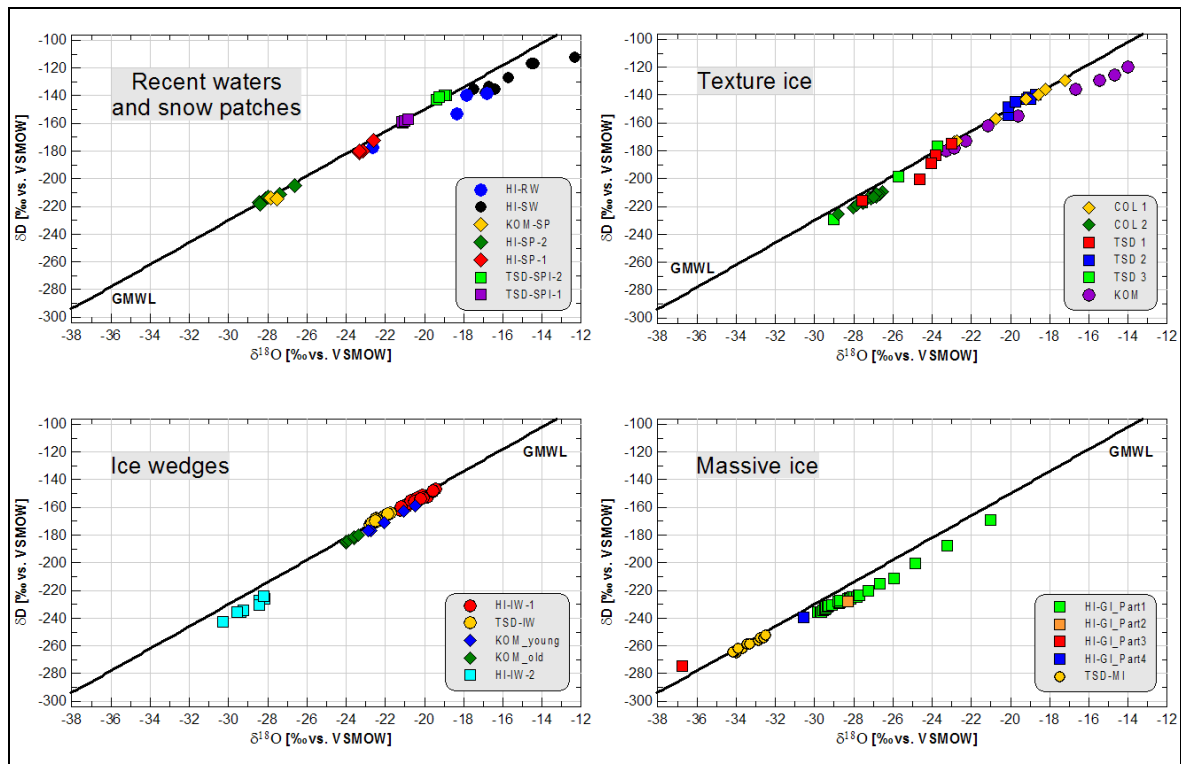
Fig. 5.3: Summary of the isotopic composition for ground ice of different genetic origin.

Recent waters and snow

The isotopic composition of modern precipitation and recent water bodies (e.g. thermokarst ponds, lakes) serves as the basis for applying paleoclimatic interpretations from the stable isotope composition in the sampled ground ice (SCHWAMBORN et al., 2006). Modern waters contribute to recent ground ice aggradation and thus enable the transfer of climatic information deduced from recent waters towards ground ice preserved in the permafrost.

Tab. 5.4: Summary of isotopic data of recent waters and snow.

Ice type	Sample group ID	Study site	N	$\delta^{18}O$ [‰] mean	$\delta^{18}O$ standard deviation	d-excess [‰] mean	Slope	Proposed stratigraphic affiliation
Rain water	HI-RW	–	4	-18.9	2.2	-0.9	6.8	Recent
Surface water	HI-SW	–	8	-15.6	1.6	-2.2	5.6	Recent
Snow patch	KOM-SP-1	KOM	2	-27.7	0.2	7.3	-1.9	Recent
Snow patch	HI-SP-2	COL 2	6	-27.8	0.6	9.4	6.8	Recent
Snow patch (buried)	HI-SPI-1	–	4	-23.1	0.3	6.3	11.3	??
Snow patch (buried)	TSD-SPI-2	TSD	4	-19.1	0.2	12.2	5.5	??
Snow patch (buried)	TSD-SPI-1	TSD	5	-21.1	0.1	9.9	7.6	??

Rain values and those from surface waters exhibit an isotopic composition that is relatively enriched in ^{18}O and show a distinct offset from the GMWL (Tab. 5.4, Fig. 4.39). Thus, the isotopic range of rain water (−22.7 to −16.8 ‰) is supposed to reflect summer conditions. However, only four rain events over a very short period were measured so that these values should not be overestimated. On average, surface waters are somewhat more enriched and show lower d-excess values (Tab. 5.4). Usually, surface waters show more negative values than summer precipitation as they are supposed to be fed by a mixture of winter and summer precipitation events, mostly over several years, as well as an additional groundwater supply. Consequently, this enrichment does not necessarily reflect climatic conditions. Both water types show a clear kinetic fractionation of isotopes since isotopically more enriched samples own lowest d-excess. Kinetic effects during re-evaporation of drops lead to a further enrichment of $\delta^{18}O$ in precipitating water, and to a decrease of the slope (JOUSSAUME et al., 1984) in the same way as evaporation from small water bodies results in a relative isotopic enrichment and a decrease in d-excess (GAT, 1995, 1996).

Recent snow patches clearly show lower isotope values than summer rain and are therefore supposed to reflect winter temperatures. However, the most likely buried snow patches appear slightly enriched in heavy isotopes. This could be due to isotopic exchange processes between snow and the adjacent sediments. According to Jean-Baptiste et al. (1998), the transport of hydrogen and oxygen atoms through solid ice is slow, whereas water vapour diffusion through the interconnected porosity is much faster. Another possible explanation for the enriched values is a higher temperature during (snow) vapour formation, thus probably representing summer snow, although summer snow should deviate from the GMWL towards lower d-excess (similar to summer precipitation) what is not the case here. Snow patch KOM-SP-1 exhibits an unusual negative slope of −1.9, a value that is certainly not related to natural processes but to the fact, that only two measurements are used to calculate the linear regression line. Consequently, this value is not statistically significant and hence not useful to interpret.

Ice wedges

One of the most promising archives for paleoclimate reconstruction are ice wedges, as their stable isotope composition reflects mean annual winter temperatures (ROMANOVSKY, 1976; VAIKMÄE, 1991; VASIL'CHUK & VASIL'CHUK, 1997; VASIL'CHUK et al., 2000a). Repeated cracking in the upper part of permafrost and infill with meltwater derived from winter precipitation leads to the formation of a vertically-foliated ice wedge. Isotope fractionation during the fast freezing process can be neglected (MICHEL, 1982; MACKAY, 1983), so that in the ideal case, the ice wedge isotopic signal (better: of every single ice vein) reflects the isotope composition of the original precipitation.

Ice wedges on Herschel Island should have begun to form in outwash and morainic deposits of Wisconsin age after deglaciation (RAMPTON, 1982), when dry and harsh climatic conditions supported frost cracking. The recovered Pleistocene ice wedge (HI-IW-2) was recognised by its truncation by the early Holocene thaw unconformity. This is broadly supported by comparable observations made by Mackay (1975, 1990), Pollard (1990) and Murton & French (1994).

Tab. 5.5: Summary of isotopic data of Pleistocene, Holocene and recent ice wedges.

Ice type	Sample group ID	Study site	N	$\delta^{18}O$ [‰] mean	$\delta^{18}O$ standard deviation	d-excess [‰] mean	Slope	Proposed stratigraphic affiliation
Ice wedge	HI-IW-1	COL 1	23	-20.5	0.5	8.7	7.2	Holocene
Ice wedge	TSD-IW	TSD	15	-22.3	0.3	10.3	7.4	Holocene
Ice wedge	KOM-IW-1-B1	KOM	5	-21.8	0.9	5.6	7.8	Recent
Ice wedge	KOM-IW-1-B2	KOM	6	-23.7	0.2	7.1	7.4	Holocene
Ice wedge	HI-IW-2	COL 2	10	-29.0	0.7	-0.3	7.9	Pleistocene

Its mean $\delta^{18}O$ signature (Tab. 5.5) is remarkably depleted (−29.0 ‰) compared to all other ice wedges that have been recovered and that penetrate the unconformity or that are not truncated. Thus, significantly colder winter temperatures are assumed during the formation of the initial snow that fed the ice wedge, in contrast to Holocene and more recent ice wedges. However, the very low d-excess (−0.3 ‰) is somewhat difficult to interpret as it does not agree with d-excess of meteoric waters, that should be closer to the GMWL. A slope very close to the value of **8** supports the persuasion in a meteoric water source for all ice wedges. Low d-excess values in ice wedges are reported by Dereviagin et al. (2002) and Meyer et al. (2002a,b) for the Laptev Sea Region. Sublimation and vapour exchange within a thin Pleistocene snow cover during dry and harsh climatic conditions could lead to low d-excess values (DEREVIAGIN et al., 2002). Another possible explanation is a different moisture source feeding Pleistocene ice wedges (DEREVIAGIN et al., 2002). Relocation of the circulation pattern by an extensive LIS might favour moisture originating from the Pacific Ocean (Meyer, *personal communication*) that is characterised by low d-excess (CLARK & FRITZ, 1997). However, the shares of processes affecting d-excess are not completely understood yet.

As reported by Mackay (1983), Holocene ice wedges sampled on Tuktoyaktuk Peninsula and Richards Island in the Mackenzie Delta area lie within a range of −26 to −22 ‰ ($\delta^{18}O$), in contrast to a truncated wedge that gave a value of −29 ‰ (Tab. 5.5). The mean isotopic compositions of snow and that of Holocene/Recent ice wedges differ as it would not have been expected, since ice wedges are supposed to resemble the snow signature. However, the sampled snow patches represent precipitation of only one or few winter(s), whereas ice wedges that do not crack annually (MACKAY, 1992) consist of numerous ice veins so that sampling, as it was performed here, would smooth individual isotope signals (VASIL'CHUK et al., 2000a).

An ice wedge (KOM-IW) consisting of two generations (Fig. 4.38) was recovered at Komakuk Beach, where this phenomenon is ubiquitous. The lower wedge was either truncated by thaw due to climate change, disturbance of vegetation cover, or the shift of drainage channels (WASHBURN, 1979); or the rate of peat growth raised and buried the older wedge. After an unknown period of time the wedge was reactivated so that a new generation started to grow and penetrated the older one. It becomes obvious that the lower wedge (δ^{18}O: −23.7 ‰), which grew syngenetically within a thick aggrading peat sequence is depleted by −2 ‰ over the younger generation (−21.8 ‰). This leads to assumption that the younger ice wedge generation formed during warmer conditions. However, the recent one does not reflect the warmest temperatures of all sampled ice wedges as the Holocene ice wedge (HI-IW-1) is less depleted by more than 1 ‰ (Tab. 5.5). Consequently, recent winter temperatures are not necessarily the highest ever observed in the study area since the Pleistocene-Holocene transition.

The fact that the old ice wedge generation (KOM-IW-1-B2) and the ice wedge (TSD-IW) penetrate the unconformity on Herschel Island, suggest that both wedges might have formed during climate deterioration following the HTM (~11-8 ka BP), possibly around 4.5 ka BP (RITCHIE, 1984).

Massive ground ice bodies

Within glacially-affected and ice-rich Herschel Island sediments, bodies of massive ice have been recovered whose appearance and isotopic composition is completely different to all other sampled ice types.

One ice body (TSD-MI − ch. 4.3.2) is made of milky white ice with sediment bands that are folded together with the ice and show anticlinal and synclinal as well as inclined structures. Its basis was not encountered while the top was truncated by either thaw or mass wasting (Fig. 4.29). δ^{18}O-isotopes are strongly depleted (−33.3 ‰) thus suggesting a Pleistocene origin with slope and d-excess near the GMWL, which indicate an unaltered meteoric water source. The question arises, whether the ice body aggraded prior to glaciation as massive segregated ice and was then deformed by glacier ice thrust. Or if the ice was originally basal glacier ice that was buried by supra-glacial till as a remnant of the Laurentide Ice lobe. Two main theories have been advanced to explain these massive icy

bodies. The first is that they are segregated ice bodies (MACKAY, 1971, 1973; MACKAY & DALLIMORE, 1992) fed by groundwater migrating towards a freezing front during permafrost aggradation (LACELLE et al., 2004), pore water expulsion or the freeze up of pressurized glacial meltwater onto the base of permafrost (LACELLE et al., 2007) immediately after deglaciation. A second interpretation is that these icy bodies are remnants of buried Pleistocene glacier ice (e.g. FRENCH & HARRY, 1990; LACELLE, 2004; MURTON et al., 2005), without a clear distinction being made between glacier ice derived from snow and subglacier regelation ice (LORRAIN & DEMEUR, 1985; FRENCH & HARRY, 1988, 1990; FRENCH, 1998).

Similar bodies of massive ice on Herschel Island have been reported by Pollard (1990), while Lacelle et al. (2004) stated that glacier ice can become buried during deglaciation by an insulating cover of till, which may exceed the active layer thickness. Alternating layers of debris-rich and bubble-rich but debris-poor ice are found. These features resemble glaciotectonic structures observed in deformed marginal or basal glacier ice (e.g., KNIGHT et al., 2000; MURTON et al., 2005). Buried glacier ice may contain significant quantities of stratified debris and may have experienced thawing and refreezing (regelation) (FRENCH & HARRY, 1990).

Tab. 5.6: Summary of isotopic data of massive ground ice bodies.

Ice type	Sample group ID	Study site	N	$\delta^{18}O$ [‰] mean	$\delta^{18}O$ standard deviation	d-excess [‰] mean	Slope	Proposed stratigraphic affiliation
			33	-28.1	2.1	0.7	7.2	Pleistocene
			5	-28.3	0.02	-1.1	2.0	Pleistocene
Massive ice body	HI-GI	HI-GI	5	-36.7	0.2	19.5	6.1	Pleistocene
			5	-30.5	0.3	5.1	6.5	Pleistocene
		Summary	48	-29.3	6.1	2.9	6.2	Pleistocene
Massive ice body	TSD-MI	TSD	11	-33.3	0.6	8.0	7.2	Pleistocene

Low variations in isotopic signature within the ice body (TSD-MI) suggest only one water source and stable freezing conditions during ice formation. A slope of 7.2 and a d-excess of 8.0 ‰ (Tab. 5.6) indicates a meteoric water source being largely unaffected by secondary processes (secondary freeze, regelation) as they occur during the formation of segregated ice. The d-excess for Laurentide ice (Pleistocene precipitation) preserved in the

Barnes Ice Cap (Baffin Island) is equal to 7 ±3 ‰ (LACELLE et al., 2004). The light oxygen isotope ratios from TSD-MI are very similar to the average of −33 ‰ measured for Laurentide ice at the base of the Barnes Ice Cap (ZDANOWICZ et al., 2002). Additonally, Dansgaard and Tauber (1969) estimated the average $\delta^{18}O$ value for Laurentide Ice at < -30 ‰ from Camp Century (Greenland).

Therefore, there is strong evidence that Pleistocene basal glacier was deformed during ice thrust, then became sheared off and was incorporated into glacial diamicton or became buried by supraglacial meltout till (MURTON et al., 2005).

Another massive ice body (HI-GI − Figs. 2.17, 4.31, 4.32) of unknown but supposedly glacial origin was encountered adjacent to large striated boulders of clearly glacial force and within brownish-grey deposits with a significant content of organic matter and macro-remains. Firnified glacier ice tend to have a high bubble content distributed randomly, whereas massive segregated ice bodies tend to have variable crystal sizes and a low bubble content (LACELLE et al., 2007). HI-GI exhibits both features. (1) It is made of very pure ice, almost free of bubbles and enriched in heavy isotopes in one part in contrast to (2) a very bubble-rich part that shows strongly depleted values. With −36.7 ‰ on average for $\delta^{18}O$, the milky white (bubble-rich) ice (Part 3) exhibits the lowest isotopic values that have been measured on ground ice during this study. The mutual appearance of erratics and very strongly depleted isotopic values at least in a part of the ice body leads to the question whether the ice is of glacial origin or if the water source is of glacial origin. Uncon-formable upper and lower contacts do account for a buried origin (MACKAY, 1989), although sediment incorporations at one edge of the ice body speaks for a segregated origin of HI-GI. Nevertheless, the water feeding the ice body definitely formed during cold climate conditions as they do not occur today. No other ice type recovered here, indicate such cold climate conditions as they prevailed during the massive ice formation or its water source.

As reported by French & Harry (1990) there might be a progressive change in water quality within a massive segregated ice body, although some massive ice bodies of probably glacial origin may have experienced partial thawing and subsequent regelation that altered the isotopic composition prior to ultimate preservation/burial (FRENCH & HARRY, 1990). A strong isotopic gradient trending from a relatively "warm" oxygen isotopic signature (−21.0 ‰) at the ice margin towards a "cooler" signature (~ −26 ‰)

about 30 cm in the ice interior (see Figs. 4.32, 5.3) might reflect an isotopic enrichment due to regelation and isotopic exchange processes at the ice-sediment interface (ZDANOWICZ et al., 2002). However, a further inward depletion in ^{18}O cannot be explained by diffusion processes. If a linear regression line (slope) is drawn, excluding the outer samples that have experienced isotopic exchange as well as the most negative sample (part 3), then the extended regression line meets the most negative value (Fig. 5.4). Additionally, the slope from HI-GI plots well below the global meteoric water. That is regarded to represent a freezing slope and is therefore consistent with an origin as regelation ice or segregated-intrusive ice (MURTON et al., 2005). According to Souchez et al. (2000), the freezing slope is always lower than the slope of the GMWL.
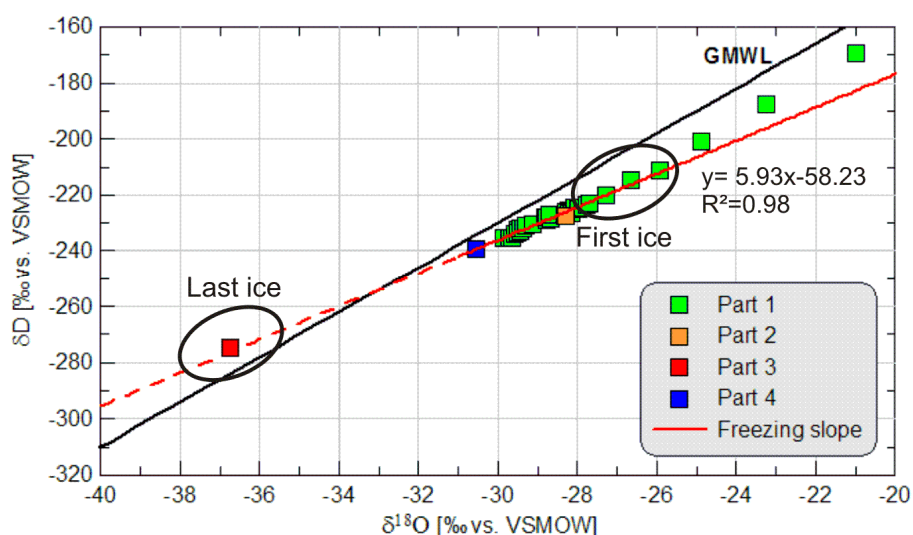
Fig. 5.4: Isotopic composition of massive ice body (HI-GI) and its interpretation towards its origin.
Note that all samples (except those affected by isotopic exchange processes) fit a linear regression line below the GMWL, termed "freezing slope". It is supposed that all parts derive from one water source that froze under closed-system conditions from the outside into the inner, leading to fractionation along a freezing slope. The innermost part becomes strongest depleted in contrast to the outer margin.

Taking into account all information about the stratigraphic position, isotope composition and its general appearance, the following conclusions about the origin of HI-GI can be drawn.

(1) HI-GI most likely does not represent buried glacier ice due to strong variations in appearance and isotopic composition. Despite strong isotopic differences, all samples – except those affected by isotopic exchange processes – lie almost exactly on the linear regression line. Thus, only a single water source is assumed.

(2) It seems likely that the ice body formed under closed-system conditions and derived from glacial meltwater. Pressurised glacial meltwater or a fragment of glacier ice was buried under till and melted. As the glacier retreated, the permafrost table rose and enabled slow freezing of the water body from outside to the interior accompanied by kinetic fractionation.

Clark and Fritz (1997) have shown fractionation for finite water bodies in an evaporative system. "During evaporative enrichment of water, the vapour will have a reciprocal depletion, and plot on the same evaporative line, but opposite the initial composition of the water" (CLARK & FRITZ, 1997 p.43). Closed-system freezing is an analogue. Consequently, the first ice is enriched in $\delta^{18}O$ while the residual water and so the last ice becomes progressively depleted. Bubbles are forced into the interior during the freezing process. That is why the isotopically depleted ice that froze last is bubble-rich, whereas the first ice has almost no bubbles and is enriched in ^{18}O.

Texture Ice

Even though preservation of soil moisture in texture ice occurs in a complex way, it can still reflect environmental and climatic changes under certain circumstances (SCHWAMBORN et al., 2006). Those changes can be resolved by interpreting the texture ice record (MURTON & FRENCH, 1994; KOTLER & BURN, 2000). At most sites a reticulated pattern of segregated ice is commonly present in fine-grained sediments. These patterns develop during freezing of saturated fine-grained sediments (ice aggradation) (MACKAY, 1989). A coarser lens-like pattern with parallel ice lenses of variable thickness occurs above the early Holocene thaw unconformity. This might be due to two-sided freezing with the onset of climate deterioration after the HTM. Permafrost at the base and directly above the base of the active layer is characteristically ice-rich due to downward moisture migration from the active layer into frozen ground and two-sided freezing at the end of summer (MACKAY, 1983; BURN & MICHEL, 1988; KOKELJ et al., 2003).

Stable isotopes within texture ice from below and above the thaw unconformity show great variations (Tab. 5.7). At Collinson Head and Thaw Slump D, $\delta^{18}O$ values below the unconformity lie on average below −26 ‰. Even though the exact water source, the processes of ice formation and isotopic fractionation processes could not be clarified conclusively, the strong gradient in isotopic composition of about 7 ‰ ($\delta^{18}O$) points to

differences in paleotemperatures during ground ice aggradation. These values compared with $\delta^{18}O$ values obtained from Pleistocene glacier ice (i.e. Barnes Ice Cap values ranging from −42 to −26 ‰) (ZDANOWICZ et al., 2002) suggest that texture ice below the basis of the paleoactive layer formed during the Pleistocene.

As the active layer deepened, Holocene precipitation mixed with the ^{18}O-depleted Pleistocene meltwater in the thaw zone above the unconformity (LACELLE et al., 2004). This is clearly visible in the isotopic composition of at profiles Komakuk Beach, COL 1 and TSD (average $\delta^{18}O$: −19.9 to −18.9 ‰, Tab. 5.7), which is approximately 7 ‰ enriched over supposedly Pleistocene meltwater that contributed to texture ice formation.

Tab. 5.7: Summary of isotopic data of texture ice.

Ice type	Sample group ID	Study site	N	$\delta^{18}O$ [‰] mean	$\delta^{18}O$ standard deviation	d-excess [‰] mean	Slope	Proposed stratigraphic affiliation
Texture ice	KOM	KOM	9	-18.9	3.5	0.1	6.4	Holocene
Texture ice	COL 1	COL 1	7	-19.9	2.1	9.4	8.0	Holocene
Texture ice	TSD 2	TSD	8	-19.4	0.5	10.3	8.0	Holocene
Texture ice	COL 2	COL 2	17	-27.2	0.6	3.3	7.1	Pleistocene
Texture ice	TSD 3	TSD	4	-26.5	2.0	6.8	9.9	Pleistocene
Texture ice	TSD 1*	TSD	5	-24.6	1.6	4.3	8.7	??

* Texture ice data from profile TSD 1 was rejected from interpretation as it was sampled horizontally adjacent to the massive ice body of TSD-MI. Nevertheless, there exists an isotopic gradient from depleted $\delta^{18}O$ values at the ice-rich transition to the massive ice (−27.6 ‰) to more enriched values (−23.0 ‰) with greater distance pointing to mixing processes at the diffuse boundary to pure ice.

The d-excess can provide further information on the origin of the moisture before ice formation as it is affected by relative humidity during the formation of primary vapour masses (DANSGAARD, 1964). It might be reduced to values lower than 0 ‰ by non-equilibrium fractionation during subsequent phase changes, including evaporation or freezing. The here observed d-excess values vary over a wide range (0.1 to 10.3 ‰) so that it becomes complicated to draw a general image about the water source and the extent of secondary non-equilibrium processes. However, taking into account that Lacelle et al. (2004) estimated that the $\delta^{18}O$ value of early Holocene precipitation in this region was as high as −21 ‰, secondary non-equilibrium fractionation are most likely for isotopic enrichment by 2-3 ‰ and low d-excess values (Tab. 5.7). Various reasons may account for this shift.

(1) Fractionation during (slow) freezing is accompanied by a shift towards heavier isotopic values, which may reach up to 3 ‰ in $\delta^{18}O$ (SOUCHEZ & JOUZEL, 1984, VAIKMÄE, 1991).

(2) Secondary evaporation from the active layer might be responsible for isotopic enrichment as well as for the lowered d-excess.

(3) Climate cooling since the end of the HTM would reduce enrichment of ^{18}O as it has an opposite effect on the isotopic composition.

Arguments (1) and (2) are supported with a view on the isotope data at Komakuk Beach (Fig. 4.37). D-excess is strongly correlated with depth within the upper part of the profile above the distinct sedimentary boundary (Fig. 4.34) as it decreases from 1.9 to −8.2 ‰ bottom up while $\delta^{18}O$ decreases as well from −19.6 to −14.0 ‰ (Fig. 4.37). At first, this implies rising temperatures. However, strongly enriched $\delta^{18}O$ values, a slope of 6.4 and the displacement from the GMWL (low d-excess) support secondary evaporation during aggrading peat sequences. Despite of fractionation processes, which may occur during freezing and evaporation, and despite of different water sources participating during its formation, texture ice in soils may also be used for paleoclimatic studies (MEYER et al., 2000).

5.3 An appraisal of landscape evolution

A summarising view of the different stages of landscape evolution since the Late Pleistocene is proposed in Figure 5.5.

Period	Environmental records
Late Holocene	- Recent climate warming - Thaw slump activity - Tussock tundra - $\delta^{18}O: \geq -24‰$ $\rightarrow$ relatively warm winters - Extensive coastal erosion - Ice wedge reactivation during climate deterioration
Early Holocene Thermal Maximum (HTM)	- +1-2°C warmer than today - Wetter than today and previously - Peat growth - Ice wedge truncation - Active layer deepening $\rightarrow$ Thaw unconformity - Thaw lake formation and retrogressive thaw slumps - Increased thermokarst - Intense reworking $\rightarrow$ colluvium - Smoothed topography
Late Pleistocene periglacial period	- Still lowered sea level - Arctic steppe tundra - Permafrost aggradation - $\delta^{18}O: < -27‰$ $\rightarrow$ relatively cold winters - Ice wedge growth - Few sedimentation - Part of land mass "Beringia" - Still very harsh climate - Dryer than previous period
Late Pleistocene glaciation	- $\delta^{18}O: < -30‰$ $\rightarrow$ relatively cold winters - High-reliefed topography - Push-moraines - Burial of glacier ice - Ice thrust, glacial plough - Westward moving lobe of Laurentide Ice Sheet

Fig. 5.5: Summary of stages in landscape evolution in the study area.

Late Pleistocene glaciation

Today, there is no doubt that Herschel Island was formed as a terminal moraine by glacial ice-thrust during the Late Pleistocene (Buckland glaciation). Shear at the base of an advancing or oscillating glacial margin incorporated basal glacier ice into adjacent material

or became buried by supraglacial melt-out till (MURTON et al., 2005). Glacier ice or at least glacial meltwater is proved by low oxygen isotope values below −33 ‰.

However, it is still uncertain when Buckland glaciation took place. The age of northwest Laurentide margin's greatest extent is still an important question regarding whether it is generally of global LGM age or older (DYKE et al., 2002). The model presented by Bartlein et al. (1991) described the interval from 70 to 28 ka BP (Middle Wisconsin = MIS 3) as having very cold, continental climates year-round with low variations through time (ELIAS, 2001). However, sedimentological and paleobotanical evidence suggest that the interstadial was a period of relatively warm, moist climate, but conditions still remained more severe than during the Holocene (ANDERSON & LOZHKIN, 2001).

But the agreement is that the Middle Wisconsin (MW) was a time of reduced ice cover elsewhere in glaciated North America (DYKE et al., 2002). Thus, glaciation of the study area took place most unlikely during MW. Furthermore, many authors favour a reduced ice extent during LGM (HAMILTON, 1986, 1994; SVENDSEN et al., 1999; MANGERUD et al., 2002; BRIGHAM-GRETTE et al., 2003; GUALTIERI et al., 2003). These reconstructions suggest that especially the Eastern Siberian and Barents-Kara ice sheets reached their maximum extent >60 ka BP (MANGERUD et al., 2002; BRIGHAM-GRETTE et al., 2003; ENGLAND et al., 2006). In contrast to these views from Siberia, Duk-Rodkin et al. (1996) postulates on the basis of ^{36}Cl-dates that Laurentide Ice Sheet "reached its all-time maximum by c. 30,000 years BP" (DUK-RODKIN et al., 1996). Nevertheless, the oldest date obtained from Herschel Island during this study at 3.5 m b.s. gave an age of 50,770 +3800/−2570 BP although I cannot exclude that dated material represents reworked organic matter within originally near-shore marine silty loams.

Glacially-folded and -thrusted marine sediments with an apparent carbonate content and high conductivity values due to their marine origin were deposited as morainic ridges with a high relief. This strong relief and great absolute elevations makes the island unique on the otherwise level to gently-sloping Yukon Coastal Plain. Only the ice-thrusted ridge between Kay Point and King Point is of similar origin (MACKAY, 1959).

Late Pleistocene periglacial period

As the ice margin melted during the Late Pleistocene or did not advance once again in the study area, Herschel Island became ice-free and part of a periglacial environment with a harsh full arctic climate. Under the influence of the remaining ice cap, which had retreated within the Mackenzie Delta area (Sitidgi Stade, 13 ka BP − RAMPTON, 1988), cold and dry conditions prevailed so that Pleistocene ice wedge growth and ground ice aggradation re-started. This is supported by the presence of one sampled ice wedge (HI-IW-2) that was truncated in the early Holocene and therefore formed during ice-free conditions during the Late Pleistocene. Moreover, texture ice below the early Holocene thaw unconformity is depleted in ^{18}O (<-26 ‰) and corresponds well to the isotopically "cold" Pleistocene ice wedge ($\varnothing\ \delta^{18}O = -29$ ‰).

During the late Wisconsin, unglaciated Yukon, isolated from the rest of North America by glaciers and connected with Far East Asia via the Bering Land Bridge, became part of eastern Beringia (SCHWEGER, 1997). During this cold and arid phase, the driest and most hostile Beringian environments were the lowlands flanking the Beaufort Sea, i.e. the Arctic Coastal Plain of northern Alaska and Yukon (HOPKINS, 1982; DINTER et al., 1990) including Herschel Island. This area occupied the rainshadow of moisture sources in the Gulf of Alaska and the Bering Sea, and it is likely that a closed sea-ice cover on the Beaufort Sea combined with a lowered sea level reduced moisture supply from the north (BATEMAN & MURTON, 2006). The moisture source in general might have shifted as the global circulation was strongly affected by the presence of the LIS and the Beringian Land Bridge (ENGLAND et al., 2006) until its inundation by ~ 11 ka BP and the re-establishment of the circulation between the Pacific and Arctic oceans (ELIAS et al., 1996).

Cold and arid conditions thus favoured a stable periglacial landscape with reduced sedimentation and landscape-shaping processes.

Holocene Thermal Maximum

According to Ritchie et al. (1983), a maximum summer solar radiation at high latitudes of the Northern Hemisphere occurred at 10 ka. Milankovitch Theory predicts greater summer radiation by 9-10 % and summer temperatures of 3-6°C warmer than today (RITCHIE et al., 1983).

On the Yukon Coastal Plain, the formation of thermokarst lakes peaked between 11.6 and 10.3 ka BP (RAMPTON, 1988), suggesting greatest warmth during this interval (KAUFMAN et al., 2004). In the vicinity of Herschel Island, however, bathymetric charts show a narrow continental shelf, so that the shoreline was only 4 to 15 km north of the island in the early Holocene (MATTHEWS, 1975). This suggests that arctic maritime effects (KOKELJ et al., 2002) cooled the study area in comparison to other regions along the coastal plain to the west.

Thickening of the active layer between 10.3 and 9.1 ka BP is documented by a widespread thaw unconformity along the Arctic coast of northwest Canada (MACKAY, 1978, 1992; BURN et al., 1986; MURTON & FRENCH, 1994; BURN, 1997; FRENCH, 1998; KOKELJ et al., 2002). However, the depth of the thaw unconformity (~1.5-2.5 m) does not resemble the thickness of the paleoactive layer since there is a variable amount of excess ice above the unconformity (MACKAY, 1972; BURN, 1997) and mass wasting processes might have added some material. Subtracting the excess ice content from the interval between the base of the active layer and the unconformity at undisturbed sites provides estimates of paleoactive layer thickness that is approximately double the present active layer thickness (KOKELJ et al., 2002).

Stable isotope values from texture ice between the base of the modern and paleoactive layer exhibit warmer conditions as they prevailed during Pleistocene times.

During the period of deeper thaw, mass deposition from upslope proceeded − especially on high-relief Herschel Island − as shown by the numerous clods of peat and buried organic matter above the thaw unconformity (MACKAY, 1990). Thaw mobilisation of sediments resulted in the transport of mudflow sediments from upland areas into adjacent basins by gelifluction (HARRY et al., 1988). Because of repeated episodes of thermokarst modification (e.g. block slumping, active layer detachment slides, formation of retrogressive thaw slumps) and gelifluction much of the postglacial morphology of the Island has experienced significant smoothing. Thick colluvial deposits with variable content of TOC and occasional clods of peat support this view of a highly active period in landscape development.

On level ground surfaces, the HTM is directly connected with the formation of thermokarst lakes. Deep thaw led to the degradation of excess ice and massive ground ice so that the ground surface subsided by the volume it contained ground ice in excess, which had

melted and drained (POLLARD & COUTURE, 2007). Furthermore, where surfaces remained stable, high net primary productivity in response of early Holocene climate amelioration (EISNER et al., 2005) led to the growth of thick peat sequences (SHUR & JORGENSEN, 1998) as they have been recovered at Komakuk Beach. Microfossil analyses by Eisner et al. (2005) indicate that, in the early Holocene, the local landscape was wet and conditions were eutrophic.

Pedogenetic processes and peat growth on a stable surface are confirmed by many analytical results.

(1) TOC contents are enriched towards values between 5 and 45 %, whereas all deposits below the unconformity contain less than 2 % organic carbon. Reworked deposits by mass-wasting processes exhibit only slightly enriched values.

(2) Values of pH increase significantly with increasing depth in highly organic sequences. This is due to carbonate leaching and the release of humic acids in well-aerated horizons during decomposition of organic matter.

(3) Directly at the base of the peat sequence at Komakuk Beach, the only prominent peak in magnetic susceptibility occurred. An amorphous black and strongly magnetic crust covers organic remains. This is most likely due to the formation of secondary iron sulphides in an anoxic environment. If there is high bacterial production of H_2S because of high rates of organic matter sedimentation and minimal circulation, iron sulphides can then be precipitated directly (TUCKER, 1991). Ferromagnetic Greigite (Fe_3S_4) and Mackinawite (($Fe,Ni)_9S_8$) as well as non-magnetic Pyrite (FeS_2) may contribute to mineral assemblage of this peat (SIEGERT, 1987; HILTON, 1990; Siegert, *personal communication*).

(4) During thaw period, there is a downward ion migration with seeping water within the active layer, especially at co-occurrence of lowered pH within peat sequences. Increasing conductivity values with depth depict leaching of ions towards the permafrost table, where they concentrate, which leads to a peak in conductivity. This effect was also considerable at the base of the paleoactive layer in undisturbed profiles.

The base of the peat sequence at Komakuk Beach (2.7 m b.s.) gave an age of 8405 ±45 a BP (9521-9372 cal a BP). This is consistent with several age determinations at the

unconformity along the Yukon Coastal Plain reported by Harry et al. (1988), Mackay (1990), Kaufman et al. (2004) that yielded ages between 10.3 and 7.9 ka BP.

In summary, the early Holocene Thermal Maximum (approximately 11-8 ka BP) was a period of greater summer warmth due to a Milankovitch insolation peak (RITCHIE et al., 1983). Additional warming promoted peat growth (EISNER, 1991) and forced deeper thaw of permafrost in general as well as ice-rich deposits in particular. This led to a truncation of previous cryostructures (MACKAY, 1975; MURTON & FRENCH, 1994), thaw lake formation (e.g. RAMPTON, 1988; EDWARDS & BRIGHAM-GRETTE, 1990) and enhanced redeposition of material by slope processes and thermokarst (WOLFE et al., 2001).

Middle & Late Holocene

Climate deterioration

Reconstructions indicate warmer-than-present conditions from 11 to 8 ka BP, after which temperatures declined steadily until about 5 ka (KAUFMAN et al., 2004). A transition to near-modern temperatures occurred between 6.7 and 5.6 ka (KAUFMAN et al., 2004). During the late Holocene, the Coastal Plain experienced overall cooling with generally drier conditions after 4.5 ka BP (EISNER, 1999). As the climate gradually cooled, the active layer thinned and some of the ice wedges, that have been previously truncated during the HTM, were reactivated (MACKAY, 2000). According to Ritchie (1984), the renewed ice wedge growth may have started at about 4.5 ka BP. The rise of the permafrost table led to a decrease in thermokarst and mass wasting activity. Relatively stable surface conditions are necessary for ice wedge growth and repeated frost cracking, which in turn are responsible for a re-establishment of polygonal ground. Average isotope signatures from Holocene ice wedges range from −20.5 to −23.7 ‰, thus representing considerably warmer winter temperatures as they are enriched by 5.3 to 8.5 ‰ compared to the Pleistocene ice wedge.

Late Holocene & Recent conditions

Reworking of ice-rich sediments since the HTM has produced an upper diamicton above the unconformity that mantles much of the landscape (DE KROM, 1990). This process is still in progress, even though it is restricted to the upper part since the rising permafrost table stabilised the remaining deposits between the modern and paleo-active layer.

Earth hummocks and patterned ground are prominent features of Herschel Island permafrost landscape. These features are abundant on moderately well-drained positions. Non-sorted nets, circles and stripes (WASHBURN, 1980) are the most common on fine-textured soils of Herschel Island. These features develop as a result of cryoturbation. Gelifluction and frost creep result from freeze-thaw cyclicity and occur on all gentle slopes. This leads to a seasonal downslope movement of thawed material above the permafrost table (SMITH et al., 1989). Lacustrine deposits in thaw lake basins formed e.g. as a result of massive ground ice melt (HILL, 1990), leading to ground subsidence and water infillment.

The morphology of rolling and hummocky terrain seems to be due to thermokarst development rather than primary glacial deposition (RAMPTON, 1982). The upper 3 m of deposits (upper diamicton) is commonly debris flow, lacustrine, or colluvial deposits that have been reworked by a number of freeze-thaw cycles or thermoerosion and that have similar textures to the underlying till (main diamicton) (BOUCHARD, 1974). As Rampton (1982) puts it, intense reworking leads to a subdued morphology of moraines.

Drainage on Herschel Island is relatively good because of high relief energy in contrast to Komakuk Beach, although peat accumulates on flat areas and in thermokarst ponds on the island, too. Active layer detachment slides and retrogressive thaw slumps are common on steep slopes (DE KROM, 1990) on Herschel Island only, whereas thermal niching and block slumping occur along all coastlines exposed to wave erosion (RAMPTON, 1982). Retrogressive thaw slumps are prominent thermoerosional features on Herschel Island with a great erosional and thus landscape-shaping potential. They are often polycyclic in nature (LANTUIT & POLLARD, 2005). This refers to the formation of a new retrogressive thaw slump within the floor of an older one (MACKAY, 1966; WOLFE et al., 2001). An example for the existence of more than one slump generation becomes evident with a view on the morphology of Thaw Slump D (Fig. 2.16) and on radiocarbon ages obtained from study site Collinson Head No.2 (COL 2). Table 5.8 reveals several age inversions within slumped material. This leads the interpretation that in recent times, at least two slump events took place and reworked organic matter as well as soils (paleosols) that have developed on temporarily stabilised slump floors. Lantuit (2008) supposes the existence of a ~250-years cycle of thaw slump activity in the coastal zone on Herschel Island.

Tab. 5.8: Age-depth relationship for COL 2.

Depth	Radiocarbon age
[m] below surface	[^{14}C a BP]
3.5	50,770 (+3800/−2570)
2.3	>1954 A.D. (*)
1.1	625 ±35
0.9	1110 ±35

(*) Probably contaminated material was dated.

Since glaciation, it is believed that the southwest shore of Herschel Island has retreated by 1 to 2 km (MCDONALD & LEWIS, 1973). McDonald and Lewis (1973) documented average horizontal coastal retreat rates of 0.66 m/a on Herschel Island for the 1944-1970 period. More recently, Lantuit and Pollard (2008) calculated annual coastal retreat rates to be 0.61 m/a for the 1952-1970 period and 0.45 m/a for the 1970-2000 period. Since the relative sea level has stabilised by about 6-5 ka BP (BAUCH et al., 1999, 2001) at the end of the postglacial (Flandrian) transgression, longshore currents paralleling the coast contribute to the formation of spits and bars (Osborne Spit, Herschel Spit, etc.), where coastal sections are not subjected to coastal erosion.

6 CONCLUSIONS & OUTLOOK

The aggradation and degradation of massive ground ice has formed major control on the late Quaternary landscape evolution of Herschel Island since ground ice makes up a significant content of the upper permafrost. The complex stratigraphy is attributed to the interactions between the northwestern margin of the Laurentide Ice Sheet and the permafrost beneath. Glacier ice thrust caused deformed permafrost that is dominated by glaciotectonic structures such as simultaneously folded sediments and cryostructures indicative of ductile deformation. Very similar structures have been recovered by Murton et al. (2004, 2005) and Murton (2005) along the Tuktoyaktuk Coastlands. Stagnation and/or oscillation of the LIS on Herschel Island was accompanied by melt-out of glacigenic debris of a formerly marine near-shore origin, resulting in the widespread formation of a compact diamicton and burial of basal glacier ice. Additional ground ice formed since ice-free Pleistocene conditions and during the Holocene as well.

Combining information about strong variations in the sedimentological and stable isotopic record, it becomes obvious that the study area has undergone significant climatic and environmental changes since the Late Pleistocene. Unfortunately, the transition from glacial towards periglacial conditions (i.e. deglaciation) on Herschel Island could not be timed more exactly than other authors did before and is still very uncertain. But it is evident that since deglaciation the study area was extensively affected by periglacial landscape-shaping processes. Their impacts on landscape development have been ascertained with the help of a multidisciplinary (multi-proxy) research approach, which leads to the following conclusions:

1. Wisconsin glaciation caused:
   - deformation of massive segregated ice and frozen sediments,
   - the emplacement of a diamicton above the glacially deformed sequence;
   - and the burial of basal glacier ice.

2. Deglaciation of the island was accompanied by thermal contraction cracking and ice wedge formation within glacially deformed permafrost.

3. Climate warming during the early Holocene caused active-layer deepening, which truncated the tops of ice wedges and those of previously formed cryostructures

beneath. A pronounced early Holocene thaw unconformity dates back to at least 8.4 ka BP and indicates a significantly warmer climate than present.

4. The following climate deterioration caused active-layer thinning, allowing ice-wedge growth to reactivate. Segregated ice formed in the whole paleoactive layer above the unconformity during restarted permafrost aggradation.

5. Melting of massive ground ice and ice-rich materials during warm intervals and periods of enhanced coastal erosion have produced numerous large retrogressive thaw slumps, which, on the one hand expose vertical permafrost sequences and thus enable the study of Herschel Island stratigraphy, but on the other hand complicate local stratigraphical approaches by relocation of material due to mass wasting processes.

Different types of ground ice have been recovered that are useful as paleotemperature proxy to a variable degree. By all means, ground ice of Pleistocene as well as Holocene age is present as their isotopic signals and stratigraphic position suggest. Holocene and Pleistocene sequences are excellent to distinguish since their isotopic signals differ drastically by about 8 ‰. Buried glacier ice could be encountered with great certainty – a paleoenvironmental proxy that remained unaltered since it came into existence and thus keeps information from past environmental conditions unchanged, too.

Finally it seems undoubted that during the late Wisconsin glaciation, when glaciers did not advanced towards the study area again, unglaciated Yukon, became part of eastern Beringia. But the question remains, for how long the study area stayed unglaciated, until the timeframe of deglaciation is not appointed more exactly. This information is essential to gain precise knowledge about pre-Holocene environmental variations in an area with strong environmental gradients in the proximity of a glacier margin and coastal influence.

Despite the great amount of paleoenvironmental records, paleoecological statements about ground cover, plant communities and hence variations in summer temperatures in the past remain difficult since paleoecological studies on pollen and fresh-water ostracods are missing but are in progress. Further detailed absolute age determinations are needed to verify or falsify a specific time span of polycyclicity in slump events and to refer paleoenvironmental events to distinct climate periods. To better understand landscape and environmental history of Herschel Island and the Yukon Coastal Plain as a whole a continuous sedimentary sequence from lakes or drained lake basins covering the entire

Holocene and even the Late Pleistocene, too, are supposed to provide further detailed paleoenvironmental information. Many circum-arctic studies focus on sediment sequences from unglaciated Beringia with the aim of paleoenvironmental reconstruction. But only few of these use multi-proxy analyses in one stroke (i.e. sediments for reconstructing depositional conditions and transport forces, microfossil analyses to infer summer temperature variations *and* stable water isotopes as paleo winter temperature proxy). So, further research is needed to get an encompassing image about climate and landscape development in past times to predict future changes in a highly vulnerable region against the background of a warming Arctic.

7 REFERENCES

ACIA (2004). Impacts of a warming Arctic: Arctic Climate Impact Assessment. Cambridge University Press. Cambridge.

AD-HOC-AG BODEN (2004), Bodenkundliche Kartieranleitung, 5th ed. Hannover. 438p.

AGRICULTURE CANADA EXPERT COMMITTEE ON SOIL SURVEY. (1987). The Canadian System of Soil Classification. 2nd ed. Agriculture Canada Publication. 1646. 164p.

AHNERT, F. (1999). Einführung in die Geomorphologie. 2nd ed. Ulmer, Stuttgart.

BATEMAN, M. D., MURTON, J. B. (2006). The chronostratigraphy of late pleistocene glacial and periglacial aeolian activity in the Tuktoyaktuk Coastlands, NWT, Canada. Quaternary Science Reviews 25 (19-20). 2552-2568.

BAUCH, H., KASSENS, H., ERLENKEUSER, H., GROOTES, P.M., DEHN, J., PEREGOVICH, B., THIEDE, J. (1999). Depositional environment of the Laptev Sea (Arctic Siberia) during the Holocene. Boreas 28. 194-204.

BAUCH, H.A., MUELLER-LUPP, T., TALDENKOVA, E., SPIELHAGEN, R.F., KASSENS, H., GROOTES, P.M., THIEDE, J., HEINEMEIER, J., PETRYASHOV, V.V. (2001). Chronology of the Holocene transgression at the North Siberian margin. Global and Planetary Change 31. 125-139.

BOUCHARD, M. (1974). Géologie des dépôts meubles de l'île Herschel, territoire du Yukon. M.Sc.(maitrise) Thesis. Université de Montréal. 70 pp.

BREZGUNOV, V.S., DEREVYAGIN, A.Y., CHIZHOV, A.B. (2001). Using natural stable Hydrogen and Oxygen isotope for studying the conditions of ground ice formation. Water Resources 28 (6). 604-608.

BRIGHAM-GRETTE, J., GUALTIERI, L.M., GLUSHKOVA, O.Y., HAMILTON, T.D., MOSTOLLER, D., KOTOV, A. (2003). Chlorine-36 and 14C chronology support a limited Last Glacial Maximum across central Chukotka, northeastern Siberia, and no Beringian ice sheet. Quaternary Research 59 (3). 386-398.

BROWN, R.J.E. (1970). Permafrost in Canada; its influence on northern development. University of Toronto Press. Toronto. 234p.

BURN, C.R. (1997). Cyostratigraphy, palaeography, and climate change during the early Holocene warm interval, western Arctic coast, Canada. Canadian Journal of Earth Sciences 34. 912-925.

BURN, C.R., MICHEL, F.A. (1988). Evidence for recent temperature-induced water migration into permafrost from the tritium content of ground ice near Mayo, Yukon Territory. Canadian Journal of Earth Sciences 25. 909-915.

BURN, C. R., MICHEL, F. A., SMITH, M. W. (1986). Stratigraphic, isotopic and mineralogical evidence for an early Holocene thaw unconformity at Mayo, Yukon Territory. Canadian Journal of Earth Sciences 23 (6). 794-803.

BUTLER, R. (1992). Paleomagnetism: Magnetic domains to geologic terranes. Cambridge.

CLARK, I.D., FRITZ, P. (1997). Environmental Isotopes in Hydrogeology. Lewis Publ., Boca Raton.

COUTURE, N.J. (2006). How changes in environmental forcing affects fluxes of soil organic carbon from eroding permafrost coasts, Canadian Beaufort Sea. unpublished Ph.D. Research Proposal. McGill University. Montreal. 52p.

COUTURE, N., POLLARD, W. (2007). Modelling geomorphic response to climatic change. Climatic Change 85. 407−431.

CRAIG, H. (1953). The geochemistry of the stable carbon isotopes. Geochimica et Cosmochimica Acta 3. 53-92.

CRAIG, H. (1961). Isotopic variations in meteoric waters. Science 133. 1702-1703.

CRAIG, H., GORDON, L. (1965). Deuterium and oxygen-18 variation in the ocean and the marine atmosphere. In: Tongiorgi, E. (Ed.). Stable Isotopes in Oceanographic Studies and Paleotemperatures. Spoleto. 9-130.

DANSGAARD, W. (1953). Comparative measurements of standards for carbon isotopes. Geochimica et Cosmochimica Acta 3. 253-256.

DANSGAARD, W. (1964). Stable isotopes in precipitation. Tellus 16. 436-469.

DANSGAARD, W., TAUBER, H. (1969). Glacier Oxygen-18 Content and Pleistocene Ocean Temperatures. Science 166 (3904). 499-502.

DE KROM, V. (1990). A geomorphic investigation of retrogressive thaw slumps and active layer detachment slides on Herschel Island, Yukon Territory. M.Sc. Thesis. McGill University. Montréal.

DEGENS, E. T. (1969). Biogeochemistry of Stable Carbon Isotopes. In: Eglinton, G., Murphy, M.T.J. (Eds.) (1969). Organic Geochemistry: Methods and Results. Springer. Berlin.

DEGENS, E.T. (1968). Geochemie der Sedimente. Stuttgart.

DEREVIAGIN, A.Y., MEYER, H., CHIZHOV, A.B., HUBBERTEN, H.-W., SIMONOV, E.F. (2002) New Data on the Isotopic Composition and Evolution of modern Ice wedges in the Laptev Sea Region. Polarforschung 70. 27-35.

DINTER, D.A., CARTER, D.L., BRIGHAM-GRETTE, J. (1990). Late Cenozoic geological evolution of the Alaskan North Slope and adjacent continental shelves. In: Grantz, A., Johnson, L., Sweeney, J.F. (Eds.). The Arctic Ocean Region. The Geology of North America v. L. Geological Society of America, Boulder, CO, pp. 459-490.

DUK-RODKIN, A., BARENDREGT, R. W., FROESE, D. G., WEBER, F., ENKIN, R., SMITH, I. , ZAZULA, G. D., WATERS, P., KLASSEN, R. (2004). Timing and extent of Plio-Pleistocene glaciations in north-western Canada and east-central Alaska. In: Ehlers, J., Gibbard, P.L. (Eds.). (2004). Quaternary Glaciations - Extent and Chronology, Part II: North America. Amsterdam.

DUK-RODKIN, A., BARENDREGT, R.W., TARNOCAI, C., PHILLIPS, F.M. (1996). Late Tertiary to Late Quaternary record in the Mackenzie Mountains, Northwest Territories, Canada: stratigraphy, paleomagnetism, and chlorine-36. Canadian Journal of Earth Sciences 33. 875-895.

DYKE, A.S., ANDREWS, J.T., CLARK, P.U., ENGLAND, J.H., MILLER, G.H., SHAW, J., VEILLETTE, J.J. (2002). The Laurentide and Innuitian ice sheets during the Last Glacial Maximum. Quaternary Science Reviews 21. 9-31.

DYKE, A.S., PREST, V.K. (1987). Late Wisconsinan and Holocene history of the Laurentide Ice Sheet. Géographie Physique et Quaternaire 41. 237-263.

EDWARDS, M.E., BRIGHAM-GRETTE, J. (1990). Climatic change and thawlake formation in Alaska. 11th Biennial Meeting of the American Quaternary Association, Waterloo. p. 17.

EISNER, W.R. (1991). Palynological analysis of a peat core from Imnavait Creek, the North Slope, Alaska. Arctic 44, 279-282.

EISNER, W.R. (1999). Climate change and spatial diversity of vegetation during the Late Quaternary of Beringia. Geographic Studies 252. University of Utrecht. 157 pp.

EISNER, W.R., BOCKHEIM, J.G., HINKEL, K.M., BROWN, T.A., NELSON, F.E., PETERSON, K.M., JONES, B.M. (2005). Paleoenvironmental analyses of an organic deposit from an erosional landscape remnant, Arctic Coastal Plain of Alaska. Palaeogeography, Palaeoclimatology, Palaeoecology 217 (3-4). 187-204.

ELIAS, S.A., SHORT, S.K., NELSON, C.H., BIRKS, H.H. (1996). Life and times of the Bering land bridge. Nature 382. 60–63.

ENGLAND, J., ATKINSON, N., BEDNARSKI, J., DYKE, A.S., HODGSON, D.A., O COFAIGH, C. (2006). The Innuitian Ice Sheet: configuration, dynamics and chronology. Quaternary Science Reviews 25 (7-8). 689.

EPSTEIN, S., MAYEDA, T. (1953). Variations of O18 content of waters from natural sources. Geochimica et Cosmochimica Acta 4. 213-224.

FRENCH, H.M. (1996). The Periglacial Environment. 2nd ed., Longman Publ., London.

FRENCH, H.M. (1998). An appraisal of cryostratigraphy in north-west Arctic Canada. Permafrost and Periglacial Processes 9 (4). 297-312.

FRENCH, H.M., HARRY, D.G. (1990). Observations on buried glacier ice and massive segregated ice, western Arctic coast, Canada. Permafrost and Periglacial Processes 1. 31-43.

FROHN, R.C., HINKEL, K.M., EISNER, W.R. (2005). Satellite remote sensing classification of thaw lakes and drained thaw lake basins on the North Slope of Alaska. Remote Sensing of Environment 97 (1). 116-126.

FÜCHTBAUER, H. (Ed.) (1988): Sedimente und Sedimentgesteine. Stuttgart.

FULTON, J.R. (Ed.) (1989). Quaternary geology of Canada and Greenland, Geology of Canada No.1. Geological Survey of Canada. Ottawa. 889 pp.

GAT, J.R. (1995). Stable Isotopes of Fresh and Saline Lakes. In: Lerman, A., Imboden, D., Gat, J.R. (Eds.). (1995). Physics and Chemistry of Lakes. Springer. Berlin. 139-165.

GAT, J.R. (1996). Oxygen and hydrogen isotopes in the hydrologic cycle. Annual Review of Earth and Planetary Sciences 1. 225-262.

GEOLOGICAL SURVEY OF CANADA (1981). Geology. Herschel Island and Demarcation Point, Yukon Territory. Series Maps, 1514A. Scale: 1:250,000.

GLASER, B. (2005). Compound-specific stable-isotope (δ^{13}C) analysis in soil science. Journal of Plant Nutrition and Soil Science 168 (5). 633-648.

GUALTIERI, L., VARTANYAN, S., BRIGHAM-GRETTE, J., ANDERSON, P.M. (2003). Pleistocene raised marine deposits on Wrangel Island, northeast Siberia and implications for the presence of an East Siberian ice sheet. Quaternary Research 59. 399-410.

HAMILTON, T.D. (1986). Late Cenozoic glaciation of the central Brooks Range. In: Hamilton, T.D., Reed, K.M., Thorson, R.M. (Eds.). Glaciation in Alaska: the Geologic Record. Alaska Geological Society, Anchorage. 9-49.

HAMILTON, T.D. (1994). Late Cenozoic glaciation of Alaska. In: Plafker, G., Berg, H.C. (Eds.), The Geology of Alaska. Geological Society of America, Boulder, 813-844.

HANDBOOK COULTER LS SERIE TEIL III (1993). Coulter Electronics GmbH. Krefeld.

HANDBOOK ELEMENTAR VARIO EL III (2001). Elementar Analysensysteme GmbH. Hanau.

HANDBOOK WTW (1989). pH-Fibel: Einführung in die pH- und Redox-Meßtechnik. Wiss.-techn. Werkstätten GmbH, Weilheim.

HANDBOOK WTW (1993). Leitfähigkeits-Fibel: Einführung in die Konduktometrie. Wiss.-techn. Werkstätten GmbH, Weilheim.

HARRIS, C., DAVIES, M.C.R. (1998). Pressures recorded during laboratory freezing and thawing of a natural silt-rich soil. In: Lewkowicz, A.G., Allard, M. (Eds.). Seventh International Permafrost Conference. Yellowknife, NWT, Canada, 23-27 June, 1998. Nordicana. 433-439.

HARRIS, S.A., FRENCH, H.M., HEGINBOTTOM, J.A., JOHNSTON, G.H., LANDANYI, D.C., SEGO, D.C., VAN EVERDINGEN, R.O. (1988). Glossary of Permafrost and Related Ground-Ice Terms. Permafrost Subcommittee, Associate Committee on Geotechnical Research, National Research Council Canada, Technical Memorandum No. 142. Ottawa. 156p.

HARRY, D.G., FRENCH, H.M., POLLARD, W.H. (1988). Massive ice and ice-cored terrain near Sabine Point, Yukon Coastal Plain. Canadian Journal of Earth Sciences 25. 1846-1856.

HENDL, M., LIEDTKE, H. (Eds.) (1997). Lehrbuch der Allgemeinen Physischen Geographie. Gotha.

HILL, P.R. (1990). Coastal geology of the King Point area, Yukon Territory, Canada. Marine Geology 91. 93-111.

HILL, P.R., BLASCO, S.M., HARPER, J.R., FISSEL, D.B. (1991). Sedimentation on the Canadian Beaufort Shelf. Continental Shelf Research 11 (8-10). 821-842.

HILTON, J. (1990). Greigite and the magnetic properties of sediments. Limnology and Oceanography 35 (2). 509-520.

HOEFS, J. (1997). Stable isotope geochemistry. 4th ed., Springer. Berlin.

HOLLERBACH, A. (1985). Grundlagen der organischen Geochemie. Springer. Berlin.

HÖLTING, B. (1996). Einführung in die allgemeine und angewandte Hydrogeologie. 5th ed., Enke. Stuttgart.

HOPKINS, D.L. (1982). Aspects of the paleogeography of Beringia during the Late Pleistocene. In: Hopkins, D.L., Matthews, Jr. J.V., Schweger, C.E., Young, S.B. (Eds.). Paleoecology of Beringia. Academic Press, New York, 3-28.

HORITA, J., UEDA, A., MIZUKAMI, K., TAKATORI, I. (1989). Automatic δD and $\delta 18O$ analyses of multi-water samples using H2- and CO2-water equilibration methods with a common equilibration set-up. International Journal of Radiation Applications and Instrumentation. Part A. Applied Radiation and Isotopes 40 (9). 801-805.

INMAN, D.L. (1952). Measures of describing the size distribution of sediments. Journal of Sedimentary Petrology 22. 125-145.

IPCC (2007). Climate Change 2007: The Physical Science Basis. Contribution of Working Group I to the Fourth Assessment Report of the Intergovernmental Panel on Climate Change. Cambridge University Press. Cambridge.

JEAN-BAPTISTE, P., JOUZEL, J., STIEVENARD, M., CIAIS, P. (1998). Experimental determination of the diffusion rate of deuterated water vapour in ice and application to the stable isotopes smoothing of ice cores. Earth and Planetary Science Letters 158 (1-2). 81-90.

JOUSSAUME, S., SADOURNY, R., JOUZEL, J. (1984). A general circulation model of water isotope cycles in the atmosphere. Nature 311 (5981). 24-29.

JOUZEL, J., ALLEY, R.B., CUFFEY, K.M., DANSGAARD, W., GROOTES, P., HOFFMANN, G., JOHNSEN, S.J., KOSTER, R.D., PEEL, D., SHUMAN, C.A., STIEVENARD, M., STUIVER, M., WHITE, J. (1997). Validity of the temperature reconstruction from water isotopes in ice cores. J. Geophys. Res. 102 (C12), 26471-26488.

JOUZEL, J., MERLIVAT, L., LORIUS, C. (1982). Deuterium excess in an East Antarctic ice core suggests higher relative humidity at the oceanic surface during the last glacial maximum. Nature 299 (5885). 688-691.

JOUZEL, J., STIEVENARD, M., JOHNSEN, S. J., LANDAIS, A., MASSON-DELMOTTE, V., SVEINBJORNSDOTTIR, A., VIMEUX, F., VON GRAFENSTEIN, U., WHITE, J. W. C. (2007). The GRIP deuterium-excess record. Quaternary Science Reviews 26 (1-2). 1-17.

KARTE, J. (1979): Räumliche Abgrenzung und regionale Differenzierung des Periglazials. Bochumer Geographische Arbeiten 35. Göttingen.

KAUFMAN, D.S., AGER, T.A., ANDERSON, N.J., ANDERSON, P.M., ANDREWS, J.T., BARTLEIN, P.J., BRUBAKER, L.B., COATS, L.L., CWYNAR, L.C., DUVALL, M.L., DYKE, A.S., EDWARDS, M. E., EISNER, W.R., GAJEWSKI, K., GEIRSDOTTIR, A., HU, F.S., JENNINGS, A.E., KAPLAN, M.R., KERWIN, M.W., LOZHKIN, A.V., MACDONALD, G.M., MILLER, G.H., MOCK, C.J., OSWALD, W.W., OTTO-BLIESNER, B.L., PORINCHU, D.F., RUHLAND, K., SMOL, J.P., STEIG, E.J., WOLFE, B.B. (2004). Holocene thermal maximum in the western Arctic (0-180°W). Quaternary Science Reviews 23. 529-560.

KNIGHT, P.G., PATTERSON, C.J., WALLER, R.I., JONES, A.P., ROBINSON, Z.P. (2000). Preservation of basal-ice sediment texture in ice-sheet moraines. Quaternary Science Reviews 19. 1255-1258.

KOKELJ, S.V., BURN, C.R. (2003). Ground ice and soluble cations in near-surface permafrost, Inuvik, Northwest Territories, Canada. Permafrost and Periglacial Processes 14 (3). 275-289.

KOKELJ, S.V., JENKINS, R.E., MILBURN, D., BURN, C.R., SNOW, N. (2005). The influence of thermokarst disturbance on the water quality of small upland lakes, Mackenzie Delta region, Northwest Territories, Canada. Permafrost and Periglacial Processes 16. 343-353.

KOKELJ, S.V., LEWKOWICZ, A.G. (1999). Salinization of Permafrost Terrain Due to Natural Geomorphic Disturbance, Fosheim Peninsula, Ellesmere Island. Arctic 52 (4). 372-385.

KOKELJ, S. V., SMITH, C. A. S., BURN, C. R. (2002). Physical and chemical characteristics of the active layer and permafrost, Herschel Island, western Arctic Coast, Canada. Permafrost and Periglacial Processes 13. 171-185.

KOTLER, E., BURN, C.R., (2000). Cryostratigraphy of the Klondike "muck" deposits, west-central Yukon Territory. Canadian Journal of Earth Sciences 37 (6). 849–861.

LACELLE, D., BJORNSON, J., LAURIOL, B., CLARK, I.D., TROUTET, Y. (2004). Segregated-intrusive ice of subglacial meltwater origin in retrogressive thaw flow headwalls, Richardson Mountains, NWT, Canada. Quaternary Science Reviews 23. 681-696.

LACELLE, D., LAURIOL, B., CLARK, I.D., CARDYN, R., ZDANOWICZ, CH. (2007). Nature and origin of a Pleistocene-age massive ground-ice body exposed in the Chapman Lake moraine complex, central Yukon Territory, Canada. Quaternary Research 68 (2). 249.

LACHENBRUCH, A.H. (1962). Mechanics of thermal contraction cracks and ice-wedge polygons in permafrost. Special Geol. Soc. of Am. Papers 70. New York. 69p.

LANTUIT, H. (2005). Mapping permafrost and ground ice related coastal erosion on Herschel Island, southern Beaufort Sea, Yukon Territory. M.Sc.Thesis. McGill University. Montréal. 135.

LANTUIT, H. (2008). The modification of arctic permafrost coastlines. Ph.D. thesis, University of Potsdam. 106 pp. Unpublished.

LANTUIT, H., POLLARD, W.H. (2005). Temporal stereophotogrammetric analysis of retrogressive thaw slumps on Herschel Island, Yukon Territory. Natural Hazards and Earth System Science 5. 413-423.

LANTUIT, H., POLLARD, W.H. (2008). Fifty years of coastal erosion and retrogressive thaw slump activity on Herschel Island, southern Beaufort Sea, Yukon Territory, Canada. Geomorphology 95. 84-102.

LEWIS, C.P. (1988). Mackenzie Delta Sedimentary Environments and Processes. Draft Contract Report. Environment Canada, Inland Waters Directorate: Ottawa. 395 pp.

LEWKOWICZ, A.G. (1987). Headwall retreat of ground-ice failures, Banks Island, Northwest Territories. Canadian Journal of Earth Sciences 24. 1077-1085.

LIBBY, W.F. (1952). Radiocarbon Dating. The University of Chicago Press. Chicago. 124p.

LORRAIN, R.D., DEMEUR, P. (1985). Isotopic evidence for relic Pleistocene glacier ice on Victoria Island, Canadian Arctic Archipelago. Arctic and Alpine Research 17 (1). 89-98.

LOZINSKI, W. (1909): Die Mechanische Verwitterung der Sandsteine im gemässigten Klima. Acad. Sci. Cracovie Bull. Inetrenat., Cl. Sci. Math. et Naturalles 1. 1-25.

MACKAY, J.R. (1959). Glacier ice-thrust features of the Yukon Coast. Geographical Bulletin 13. 5-21.

MACKAY, J.R. (1966). Segregated epigenetic ice and failures in permafrost, Mackenzie delta area, N.W.T. Geographical Bulletin 8. 59-80.

MACKAY, J.R. (1971). The origin of massive icy beds in permafrost, western arctic coast, Canada. Canadian Journal of Earth Sciences 8 (4). 397-422.

MACKAY, J.R. (1972a). Offshore permafrost and ground ice, southern Beaufort Sea, Canada. Canadian Journal of Earth Sciences 9. 1550-1561.

MACKAY, J.R. (1972b). The world of underground ice. Annals of the Association of American Geographers 62. 1-22.

MACKAY, J.R. (1973). Problems in the roigin of massive ice beds, western Arctic, Canada. In: Permafrost: North American contribution to the second international conference. Yakutsk. U.S.S.R. National Academy of Sciences. Wahington D.C. Publication 2115. 223-228.

MACKAY, J.R. (1974). Ice wedge cracks, Garry Island, NWT. Canadian Journal of Earth Sciences 11, 1366-1383.

MACKAY, J.R. (1975). The stability of permafrost and recent climatic change in the Mackenzie valley, N.W.T. Current Research (Paper 75-1B). 173-176.

MACKAY, J.R. (1978). Quaternary and permafrost features, Mackenzie delta area. In: Young, F.G. (Ed.). Geological and geographical guide to the Mackenzie delta area. Can. Society Petroleum Geologists. 42-50.

MACKAY, J.R. (1979). The use of snow fences to reduce ice-wedge cracking, Garry Island, Northwest Territories. Current Research, Part A, Paper 78-1A. Geol. Surv. Canada. 523-524.

MACKAY, J.R. (1983). Oxygen isotope variations in Permafrost, Tuktoyaktuk penisnula area, Northwest Territories. Current Research Part B (Paper 83-1B). 67-74.

MACKAY, J.R. (1989). Massive ice: some field criteria for the identification of ice types. Current Research Part G (Paper 89-1G). 5-11.

MACKAY, J.R. (1990). Some Observations on the Growth and Deformation of Epigenetic, Syngenetic and Anti-Syngenetic Ice wedges. Permafrost and Periglacial Processes 1. 15-29.

MACKAY, J.R. (1992). The frequency of ice-wedge cracking (1967-1987) at Garry Island, western Arctic coast, Canada. Canadian Journal of Earth Sciences 29. 236-248.

MACKAY, J.R. (2000). Thermally induced movements in ice-wedge polygons, Western Arctic Coast: A long-term study. Géographie physique et Quaternaire 54 (1). 41-68.

MACKAY, J.R., DALLIMORE, S.R. (1992). Massive ice of the Tuktoyaktuk area, western Arctic coast, Canada. Canadian Journal of Earth Sciences 29. 1235-1249.

MANGERUD, J., ASTAKHOV, V., SVENDSEN, J.-I. (2002). The extent of the Barents-Kara ice sheet during the Last Glacial Maximum. Quaternary Science Reviews 21 (1-3). 111-119.

MATTHEWS, J.V. JR. (1975). Incongruence of macrofossils and pollen evidence: a case from the late Pleistocene of the northern Yukon Coast. Report of Activities, Part B, Geological Survey of Canada Paper 75-1B. 139-146.

MCDONALD, B.C., LEWIS, C.P. (1973). Geomorphologic and Sedimentologic Processes of Rivers and Coast, Yukon Coastal Plain. Environmental-Social Committee, Northern Pipelines, Canada. Rept. No. 73-39, 245 pp.

MERLIVAT, L., JOUZEL, J. (1979). Global climatic interpretation of the deuterium-oxygen 18 relationship for precipitation. Journal Geophysical Research 84 (C8). 5029-5033.

MERLIVAT, L., JOUZEL, J. (1983). Deuterium and 18O in precipitation: A global model from oceans to ice caps. In: n.n.: Palaeoclimates and palaeowaters; a collection of environmental isotope studies. Int. At. Energy Agency, Vienna. 65-66

METEOROLOGICAL SERVICE OF CANADA. (2006). http://climate.weatheroffice.ec.gc.ca/, visited: 13.11.2007.

MEYER, H., SCHÖNICKE, L., WAND, U., HUBBERTEN, H.-W., FRIEDRICHSEN, H. (2000). Isotope studies of hydrogen and oxygen in ground ice – Experiences with the equilibration technique. Isotopes in Environmental and Health Studies 36. 133-149.

MEYER, H., DEREVIAGIN, A.Y., SIEGERT, C., HUBBERTEN, H.-W. (2002a). Paleoclimate studies on Bykovsky Peninsula, North Siberia - hydrogen and oxygen isotopes in ground ice. Polarforschung 70. 37-51.

MEYER, H., DEREVIAGIN, A.Y., SIEGERT, C., SCHIRRMEISTER, L., HUBBERTEN, H.-W. (2002b). Paleoclimate reconstruction on Big Lyakhovsky Island, North Siberia– hydrogen and oxygen isotopes in ice wedges. Permafrost and Periglacial Processes 13. 91-105.

MEYERS, P.A. (1994). Preservation of elemental and isotopic source identification of sedimentary organic matter. Chemical Geology 114 (3-4). 289-300.

MEYERS, P.A. (1997). Organic geochemical proxies of paleoceanographic, paleolimnologic, and paleoclimatic processes. Organic Geochemistry 27 (5-6). 213-250.

MEYERS, P.A., ISHIWATARI, R. (1993). Lacustrine organic geochemistry − an overview of indicators of organic matter sources and diagenesis in lake sediments. Organic Geochemistry 20 (7). 867-900.

MEYERS, P.A., LALLIER-VERGES, E. (1999). Lacustrine sedimentary organic matter records of Late Quaternary paleoclimates. Journal of Paleolimnology 21 (3). 345-372.

MICHEL, F.A. (1982). Isotope investigations of permafrost waters in Northern Canada. PhD thesis, Dept. of Earth Sciences, Univ. of Waterloo, Canada.

MOORMAN, B.J., MICHEL, F.A., WILSON, A. (1996). 14C dating of trapped gases in massive ground ice, western Canadian Arctic. Permafrost and Periglacial Processes 7. 257-266.

MURTON, J.B. (1993). Thaw modification of frost-fissure wedges, Richards Island, Pleistocene Mackenzie Delta, western Arctic Canada. Journal of Quaternary Science 8 (3). 185-196.

MURTON, J.B. (2005). Ground-ice stratigraphy and formation at North Head, Tuktoyaktuk Coastlands, western Arctic Canada: a product of glacier-permafrost interactions. Permafrost and Periglacial Processes 16 (1). 31-50.

MURTON, J.B., FRENCH, H.M. (1994). Cryostructures in permafrost, Tuktoyaktuk Coastlands, western Arctic Canada. Canadian Journal of Earth Sciences 31. 737-747.

MURTON, J.B., WALLER, R.I., HART, J.K., WHITEMAN, C.A., POLLARD, W.H., CLARK, I.D. (2004). Stratigraphy and glaciotectonic structures of permafrost deformed beneath the northwest margin of the Laurentide ice sheet, Tuktoyaktuk Coastlands, Canada. Journal of Glaciology 50. 399-412.

MURTON, J.B., WHITEMAN, C.A., WALLER, R.I., POLLARD, W.H., CLARK, I.D., DALLIMORE, S.R. (2005). Basal ice facies and supraglacial melt-out till of the Laurentide Ice Sheet, Tuktoyaktuk Coastlands, western Arctic Canada. Quaternary Science Reviews 24, 681-708.

OECHEL, W.C., HASTINGS, S.J., VOURLRTIS, G., JENKINS, M., RIECHERS, G., RULKE, N. (1993). Recent change of Arctic tundra ecosystems from a net carbon dioxide sink to a source. Nature 361. 520-523.

OPERATION MANUAL BARTINGTON MS2 (1990). Bartington Instr. Ltd. Witney.

PELTIER, W. R. (2002). On eustatic sea level history: Last Glacial Maximum to Holocene. Quaternary Science Reviews 21 (1-3). 377-396.

POLLARD, W.H. (1990). The nature and origin of ground ice in the Herschel Island area, Yukon Territory. 5th Canadian Permafrost Conference. Québec. Nordicana. 23-30.

POLLARD, W. H. (1998). Arctic Permafrost and Ground Ice. In: Weatherhead, E., Morseth, C.M. (Eds.) Chapter 11: Climate Change, Ozone and ultraviolet Radiation. Arctic Monitoring and Assessment Program Report.

POLLARD, W.H., DALLIMORE, S.W. (1988). Petrographic characteristics of massive ground ice, Yukon Coastal Plain, Canada Proceedings, 5th International Conference on Permafrost. Trondheim, Norway, August 1988. Tapir. Trondheim. 224-229.

RACHOLD, V., EICKEN, H., GORDEEV, V.V., GRIGORIEV, M.N., HUBBERTEN, H.-W., LISITZIN, A.P., SHEGCHENKO, V.P., SCHIRRMEISTER, L. (2004). Modern terrigenous organic carbon input to the arctic Ocean. In: Stein, R., Macdonald, R.W. (Eds.) Organic Carbon Cycle in the arctic Ocean: Present and Past. Springer. Berlin.

RAMPTON, V.N. (1982). Quaternary geology of the Yukon Coastal Plain. Geological Survey of Canada. Bulletin 317. 49p.

RAMPTON, V.N. (1988). Quaternary geology of the Tuktoyaktuk coastlands, Northwest Territories. Geological Survey of Canada. Memoir 423.

REIMNITZ, E., WOLF, C. (1998). Are North Slope Surface Alluvial Fans Pre-Holocene Relicts?. U.S. Geological Survey. Professional Paper 1605. 9p.

RITCHIE, J.C. (1984). Past and Present Vegetation of the Far Northwest of Canada. University of Toronto Press, Toronto. 251 pp.

RITCHIE, J.C., CWYNAR, L.C., SPEAR, R.W. (1983). Evidence from north-west Canada for an early Holocene Milankovitch thermal maximum. Nature 305. 126-128.

ROMANOVSKY, N.N. (1976). The scheme of correlation of polygonal wedge structures. Biuletyn Periglacjalny 26, 287-294.

SCHEFFER, F., SCHACHTSCHABEL, P. (2002). Lehrbuch der Bodenkunde. 15th ed., Spektrum, Heidelberg.

SHEPARD, F.P. (1954). Nomenclature based on sand-silt-clay ratios. Journal of Sedimentary Research 24. 151-158.

SCHIRRMEISTER, L., KUNITSKY, V.V., GROSSE, G., SCHWAMBORN, G., ANDREEV, A.A., MEYER, H., KUZNETSOVA, T., BOBROV, A., OEZEN, D. (2003): Late Quaternary history of the accumulation plain north of the Chekanovsky Ridge (Lena Delta, Russia): A multidisciplinary approach. Polar Geography 27 (4). 277-319.

SCHWAMBORN, G., MEYER, H., FEDOROV, G., SCHIRRMEISTER, L., HUBBERTEN, H.-W. (2006). Ground ice and slope sediments archiving late Quaternary paleoenvironment and paleoclimate signals at the margins of El'gygytgyn Impact Crater, NE Siberia. Quaternary Research 66 (2). 259-272.

SHUR, Y.L., JORGENSON, M.T. (1998). Cryostructure development on the floodplain of the Colville River Delta, northern Alaska. In: Lewkowicz, A.G., Allard, M. (Eds.). Seventh International Permafrost Conference. Yellowknife, NWT, Canada, 23-27 June, 1998. Nordicana 57. 993-999.

SIEGERT, CH. (1987). Greigit und Mackinawit in quartären Permafrost-Ablagerungen Zentral-Jakutiens. Mineralogisches Journal. Kiev. Vol. 9. No 5. 75-81 (in Russian).

SMITH, C.A.S., KENNEDY, C.E., HARGRAVE, A.E., MCKENNA, K.M. (1989). Soil and vegetation of Herschel Island, Yukon Territory. Yukon Soil Survey Report No. 1. Land Resource Research Centre, Agriculture Canada: Ottawa.

SOUCHEZ, R.A., JOUZEL, J. (1984). On the isotopic composition in δD and δ^{18}O of water and ice during freezing. Journal of Glaciology 30 (106). 369-372.

SOUCHEZ, R., JOUZEL, J., LORRAIN, R., SLEEWAEGEN, S., STIÉVENARD M., VERBEKE, V. (2000). A Kinetic Isotope Effect During Ice Formation by Water Freezing. Geophys. Res. Lett. 27(13). 1923-1926.

STUIVER, M, REIMER, P.J. (1993). Extended ^{14}C Data Base And Revised Calib 3.0 ^{14}C Age Calibration Program. Radiocarbon 35. 215-230.

SVENDSEN, J.I., ASTAKHOV, V.I., BOLSHIYANOV, D.Y., DEMIDOV, I., DOWDESWELL, J.A., GATAULLIN, V., HJORT, C., HUBBERTEN, H.W., LARSEN, E., MANGERUD, J., MELLES, M., MÖLLER, P., SAARNISTO, M., SIEGERT, M.J. (1999). Maximum extent of the Eurasian ice sheets in the Barents and Kara Sea region during the Weichselian. Boreas 28 (1). 234-242.

TAUXE, L. (1998). Paleomagnetic Principles and Practice. Kluwer Academic Publ.

TUCKER, M.E. (1991). Sedimentary petrology. Blackwell Scientific Publications. Oxford. 260 pp.

VAIKMÄE, R. (1989). Oxygen isotopes in permafrost and in ground ice - A new tool for paleoclimatic investigations. 5th Working Meeting Isotopes in Nature. Leipzig, September 1989. 543-551.

VAIKMÄE, R. (1991). Oxygen-18 in Permafrost Ice. International Symposium of the Use of Isotope Techniques in Water Resources Development, 11-15 March 1991. Vienna.

VAN EVERDINGEN, R.O. (Ed.) (1998). Multi-language glossary of permafrost and related ground-ice terms. National Snow and Ice Data Center/World Data Center for Glaciology. Boulder.

VASIL'CHUK, Y.K. (1991). Reconstruction of the paleoclimate of the late Pleistocene and Holocene on the basis of isotope studies of subsurface ice and waters of the permafrost zone. Water Resources 17 (6). 640-674.

VASIL'CHUK, Y.K., VASIL'CHUK, A.C. (1997). Radiocarbon Dating and Oxygen Isotope Variations in Late Pleistocene Syngenetic Ice-Wedges, Northern Siberia. Permafrost and Periglacial Processes 8 (3). 335-345.

VASIL'CHUK, Y.K., VAN DER PLICHT, J., JUNGNER, H., VASIL'CHUK, A.C. (2000a). AMS-dating of Late Pleistocene and Holocene syngenetic ice-wedges. Nuclear Instruments and Methods in Physics Research Section B: Beam Interactions with Materials and Atoms 172. 637-641.

VASIL'CHUK, Y.K., VAN DER PLICHT, J., JUNGNER, H., SOININEN, E., VASIL'CHUK, A.C. (2000b). First direct dating of Late Pleistocene ice-wedges by AMS. Earth and Planetary Science Letters 179. 237-242.

WAGNER, G.A. (1995). Altersbestimmung von jungen Gesteinen und Artefakten. Enke. Stuttgart.

WALTHERT, L., ZIMMERMANN, S., BLASER, P., LÜSCHER, P., LUSTER, J. (2004-2006). Waldböden der Schweiz. Eidg. Forschungsanstalt WSL und hep Verlag. Vol.1-3.

WASHBURN, A.L. (1979). Geocryology. A survey of periglacial processes and environment. 2nd ed. London.

WASHBURN, A.L. (1980). Permafrost Features as Evidence of Climatic Change. Earth-Science Reviews 15. 327-402.

WEISE, O.R. (1983). Das Periglazial. Berlin.

WIGLEY, T.M.L. (Ed.) (2000). The carbon cycle. Cambridge.

WILLKOMM, H. (1976). Altersbestimmungen im Quartär: Datierungen mit Radiokohlen-stoff und anderen kernphysikalischen Methoden. Thiemig. München.

WOLFE, S.A., KOTLER, E., DALLIMORE, S.R. (2001). Surficial characteristics and the distribution of thaw landforms (1970 to 1999), Shingle Point to Kay Point, Yukon Territory. Open File 4088. Geological Survey of Canada.

ZDANOWICZ, CH.M., FISHER, D.A., CLARK, I., LACELLE, D. (2002). An ice-marginal 18O record from Barnes Ice Cap, Baffin Island, Canada. Annals of Glaciology 35. 145-149.

8 APPENDIX

This chapter serves as data base for all the analytical results on both sediment and ground ice or recent water samples. It is divided into the following:

Appendix 1

Overview over results for the analyses performed on sediment samples and texture ice within, p.124.

Appendix 2

Radiocarbon dates for organic matter from sediment samples, p. 128.

Appendix 3

Results for stable isotope analyses (δ^{18}O and δD, together with d-excess) on ground ice samples and recent water samples, p. 129.

Appendix 1: Overview over results for the analyses performed on sediment samples and texture ice within. Sorting is according to Inman (1952). The gravimetric ice content and δ¹⁸O values were not determined for every sample.

Sample	Profile	Depth below surface	TC	TOC	TN	C/N-ratio	Magnetic Susceptibility	Ice content	Conductivity	pH	δ¹³C	Clay	Silt	Sand	Gravel	Mean	Median	δ¹⁸O	Sorting (Inman)	Sorting Classification
		[m]	[wt %]	[wt %]	[wt %]		SI [10-8 m³/kg]	[wt %]	[µS/cm]		[‰]	[%]	[%]	[%]	[%]	[µm]	[µm]	[‰]		
Col 1/1		2.4	2.7	1.6	0.1	13	16	53	607	7.6	-26.0	25.0	63.0	12.0	0.0	12	8	-22.9	2.6	very poorly sorted
Col 1/2		2.2	2.6	1.5	0.1	12	20	42	804	7.6	-26.2	30.0	65.0	5.0	0.0	8	5	-22.7	2.2	very poorly sorted
Col 1/3		1.9	2.4	1.3	0.1	11	16	46	716	7.7	-26.0	33.0	55.0	12.0	0.0	9	5		2.6	very poorly sorted
Col 1/4		1.6	2.4	1.3	0.1	12	18		429	7.7	-26.1	21.0	57.0	22.0	0.0	25	11	-20.7	3.3	very poorly sorted
Col 1/5		1.4	2.2	1.1	0.1	12	17	28	494	7.7	-26.1	30.0	61.0	9.0	0.0	10	6		2.6	very poorly sorted
Col 1/6	COL 1	1.2	2.0	1.2	0.1	12	16		365	7.7	-26.0	30.0	60.0	10.0	0.0	11	6	-19.2	2.6	very poorly sorted
Col 1/7		0.9	12.2	12.1	0.8	16	23	137	490	6.8	-26.6	26.2	60.6	4.3	8.9	9	6	-18.6	2.6	very poorly sorted
Col 1/8		0.6	9.0	8.3	0.6	14	16	365	388	6.6	-26.4	25.0	67.0	8.0	0.0	10	6	-18.2	2.4	very poorly sorted
Col 1/9		0.4	11.4	10.5	0.8	14	15		280	5.0	-26.8	24.0	62.0	14.0	0.0	13	6	-17.2	2.8	very poorly sorted
Col 1/10		0.2	5.8	4.9	0.4	12	12		354	5.3	-26.7	31.0	54.0	15.0	0.0	14	5		3.0	very poorly sorted
Col 2/1		3.5	2.2	1.5	0.1	15	23	57	2513	7.2	-26.3	25.6	53.2	19.8	1.4	24	8	-27.5	3.3	very poorly sorted
Col 2/2		3.2	2.6	1.4	0.1	13	31		1910	7.5	-26.3	23.6	52.0	19.0	5.4	30	9	-27.1	3.5	very poorly sorted
Col 2/3		3.0	2.6	1.5	0.1	13	35		2029	7.3	-26.3	24.9	50.8	24.2	0.0	30	9	-26.8	3.4	very poorly sorted
Col 2/4		2.8	2.5	1.5	0.1	12	32	90	2314	7.3	-26.3	26.0	53.0	21.0	0.0	23	8	-26.8	3.3	very poorly sorted
Col 2/5		2.5	2.6	1.4	0.1	13	36		2139	7.2	-26.4	24.1	51.2	21.3	3.4	32	9	-26.6	3.5	very poorly sorted
Col 2/6	COL 2_1	2.2	2.7	1.4	0.1	12	38	122	1899	7.3	-26.3	26.0	53.0	21.0	0.0	20	6	-26.9	3.3	very poorly sorted
Col 2/7		1.8	2.6	1.4	0.1	13	35		1557	7.2	-26.3	20.0	57.0	23.0	0.0	29	14	-26.7	3.2	very poorly sorted
Col 2/8		1.5	2.5	1.4	0.1	12	26	96	2188	7.2	-26.2	32.0	55.9	12.1	0.0	9	5	-26.8	2.6	very poorly sorted
Col 2/9		1.3	2.5	1.5	0.1	13	26	48	2383	7.2	-26.2	28.0	58.0	14.0	0.0	11	6		2.8	very poorly sorted
Col 2/10		0.9	3.0	2.1	0.2	13	20	29	1578	7.1	-26.1	21.8	53.4	24.8	0.0	32	10		3.5	very poorly sorted
Col 2/11		0.6	2.5	1.6	0.1	12	19		866	7.4	-26.2	26.8	50.7	22.5	0.0	27	8		3.4	very poorly sorted

Sample	Profile	Depth below surface [m]	TC [wt %]	TOC [wt %]	TN [wt %]	C/N-ratio	Magnetic Susceptibility SI [10-8 m³/kg]	Ice content [wt %]	Conductivity [µS/cm]	pH	δ^{13}C [‰]	Clay [%]	Silt [%]	Sand [%]	Gravel [%]	Mean [µm]	Median [µm]	δ^{18}O [‰]	Sorting (Inman)	Sorting Classification
Col 2/12		3.0	2.3	1.3	0.1	11	19	85	3720	7.4	-26.0	33.0	62.0	5.0	0.0	7	4	-27.5	2.2	very poorly sorted
Col 2/13		2.7	2.4	1.4	0.1	11	20		3770	7.4	-26.0	27.0	65.0	8.0	0.0	8	5	-27.2	2.4	very poorly sorted
Col 2/14		2.3	2.5	1.4	0.1	12	20	81	3010	7.3	-26.2	25.0	67.0	8.0	0.0	8	6	-27.0	2.3	very poorly sorted
Col 2/15	COL 2_2	2.0	2.9	2.1	0.2	13	18	35	1729	7.2	-26.6	26.0	64.0	10.0	0.0	10	6		2.5	very poorly sorted
Col 2/16		1.5	2.4	1.5	0.1	11	21	26	2045	7.2	-26.3	24.0	68.0	8.0	0.0	10	6		2.4	very poorly sorted
Col 2/17		1.1	2.9	2.1	0.2	13	16	29	2086	7.2	-26.3	22.0	66.0	12.0	0.0	13	8		2.6	very poorly sorted
Col 2/18		0.9	2.2	1.5	0.1	12	15	29	854	7.4	-25.9	23.0	65.0	12.0	0.0	12	7		2.6	very poorly sorted
Col 2/19		0.5	2.3	1.5	0.1	13	16		305	7.4	-26.1	24.0	65.0	11.0	0.0	11	6		2.5	very poorly sorted
Col 2/27			2.3	1.0	0.1	9	21		5510	7.8	-26.3	38.0	45.0	17.0	0.0	69	4		3.1	very poorly sorted
Col 2/26			1.3	0.6	0.1	8	21		11500	7.9	-25.8	24.5	36.2	39.3	0.0	13	21		3.7	very poorly sorted
Col 2/20		5.8	2.4	1.3	0.1	12	22	125	2633	7.4	-25.9	20.0	56.0	24.0	0.0	31	12	-28.8	3.3	very poorly sorted
Col 2/21	COL 2_3	5.2	2.3	1.4	0.1	12	22		2454	7.4	-26.2	26.6	50.2	21.9	1.3	28	8	-28.0	3.5	very poorly sorted
Col 2/22		4.4	2.5	1.3	0.1	12	22	76	1625	7.3	-26.2	24.0	57.0	19.0	0.0	20	10	-27.9	3.2	very poorly sorted
Col 2/23		3.9	2.4	1.2	0.1	11	19		2254	7.4	-26.0	25.0	49.0	26.0	0.0	35	10	-26.9	3.5	very poorly sorted
Col 2/24		3.3	2.4	1.3	0.1	11	21		2646	7.4	-26.1	29.0	50.0	21.0	0.0	23	7	-26.8	3.3	very poorly sorted
Col 2/25		2.9	2.5	1.6	0.1	13	22	60	2604	7.2	-26.2	25.0	52.0	23.0	0.0	26	8	-27.0	3.4	very poorly sorted

Sample	Profile	Depth below surface	TC	TOC	TN	C/N-ratio	Magnetic Susceptibility	Ice content	Conductivity	pH	$\delta^{13}C$	Clay	Silt	Sand	Gravel	Mean	Median	$\delta^{18}O$	Sorting (Inman)	Sorting Classification
		[m]	[wt %]	[wt %]	[wt %]		SI [10-8 m³/kg]	[wt %]	[µS/cm]		[‰]	[%]	[%]	[%]	[%]	[µm]	[µm]	[‰]		
Kom-1/1		4.3	2.4	0.8	0.1	9	26		1497	7.8	-25.6	16.0	70.0	14.0	0.0	24	19		2.4	very poorly sorted
Kom-1/2		4.1	2.1	0.5	0.1	8	25	66	702	7.7	-26.2	9.0	61.0	30.0	0.0	45	38	-23.3	2.1	very poorly sorted
Kom-1/3		3.8	4.2	3.1	0.3	12	15		3170	7.5	-26.8	13.0	68.0	19.0	0.0	27	19		2.3	very poorly sorted
Kom-1/4		3.5	2.6	0.9	0.1	9	17	37	1652	7.5	-26.2	18.0	69.0	13.0	0.0	20	14	-22.9	2.6	very poorly sorted
Kom-1/5		3.1	5.7	4.6	0.3	14	16		1838	7.0	-27.2	10.0	60.0	30.0	0.0	46	26	-22.3	2.6	very poorly sorted
Kom-1/6		2.8	3.1	1.8	0.2	8	14	50	1150	7.4	-26.7	15.0	69.0	16.0	0.0	24	17	-21.1	2.4	very poorly sorted
Kom-1/7		2.5	27.6	30.7	1.5	20	111	251	3479 *	6.0	-27.3	10.0	57.0	33.0	0.0	93	22	-19.6	3.5	very poorly sorted
Kom-1/8	KOM	2.2	40.8	45.8	2.4	19	28		504 *	5.9	-27.6	5.7	25.0	69.4	0.0	674	718		3.7	very poorly sorted
Kom-1/9		1.9	13.6	13.9	0.7	20	16	536	598 *	6.3	-27.6	15.0	59.0	26.0	0.0	37	16	-16.7	3.4	very poorly sorted
Kom-1/10		1.7	40.8	45.6	2.5	18	24		933 *	5.6	-27.5	5.0	40.0	55.0	0.0	238	89		2.9	very poorly sorted
Kom-1/11		1.4	11.6	11.3	0.6	19	13		325 *	5.9	-27.7	21.0	66.0	13.0	0.0	15	8	-15.5	2.6	very poorly sorted
Kom-1/12		1.1	18.0	17.9	0.9	19	25		198 *	5.7	-27.0	14.0	64.0	22.0	0.0	27	16	-14.7	2.7	very poorly sorted
Kom-1/13		0.8	20.3	20.3	1.3	16	16	173	321 *	5.3	-28.1	9.0	65.0	26.0	0.0	38	21	-14.0	2.6	very poorly sorted
Kom-1/14		0.5	31.8	32.2	1.9	17	33		312 *	4.7	-28.1	6.0	51.0	43.0	0.0	108	45		2.6	very poorly sorted
Kom-1/15		0.3	35.3	37.0	2.1	17	22		382 *	4.7	-28.6	14.0	74.0	12.0	0.0	17	14		2.1	very poorly sorted
Kom-1/16		0.0	37.2	38.8	2.1	19	21		1307 *	4.7	-28.7	5.0	39.0	56.0	0.0	239	104		3.0	very poorly sorted
TSD-1/2		1.0	2.0	1.7	0.1	13	16	42	2801	7.1	-26.1	18.0	49.0	33.0	0.0	51	21	-23.0	3.3	very poorly sorted
TSD-1/3		1.0	1.9	1.5	0.1	13	18	0	2071	7.1	-26.3	21.0	50.0	29.0	0.0	43	14	-23.8	3.4	very poorly sorted
TSD-1/4	TSD 1	1.0	2.6	1.5	0.1	12	34	51	3530	7.0	-26.7	29.0	50.0	21.0	0.0	23	6	-24.0	3.3	very poorly sorted
TSD-1/5		1.0	2.5	1.3	0.1	11	23	146	1865	7.3	-26.1	23.0	52.0	25.0	0.0	33	12	-24.6	3.4	very poorly sorted
TSD-1/6		1.0	2.6	1.3	0.1	12	23	0	1513	7.3	-26.2	23.0	54.0	23.0	0.0	28	11	-27.6	3.4	very poorly sorted

Sample	Profile	Depth below surface	TC	TOC	TN	C/N-ratio	Magnetic Susceptibility	Ice content	Conductivity	pH	$\delta^{13}C$	Clay	Silt	Sand	Gravel	Mean	Median	$\delta^{18}O$	Sorting (Inman)	Sorting Classification
		[m]	[wt %]	[wt %]	[wt %]		SI [10-8 m³/kg]	[wt %]	[µS/cm]		[‰]	[%]	[%]	[%]	[%]	[µm]	[µm]	[‰]		
TSD-2/1		3.0	2.3	2.0	0.1	14	15	0	454	6.9	-26.3	31.0	55.0	14.0	0.0	13	6	-20.1	2.9	very poorly sorted
TSD-2/2		2.5	4.2	4.0	0.3	16	15	0	362	6.0	-26.4	31.4	51.7	9.5	7.4	12	5	-20.1	3.1	very poorly sorted
TSD-2/3		2.1	2.4	2.1	0.2	14	15	84	168	6.4	-26.3	35.0	51.0	14.0	0.0	12	5	-19.7	2.9	very poorly sorted
TSD-2/4		1.9	13.9	13.2	0.6	23	19	0	566 *	5.4	-26.4	25.0	63.0	12.0	0.0	12	6	-19.0	2.6	very poorly sorted
TSD-2/5	TSD 2	1.6	14.7	14.1	0.8	17	16	310	524	5.2	-27.6	18.0	61.0	21.0	0.0	26	12	-19.2	2.9	very poorly sorted
TSD-2/6		1.3	17.0	16.4	0.9	18	17	0	495	5.0	-26.9	17.0	60.0	23.0	0.0	29	14	-19.1	2.9	very poorly sorted
TSD-2/7		1.1	10.9	9.9	0.5	18	17	0	390	4.6	-27.1	22.0	63.0	15.0	0.0	17	9	-18.7	2.9	very poorly sorted
TSD-2/8		0.9	12.1	11.2	0.7	16	13	0	342	4.8	-27.4	19.0	59.0	22.0	0.0	28	12		3.0	very poorly sorted
TSD-2/9		0.8	14.9	13.6	1.0	13	22	0	380 *	4.6	-26.8	27.9	57.7	14.4	0.0	11	6	-19.0	2.9	very poorly sorted
TSD-2/10		0.5	18.2	17.5	1.1	15	16	0	375	4.6	-26.7	11.0	43.0	46.0	0.0	100	49		3.2	very poorly sorted
TSD 3/1		3.2	2.2	1.2	0.1	12	23	0	1097	7.2	-26.0	25.5	56.6	15.8	2.1	14	6	-29.0	3.2	very poorly sorted
TSD 3/2	TSD 3	2.7	2.2	1.2	0.1	12	23	0	1106	7.2	-26.1	27.0	60.0	13.0	0.0	10	5	-27.6	2.7	very poorly sorted
TSD 3/3		2.3	2.3	1.3	0.1	11	24	0	1275	7.2	-26.2	27.0	67.0	6.0	0.0	7	5	-25.7	2.2	very poorly sorted
TSD 3/4		1.8	2.2	1.2	0.1	11	30	0	1353	6.9	-25.8	25.0	67.0	8.0	0.0	11	6	-23.7	2.5	very poorly sorted
TSD-SP-2/1		2.8	6.7	5.8	0.5	13	14	0	280 *	5.8	-27.4	22.0	63.9	14.2	0.0	15	8		2.8	very poorly sorted
TSD-SP-2/3	TSD-SP	1.8	13.1	11.3	0.9	13	16	0	386 *	5.6	-26.9	15.0	59.0	26.0	0.0	36	18		2.8	very poorly sorted
TSD-SP-2/2		0.8	18.2	17.3	1.1	15	15	0	408 *	5.4	-27.2	9.0	42.0	49.0	0.0	102	59		3.0	very poorly sorted

*) Values of electrical conductivity with grey background were re-calculated due to difficulties during measurement (see ch. 3.2.2.2).

Appendix 2:   Radiocarbon dates for organic matter from sediment samples. Additionally, sample ID and sample depth below surface (b.s.) are given.

Sample	Depth	Radiocarbon age			
	[m] b.s.	[^{14}C years BP]	**+**	**—**	[calibrated years BP]
Col 1/1	2.4	12,720	90	90	15,342 - 14,646
Col 1/5	1.4	27,190	340	320	—
Col 1/8	0.6	7485	40	40	8384 - 8276
Col 2/1	3.5	50,770	3800	2570	
Col 2/10	0.9	1110	35	35	1082 - 932
Col 2/14	2.3	>1954 A.D.*			—
Col 2/17	1.1	625	35	35	660 - 550
Kom-1/1	4.3	48,400	3270	2320	—
Kom-1/7	2.5	8405	45	45	9521 - 9372
Kom-1/15	0.3	2637	31	31	2792 - 2725
TSD-2/1	3.0	10,190	50	50	12,076 - 11,702
TSD-2/9	0.8	2290	30	30	2354 - 2300

* likely contaminated material

Appendix 3: Results for stable isotope analyses ($\delta^{18}O$ and δD, together with d-excess) on ground ice samples and recent water samples. Additionally, sample ID, study site and type of sample are given.

Sample	Study site	Sample type	$\delta^{18}O$ [‰ vs. VSMOW]	δD [‰ vs. VSMOW]	d-excess [‰]
HI-IW-1.13		Ice wedge	-20.96	-158.8	8.9
HI-IW-1.14		Ice wedge	-20.23	-154.4	7.5
HI-IW-1.15		Ice wedge	-20.92	-159.6	7.8
HI-IW-1.17		Ice wedge	-20.97	-157.9	9.8
HI-IW-1.18		Ice wedge	-20.69	-156.3	9.2
HI-IW-1.19		Ice wedge	-20.35	-154.5	8.3
HI-IW-1.20		Ice wedge	-20.78	-157.0	9.2
HI-IW-1.21		Ice wedge	-20.34	-153.9	8.8
HI-IW-1.22		Ice wedge	-20.45	-155.3	8.3
HI-IW-1.23		Ice wedge	-20.10	-151.5	9.3
HI-IW-1.24a		Ice wedge	-20.86	-157.5	9.4
HI-IW-1.24b	**Collinson Head No.1**	Ice wedge	-21.18	-160.0	9.5
HI-IW-1.25		Ice wedge	-21.23	-161.8	8.0
HI-IW-1.26		Ice wedge	-19.83	-152.6	6.0
HI-IW-1.27		Ice wedge	-21.21	-159.5	10.2
HI-IW-1.28		Ice wedge	-20.68	-155.3	10.2
HI-IW-1.29		Ice wedge	-20.40	-153.4	9.8
HI-IW-1.30		Ice wedge	-20.07	-152.9	7.6
HI-IW-1.31		Ice wedge	-20.52	-155.8	8.3
HI-IW-1.32		Ice wedge	-19.44	-146.4	9.1
HI-IW-1.33		Ice wedge	-20.22	-153.7	8.1
HI-IW-1.34		Ice wedge	-19.59	-148.5	8.2
HI-IW-1.35		Ice wedge	-19.56	-147.9	8.6
COL-1-1		Texture ice	-22.85	-173.3	9.6
COL-1-2		Texture ice	-22.74	-172.6	9.3
COL-1/4		Texture ice	-20.74	-157.0	8.9
COL-1/6	**Collinson Head No.1**	Texture ice	-19.21	-143.2	10.5
COL-1/7		Texture ice	-18.57	-139.8	8.8
COL-1/8		Texture ice	-18.22	-135.7	10.1
COL-1/9		Texture ice	-17.23	-129.5	8.4

Sample	Study site	Sample type	$\delta^{18}O$	δD	d-excess
			[‰ vs. VSMOW]	[‰ vs. VSMOW]	[‰]
HI-IW-2.1[*]		Ice wedge	-27.67	-221.1	0.2
HI-IW-2.2		Ice wedge	-29.40	-235.5	-0.3
HI-IW-2.3		Ice wedge	-30.27	-242.6	-0.4
HI-IW-2.4		Ice wedge	-29.23	-234.4	-0.6
HI-IW-2.5	**Collinson Head No.2**	Ice wedge	-28.18	-225.7	-0.3
HI-IW-2.6[*]		Ice wedge	-27.23	-216.1	1.8
HI-IW-2.7		Ice wedge	-28.42	-227.5	-0.2
HI-IW-2.8		Ice wedge	-28.45	-230.4	-2.8
HI-IW-2.9		Ice wedge	-29.55	-235.8	0.5
HI-IW-2.10		Ice wedge	-28.21	-224.3	1.4
COL-2/1		Texture ice	-27.53	-217.7	2.6
COL-2/2		Texture ice	-27.11	-214.4	2.5
COL-2/3		Texture ice	-26.78	-211.7	2.5
COL-2/4		Texture ice	-26.79	-211.1	3.3
COL-2/5		Texture ice	-26.55	-209.2	3.2
COL-2/6		Texture ice	-26.85	-212.9	1.9
COL-2/7		Texture ice	-26.67	-211.1	2.2
COL-2/8		Texture ice	-26.76	-211.7	2.3
COL-2/12	**Collinson Head No.2**	Texture ice	-27.51	-216.1	4.0
COL-2/13		Texture ice	-27.20	-213.4	4.2
COL-2/14		Texture ice	-26.97	-213.0	2.7
COL-2/20		Texture ice	-28.77	-225.1	5.1
COL-2/21		Texture ice	-28.03	-220.6	3.6
COL-2/22		Texture ice	-27.86	-219.1	3.7
COL-2/23		Texture ice	-26.92	-210.8	4.5
COL-2/24		Texture ice	-26.83	-210.5	4.2
COL-2/25		Texture ice	-26.99	-213.1	2.8
HI-SP-2-1		Snow patch	-27.41	-211.6	7.7
HI-SP-2-2		Snow patch	-28.13	-214.8	10.3
HI-SP-2-3	**Collinson Head No.2**	Snow patch	-28.43	-216.9	10.5
HI-SP-2-4		Snow patch	-27.99	-213.5	10.4
HI-SP-2-5		Snow patch	-28.38	-218.1	8.9
HI-SP-2-6		Snow patch	-26.61	-204.6	8.3

Sample	Study site	Sample type	$\delta^{18}O$	δD	d-excess
			[‰ vs. VSMOW]	[‰ vs. VSMOW]	[‰]
TSD-IW-1.1		Ice wedge	-22.61	-171.2	9.7
TSD-IW-1.2		Ice wedge	-22.48	-168.0	11.9
TSD-IW-1.3		Ice wedge	-22.02	-166.0	10.1
TSD-IW-1.4		Ice wedge	-22.49	-168.6	11.4
TSD-IW-1.8		Ice wedge	-22.06	-166.3	10.1
TSD-IW-1.11		Ice wedge	-22.41	-168.8	10.5
TSD-IW-1.12		Ice wedge	-22.46	-170.2	9.5
TSD-IW-1.13		Ice wedge	-21.86	-165.4	9.4
TSD-IW-1.14		Ice wedge	-22.76	-172.1	10.0
TSD-IW-1.15		Ice wedge	-22.51	-169.7	10.4
TSD-IW-1.16		Ice wedge	-22.71	-170.8	10.9
TSD-IW-1.17		Ice wedge	-22.50	-169.8	10.3
TSD-IW-1.18		Ice wedge	-21.73	-163.7	10.1
TSD-IW-1.19		Ice wedge	-21.88	-164.8	10.3
TSD-IW-1.20*		Ice wedge	-21.80	-164.5	9.9
TSD-IW-B1I1		Ice wedge	-24.98	-194.4	5.5
TSD-IW-B1I2		Ice wedge	-25.02	-195.3	4.9
TSD-IW-B1I3		Ice wedge	-25.25	-198.1	3.9
TSD-IW-B1I4	Thaw Slump D	Ice wedge	-24.85	-191.1	7.6
TSD-IW-B1I5		Ice wedge	-24.39	-187.8	7.3
TSD-IW-B1I6		Ice wedge	-23.94	-182.9	8.6
TSD-IW-B1I7		Ice wedge	-23.51	-178.6	9.4
TSD-IW-B1I8		Ice wedge	-22.47	-170.0	9.8
TSD-IW-B1I9		Ice wedge	-22.55	-169.8	10.6
TSD-IW-B1I10		Ice wedge	-22.56	-171.4	9.1
TSD-IW1-B2-I1		Ice wedge	-22.38	-168.6	10.4
TSD-IW1-B2-I2		Ice wedge	-22.48	-169.6	10.3
TSD-IW1-B2-I3		Ice wedge	-22.30	-168.1	10.3
TSD-IW1-B2-I4		Ice wedge	-22.25	-168.3	9.8
TSD-IW1-B2-I5		Ice wedge	-22.31	-169.1	9.4
TSD-IW1-B2-I6		Ice wedge	-22.34	-169.5	9.3
TSD-IW1-B3-I1		Ice wedge	-25.59	-200.4	4.4
TSD-IW1-B3-I2		Ice wedge	-25.40	-196.7	6.5
TSD-IW1-B3-I3		Ice wedge	-24.74	-189.8	8.1
TSD-IW1-B3-I4		Ice wedge	-24.46	-186.3	9.4
TSD-IW1-B3-I5		Ice wedge	-24.20	-184.8	8.8

Sample	Study site	Sample type	δ¹⁸O	δD	d-excess
			[‰ vs. VSMOW]	[‰ vs. VSMOW]	[‰]
TSD-TI-1/2		Texture ice	-23.02	-174.8	9.3
TSD-TI-1/3		Texture ice	-23.82	-183.4	7.2
TSD-TI-1/4		Texture ice	-24.05	-188.7	3.7
TSD-TI-1/5		Texture ice	-24.63	-200.7	-3.6
TSD-TI-1/6		Texture ice	-27.56	-215.7	4.7
TSD-TI-2-1		Texture ice	-20.11	-154.3	6.5
TSD-TI-2-2		Texture ice	-20.13	-148.6	12.4
TSD-TI-2-3		Texture ice	-19.73	-144.9	12.9
TSD-TI-2-4	**Thaw Slump D**	Texture ice	-18.97	-141.4	10.4
TSD-TI-2-5		Texture ice	-19.16	-143.1	10.1
TSD-TI-2-6		Texture ice	-19.05	-141.3	11.1
TSD-TI-2-7		Texture ice	-18.72	-139.5	10.3
TSD-TI-2-9		Texture ice	-19.00	-142.9	9.1
TSD-TI-3-1		Texture ice	-29.02	-229.0	3.2
TSD-TI-3-2		Texture ice	-27.57	-217.0	3.5
TSD-TI-3-3		Texture ice	-25.73	-198.2	7.7
TSD-TI-3-4		Texture ice	-23.72	-177.0	12.7
TSD-SPI-1-I1		Snow patch	-21.17	-159.1	10.3
TSD-SPI-1-I2		Snow patch	-21.10	-159.4	9.3
TSD-SPI-1-I3		Snow patch	-21.14	-159.0	10.1
TSD-SPI-1-I4		Snow patch	-21.00	-158.0	10.0
TSD-SPI-1-I5	**Thaw Slump D**	Snow patch	-20.85	-156.9	9.9
TSD-SPI-2-I1		Snow patch	-19.39	-142.7	12.4
TSD-SPI-2-I2		Snow patch	-18.88	-139.8	11.2
TSD-SPI-2-I3		Snow patch	-18.99	-139.8	12.1
TSD-SPI-2-I4		Snow patch	-19.26	-141.2	12.9
TSD-MI-1		Massive ice	-32.73	-254.0	7.9
TSD-MI-2		Massive ice	-33.69	-261.7	7.8
TSD-MI-3A		Massive ice	-34.01	-264.7	7.4
TSD-MI-3B		Massive ice	-34.09	-264.3	8.5
TSD-MI-4		Massive ice	-34.19	-264.3	9.3
TSD-MI-5A	**Thaw Slump D**	Massive ice	-33.43	-258.7	8.8
TSD-MI-5B		Massive ice	-33.91	-262.0	9.3
TSD-MI-7		Massive ice	-32.88	-256.2	6.8
TSD-MI-8		Massive ice	-32.77	-254.0	8.1
TSD-MI-10		Massive ice	-32.58	-254.0	6.6
TSD-MI-11		Massive ice	-32.49	-252.4	7.6
TSD-MI-12		Massive ice	-33.33	-258.6	8.0
HI-RWI-1	**Thaw Slump D**	Ice vein	-22.19	-166.7	10.9
HI-RWI-2		Ice vein	-15.51	-119.0	5.1

Sample	Study site	Sample type	δ¹⁸O	δD	d-excess
			[‰ vs. VSMOW]	[‰ vs. VSMOW]	[‰]
HI-GI-3.1-I1		Massive ice	-30.17	-236.7	4.6
HI-GI-3.1-I2		Massive ice	-30.28	-237.7	4.5
HI-GI-3.1-I3		Massive ice	-30.50	-238.8	5.3
HI-GI-3.1-I4		Massive ice	-30.75	-240.7	5.3
HI-GI-3.1-I5		Massive ice	-31.00	-242.2	5.8
HI-GI-3.2-I1		Massive ice	-29.49	-233.5	2.5
HI-GI-3.2-I2		Massive ice	-29.58	-234.0	2.6
HI-GI-3.2-I3		Massive ice	-29.66	-235.4	1.9
HI-GI-3.2-I4		Massive ice	-29.72	-235.6	2.2
HI-GI-3.2-I5		Massive ice	-29.85	-235.4	3.4
HI-GI-3.3-I1		Massive ice	-29.49	-232.5	3.4
HI-GI-3.3-I2		Massive ice	-29.44	-232.7	2.8
HI-GI-3.3-I3		Massive ice	-29.43	-232.0	3.5
HI-GI-3.3-I4		Massive ice	-29.36	-231.7	3.2
HI-GI-3.3-I5		Massive ice	-29.30	-231.1	3.3
HI-GI-3.3-I6		Massive ice	-29.13	-230.4	2.6
HI-GI-3.4-I1		Massive ice	-28.70	-227.1	2.5
HI-GI-3.4-I2		Massive ice	-28.69	-228.3	1.3
HI-GI-3.4-I3		Massive ice	-28.78	-228.0	2.3
HI-GI-3.4-I4		Massive ice	-28.77	-227.9	2.3
HI-GI-3.4-I5		Massive ice	-28.80	-227.9	2.5
HI-GI-3.4-I6		Massive ice	-28.77	-229.2	1.0
HI-GI-3.5-I1	**HI-GI**	Massive ice	-28.07	-224.6	0.0
HI-GI-3.5-I2		Massive ice	-28.15	-226.3	-1.1
HI-GI-3.5-I3		Massive ice	-28.22	-226.3	-0.6
HI-GI-3.5-I4		Massive ice	-28.29	-226.0	0.3
HI-GI-3.5-I5		Massive ice	-28.31	-227.6	-1.1
HI-GI-3.5-I6		Massive ice	-28.23	-225.5	0.3
HI-GI-3.6-I1		Massive ice	-27.28	-220.3	-2.0
HI-GI-3.6-I2		Massive ice	-27.70	-223.3	-1.6
HI-GI-3.6-I3		Massive ice	-27.77	-223.7	-1.5
HI-GI-3.6-I4		Massive ice	-27.86	-224.5	-1.6
HI-GI-3.6-I5		Massive ice	-27.98	-224.9	-1.0
HI-GI-3.7-I1		Massive ice	-21.00	-169.3	-1.3
HI-GI-3.7-I2		Massive ice	-23.24	-187.6	-1.6
HI-GI-3.7-I3		Massive ice	-24.87	-200.7	-1.8
HI-GI-3.7-I4		Massive ice	-25.94	-211.4	-3.9
HI-GI-3.7-I5		Massive ice	-26.65	-214.8	-1.6
HI-GI-3.8-I1		Massive ice	-28.28	-227.7	-1.5
HI-GI-3.8-I2		Massive ice	-28.35	-227.5	-0.7
HI-GI-3.8-I3		Massive ice	-28.29	-227.1	-0.8
HI-GI-3.8-I4		Massive ice	-28.32	-227.9	-1.4
HI-GI-3.8-I5		Massive ice	-28.30	-227.7	-1.3
HI-GI-3.9-I1		Massive ice	-36.35	-272.0	18.8
HI-GI-3.9-I2		Massive ice	-36.77	-274.9	19.3

Sample	Study site	Sample type	δ¹⁸O [‰ vs. VSMOW]	δD [‰ vs. VSMOW]	d-excess [‰]
HI-GI-3.9-I3		Massive ice	-36.85	-274.8	20.0
HI-GI-3.9-I4	**HI-GI**	Massive ice	-36.89	-275.6	19.5
HI-GI-3.9-I5		Massive ice	-36.88	-275.0	20.0
HI-SPI-1-1		Snow patch	-23.14	-180.1	5.0
HI-SPI-1-2	**Herschel Island - no specific site**	Snow patch	-23.33	-181.3	5.4
HI-SPI-1-3		Snow patch	-23.34	-180.1	6.6
HI-SPI-1-4		Snow patch	-22.61	-172.6	8.3
HI-SW-1		Surface water	-12.34	-112.4	-13.7
HI-SW-2		Surface water	-16.90	-137.4	-2.2
HI-SW-3		Surface water	-14.43	-116.8	-1.3
HI-SW-4	**Herschel Island - no specific site**	Surface water	-14.57	-116.6	-0.1
HI-SW-5		Surface water	-15.75	-127.1	-1.1
HI-SW-6		Surface water	-16.39	-135.5	-4.4
HI-SW-7		Surface water	-16.74	-133.2	0.8
HI-SW-8		Surface water	-17.51	-135.4	4.7
HI-RW-1		Rain water	-22.66	-177.5	3.8
HI-RW-2	**Herschel Island - no specific site**	Rain water	-17.83	-139.8	2.9
HI-RW-3		Rain water	-18.33	-153.0	-6.3
HI-RW-4		Rain water	-16.80	-138.5	-4.0
KOM-IW-B1-I1		Ice wedge	-22.76	-176.9	5.2
KOM-IW-B1-I2		Ice wedge	-22.85	-176.7	6.1
KOM-IW-B1-I3		Ice wedge	-21.06	-162.8	5.6
KOM-IW-B1-I4		Ice wedge	-20.49	-158.8	5.1
KOM-IW-B1-I5		Ice wedge	-22.08	-170.8	5.8
KOM-IW-B2-I1	**Komakuk Beach**	Ice wedge	-24.00	-185.4	6.6
KOM-IW-B2-I2		Ice wedge	-24.01	-184.3	7.8
KOM-IW-B2-I3		Ice wedge	-23.88	-183.5	7.5
KOM-IW-B2-I4		Ice wedge	-23.60	-182.6	6.3
KOM-IW-B2-I5		Ice wedge	-23.58	-181.5	7.2
KOM-IW-B2-I6		Ice wedge	-23.37	-179.8	7.1
KOM-1/2		Texture ice	-23.27	-180.1	6.1
KOM-1/4		Texture ice	-22.87	-178.1	4.9
KOM-1/5		Texture ice	-22.28	-172.6	5.6
KOM-1/6		Texture ice	-21.13	-162.3	6.8
KOM-1/7	**Komakuk Beach**	Texture ice	-19.62	-155.0	1.9
KOM-1/9		Texture ice	-16.67	-136.0	-2.7
KOM-1/11		Texture ice	-15.47	-129.5	-5.7
KOM-1/12		Texture ice	-14.68	-125.6	-8.1
KOM-1/13		Texture ice	-13.99	-120.1	-8.2
KOM-SP-1-1	**Komakuk Beach**	Snow patch	-27.86	-213.9	8.9
KOM-SP-1-2		Snow patch	-27.53	-214.6	5.7

* Marked samples are not considered within calculations as they represent marginal samples at the transition between ice wedges and adjacent sediments and are supposed to have been affected by isotopic exchange processes.

9 DANKSAGUNG